

Inorganic Nanocylinder Lyotropic Liquid Crystals: Rheology, Phase Behavior and Film Self-Assembly

by

Teng Xu

A dissertation submitted to the Graduate Faculty of
Auburn University
in partial fulfillment of the
requirements for the Degree of
Doctor of Philosophy

Auburn, Alabama
May 4, 2014

Keywords: Silver nanowire, silica nanorod,
liquid crystal, rheology, phase behavior, self-assembly

Copyright 2014 by Teng Xu

Approved by

Virginia A. Davis, Chair, Mary and John H. Sanders Associate Professor of Chemical
Engineering

Christopher B. Roberts, Uthlaut Professor of Chemical Engineering

Ram B. Gupta, Walt and Virginia Woltosz Professor of Chemical Engineering

Curtis Shannon, Andrew T. Hunt Professor of Chemistry

Abstract

This dissertation provided key examples of inorganic nanocylinder lyotropic liquid crystalline phase formation including silver nanowire nematic and silica nanorod smectic liquid crystals. Inorganic nanocylinder liquid crystals are a relatively new extension to the established fields of colloid and liquid crystal science. The two very different systems (silver nanowires with high aspect ratio and polydispersity, and silica nanorods with very low aspect ratio) near the Onsager theory limits for liquid crystalline phase formation are interesting to study. They can be used as model experimental systems for comparison with the theoretical calculations and computational models.

The phase behavior of the two systems was evaluated using a combination of optical microscopy, rheology, and differential scanning calorimetry. The phase behavior of the silver nanowire and nanosphere aggregate dispersions was proved as a function of the combination of solvent quality, total silver volume fraction and nanowire/nanosphere ratio. Cross-polarized optical microscopy of the silver nanowire dispersions showed a strand-like biphasic morphology and a Schlieren liquid crystalline texture which are the characteristic morphology of nematic liquid crystals. The results also showed that silver nanosphere aggregates facilitated the nematic liquid crystalline phase formation of silver nanowire due to rod-sphere demixing.

The phase diagram of silica nanorod dispersions highlights the significant effect the solvent quality has on the phase behavior. The isotropic-biphasic transition ϕ_l was significantly affected by the solvent quality. Decreasing the relative DMSO concentration from 100% to 40%

resulted in an over two order of magnitude decrease in ϕ_c . Within this range, the solvent composition had little effect on ϕ_{LC} . However, below 40/60 DMSO/H₂O crystal solvates formed and a single phase liquid crystal could not be achieved. Instead of a strand-like biphasic morphology, and Schlieren liquid crystalline textures, the dispersions exhibited characteristic smectic “onion” or “oil streak” structures that depended on the silica nanorod size and shape distribution.

The rheology characteristics of the two systems were consistent with expectations for lyotropic liquid crystals including: long oscillatory transients, the Cox-Merz rule not being obeyed, negative first normal stress difference N_1 , and a maximum in the viscosity versus concentration curve. Some rheology characteristics that are unique for smectic liquid crystal were also observed in silica nanorod smectic liquid crystal dispersion.

Several methods to assemble the dispersions into solid coatings were explored. The structures of coatings assembled by drying low aspect ratio silica nanorod biphasic dispersions in the absence of shear showed the characteristic “coffee ring” structure with rods aligned along the outer edge. While applying the same method to silver nanowires and nanosphere aggregates system, no “coffee ring” structure with alignment was observed. However, for both systems, the coating microstructure was dependent on the initial microstructure and the applied shear.

These studies on the inorganic nanocylinder liquid crystals highlight their dispersion microstructures, rich rheology and phase behavior. The processing methods studied provided a foundation for establishing the processing route on large-scale assembly of inorganic nanocylinders with controlled morphology.

Acknowledgements

I would like to thank my committee members for providing both their time and knowledge in the preparation and review of this manuscript. I am grateful to my advisor Dr. Virginia A. Davis for the insight and guidance that make this research possible and for her generous support and encouragement.

Acknowledgement and thanks are also extended to Dr. Vinod Radhakrishnan, Dr. Matthew Kayatin, Dr. Geyou Ao, Dr. Daniel Horn, Zan Haywood, Joyanta Goswami, Alex Kelly, Phillip Higginbotham, Gloria Nyankima, Suzie Murdock, Amber Hubbard, and Rebecca Lin for teaching me numerous things and making research fun.

Last but not least, I would like to thank my family and friends, especially my parents Mr. Jinzhong Xu and Ms. Caiyan Liu, my fiancé Aaron Seeto and my grandmother Ms. Zhenjun Shang for their constant support and encouragement. They make me believe life is fun and wonderful and there is no difficulty that I cannot overcome.

Table of Contents

Abstract.....	ii
Acknowledgements	iv
Table of Contents	v
List of Figures.....	viii
List of Tables.....	xiii
Chapter 1 Introduction	1
Chapter 2 Background	4
2.1 Silver Nanocylinders.....	4
2.2 Silica Nanorods.....	7
2.3 Liquid Crystal Classification	8
2.4 Smectic Liquid Crystals.....	10
2.5 Onsager Theory.....	11
2.6 Phase Behavior of Lyotropic Liquid Crystal	14
2.7 Rheological Signatures of Liquid Crystalline Polymers.....	16
2.8 Rheological Behavior of Smectic Liquid Crystals.....	24
Chapter 3 Experimental Section	30
3.1 Preparation of Silver Nanowires Dispersions	30
3.2 Preparation of Silica Nanorod Dispersions.....	32
3.3 Shape and Size Distribution Characterization of Silver/Silica Nanocylinders	34

3.4 Shearing Experiment Sample Preparation	35
3.5 Microscopy	36
3.6 Thermal Analysis	38
3.7 Spectroscopy	39
3.8 Rheology and Shear-Induced Texture Study.....	41
3.9 Electrical Properties of Silver Nanowire Coatings	44
Chapter 4 Silver Nanowire Nematic Liquid Crystal	46
4.1 Silver Nanowire Synthesis and Purification	46
4.2 Dispersion Morphology	50
4.3 Solvent Effect on Silver Nanowire Dispersions	56
4.4 Rheology	58
4.5 Shear Induced Texture	71
4.6 Coating Fabrication.....	79
4.7 Alignment Characterization	83
4.8 Electrical Properties	85
4.9 Conclusion	86
Chapter 5 Silica Nanorods Smectic Liquid Crystal	87
5.1 Shape and Size Distribution of Silica Nanorods.....	87
5.2 Silica Nanorod Characterization	91
5.3 Solvent Effect on Silica Nanorod Dispersion	95
5.4 Smectic Liquid crystalline Phase Formation and Morphology.....	99
5.5 Phase Diagram	101
5.6 Dispersion Processing Methodology Effect.....	105

5.7 Rheology	107
5.8 Shear Induced Morphology Changes.....	122
5.9 Film/Coating Fabrication	128
5.10 Conclusion	132
Chapter 6 CONCLUSION	133
REFERENCE.....	136

List of Figures

Figure 2.1 Aqueous dispersions of silver nanoparticles with 4 nm diameter and from 1 to 10 in aspect ratio Uv-Vis absorbance (left) and a variation in visible color (right).....	5
Figure 2.2 Schematic representation of Friedelian classes of liquid crystals: (a) nematic; (b) cholesteric; and (c) smectic.....	9
Figure 2.3 The focal conic domain with negative (left) and positive (right) Gaussian curvature. 10	
Figure 2.4 Schematic representation of a phase diagram	15
Figure 2.5. Viscosity versus concentration curve of PBG in m-cresol at several different shear rates	17
Figure 2.6. Three regions flow curve by Onogi and Asada.	18
Figure 2.7. Reduced shear stress versus shear unit curve of 37 wt% PBLG in m-cresol solution by walker <i>et al.</i>	21
Figure 2.8. N_1 versus shear rate of 17 wt% PBLG ($M_w = 350000$) and m-cresol for two cone angles	22
Figure 2.9 Comparison between steady shear and complex viscosities for 50 % wt. HPC in water. η (square); η^* (triangle).	24
Figure 2.10 The three basic shear geometries in a smectic A phase, showing the orientations of the smectic layers with respect to velocity field.	26
Figure 2.11 Shear stress versus shear rate curve of 8CB smectic liquid crystal with different defect density.	28
Figure 3.1. Schematic drawing of silica nanorods synthesis procedure by a wet chemistry method.	33
Figure 3.2 Schematic example for silver nanowire length distribution and wires/particle ratio counting.....	34
Figure 3.3 Schematic illustration of Rheo-SALS set-up.	43
Figure 3.4. Rheo-optical system for studying changes in dispersion microstructure under shear.	44

Figure 3.5 Silver nanowires coating on glass slide substrate for the electrical property measurement.	45
Figure 4.1 Histogram of silver nanowire (left) and nanoparticle aggregates (right) diameter distribution	48
Figure 4.2. Histogram of (a) silver nanowire length, (b) diameter distribution and (c) silver nanoparticle diameter distribution after purification process.	49
Figure 4.3 Color transmission microscopy image of silver nanowires self-assembled liquid crystalline strands.....	51
Figure 4.4 (a) Schlieren structure of silver nanowires aqueous dispersion; Polarized optical microscopy images of Schlieren textures in the nematic liquid crystalline phase silver nanowires in water.	53
Figure 4.5. Color transmission microscopy images of silver nanowire ethylene glycol dispersions at different concentration under cross-polarized light	55
Figure 4.6 Differential scanning calorimetry of silver dispersions.....	57
Figure 4.7 The response of the start up of shear for concentrated Ag-EG dispersion at 1.90 vol.% shearing at 1 s^{-1} shear rate shows a oscillatory of both viscosity and first normal force difference with time.	59
Figure 4.8 The steady shear viscosity of Ag-EG dispersions at (a) increasing region of viscosity versus concentration curve; (b) Decreasing region of viscosity versus concentration curve; (c) Entirely liquid crystalline region.	62
Figure 4.9 Relationship between viscosity and volume fraction of silver nanowires and nanospheres-ethylene glycol dispersions at a shear rate of 0.01(orange circles), 0.1(blue diamonds), 1 (green triangles), and 10 (orange circles) s^{-1}	64
Figure 4.10 Viscosity versus shear rate curve of 1.90 vol.% silver nanowires and nanoparticles in ethylene glycol shows a three Region behavior.	66
Figure 4.11 Viscosity versus shear stress curve of Ag-EG dispersions at different concentrations shows obvious yield stress at concentration higher than 0.8 vol.%.....	67
Figure 4.12 Viscosity versus shear rate curve of Ag-EG dispersion at 2.90 vol% after preshearing at 0.01 (orange squares), 0.1 (blue circles) and 1 s^{-1} (green triangles) shear rate for 2000 s.....	69
Figure 4.13. Cox-Merz rule not obeyed at silver concentration of 1.6 vol. % dispersed in EG. Constant shear viscosity (blue triangles) and complex viscosity (yellow diamonds).	70
Figure 4.14 Cross polarized light optical microscopy images of (a, b) 0.5 vol. % and (c, d) 1 vol. % Ag-EG dispersion (a, c) before and (b, d) after shearing at 2000 s^{-1} shear rate.....	72

Figure 4.15 (a)(b) SEM images of dried coating made by shearing Ag-H ₂ O dispersion with initial concentration 1.0 vol.% at 200 s ⁻¹ shear rate showing a worm-like texture with the disclination aligned in the shearing direction. (c) Optical image of same coating under cross-polarized light	74
Figure 4.16 Scanning electronmicroscopy images of dried coating made by shearing Ag-H ₂ O dispersion with initial concentration 1.1 vol% at 900 s ⁻¹ shear rate showing a monodomain aligned in the shearing direction.	75
Figure 4.17 Banded texture of silver nanowire thin film made by unidirectional shear and dried in vacuum oven and then observed under cross polarized light microscopy.	78
Figure 4.18. Scanning electron microscopy images of drop casting dried samples from Ag-H ₂ O dispersions with 0.8 vol. % Ag showing a low degree of alignment.	80
Figure 4.19. Scanning electron microscopy images of sheared and dried samples from Ag-H ₂ O dispersions showing a lower degree of alignment and demixing at lower concentrations: (a, b) initial concentration 0.16 vol% (1.7 wt%); (c, d) initial concentration 0.88 vol% (8.5 wt%).	82
Figure 4.20 Polarization dependence of Raman spectra of dried coating made from dispersion with (a) initial concentration 0.16 vol. %; (b) initial concentration 0.88 vol. % at various angles with respect to the electric field vector.	84
Figure 5.1. SEM images of silica nanorods (a) before and (b) after fractionation process by centrifugation. Histogram of lengths and diameter (insert) distribution of silica nanorods (c) before and (d) after fractionation process.	88
Figure 5.2. (a) Taper degree and (b) cone angle of silica nanorods after fractionation process at each length range.	90
Figure 5.3. (a) UV-Vis absorbance of silica nanorod dispersed in 80/20 DMSO/H ₂ O. (b) UV-Vis calibration curve of silica nanorods dispersed in 80/20 DMSO/H ₂ O at 202 nm wavelength.	92
Figure 5.4. Raman spectra at 514 nm excitation of silica nanorod dry coating with the Raman shift range of 100-3200 cm ⁻¹	94
Figure 5.5 (a) UV-vis absorbance of silica nanorod-H ₂ O biphasic dispersion during sedimentation. (b) Silica nanorod concentration change during sedimentation for silica-80/20 DMSO/H ₂ O dispersion (red triangles) and silica-H ₂ O dispersion (blue diamonds).	96
Figure 5.6 Polarized light optical microscopy images of silica nanorods dispersed in different ratio of DMSO/H ₂ O binary solvents	98
Figure 5.7 Optical images of 15.9 vol. % silica nanorods dispersed in 40% DMSO 60% H ₂ O.	100
Figure 5.8. Phase diagram of silica nanorods dispersed in DMSO/H ₂ O, where more DMSO in solvent, better solvent quality resulting in a narrower biphasic region.	102

Figure 5.9 (a) Optical images of 31.3 vol. % silica nanorods dispersed in 20% DMSO 80% H₂O. Images was taken under cross-polarized light on a Nikon Eclipse 80i with LU Plan Fluor oil 60x/1.4 objective with 2× magnification in front of the camera. (b) Enlarged highlighted area.104

Figure 5.10 (a) Length distributions of silica nanorods dispersed in 80/20 DMSO/H₂O after sedimentation and taken from top, middle and bottom layers. Cross polarized light optical images of silica nanorods dispersed in 80/20 DMSO/H₂O after sedimentation and taken from (b) middle layer with 6.0 vol. % silica nanorods and (c) bottom layer with 34.1 vol. % silica nanorods of the dispersion. SEM images of dried coating made from (d) middle layer and (e) bottom layer.....106

Figure 5.11 Relationship between viscosity and volume fraction of silica nanorods dispersed in 90/10 DMSO/H₂O109

Figure 5.12 Start-up of flow of 17.8 vol. % silica nanorods dispersed in 90/10 DMSO/H₂O at constant shear rates of 1 s⁻¹ (black curve) and 5 s⁻¹ (grey curve). (a) Viscosity versus time curve and (b) shear stress versus shear unit curve..... 111

Figure 5.13 The steady shear viscosity of SiO₂-90/10 DMSO/H₂O dispersions at (a) isotropic region; (b) Increasing region of viscosity versus concentration curve; (c) Decreasing region of viscosity versus concentration curve.115

Figure 5.14 The steady shear viscosity of SiO₂-pure DMSO dispersions at (a) Increasing region of viscosity versus concentration curve; (b) Decreasing region of viscosity versus concentration curve; (c) Entirely liquid crystalline region.116

Figure 5.15 Steady state shear rate as a function of the shear stress just above the biphasic to entirely liquid crystalline phase transition of (a) 21.3 vol. % SiO₂-90/10 DMSO/H₂O; (b) SiO₂-pure DMSO 30.8 vol. %.....117

Figure 5.16 Strain amplitude sweep test of silica nanorod-DMSO entirely liquid crystalline dispersions at different nanorod concentrations at a frequency of $\omega = 10$ rad/s.....120

Figure 5.17 Viscosity/complex viscosity versus shear rate/angular frequency curve of (a) SiO₂-90/10 DMSO/H₂O in biphasic region and (b) SiO₂-pure DMSO in entirely liquid crystalline region.121

Figure 5.18. Optical images of 29.6 vol. % silica nanorods dispersed in pure DMSO (a) without and (b) with vertical shear.....123

Figure 5.19 (a) Optical images of 29.2 vol. % silica nanorods dispersed in 90% DMSO 10% H₂O without shear. Images was taken under cross-polarized light on a Nikon Eclipse 80i with LU Plan Fluor oil 60×/0.45 objective with 2× in front of camera and (b) enlarged image. Same sample observed in shear cell using a long WD 50× objective with 2× in front of camera (c) before shearing test and (d) after shear at 37.5 s⁻¹ shear rate.125

Figure 5.20 (a) SALS of 2.1 vol. % SiO₂-90/10 DMSO/H₂O and (b) 8.5 vol. % SiO₂-90/10 DMSO/H₂O during flow curve test at 0.1, 1, 10, and 100 s⁻¹; Corresponding scattering intensity at

shear rate of 0.1 and 100 s⁻¹ and angle of 0° and 90° of (c) 2.1 vol. % SiO₂-90/10 DMSO/H₂O and (d) 8.5 vol. % SiO₂-90/10 DMSO/H₂O.....127

Figure 5.21 Images of drop casting coating obtained from silica-90/10 DMSO/H₂O biphasic dispersion at 6.7 vol. % without shear.129

Figure 5.22 Scanning electron microscope images of shear alignment film obtained from shearing silica nanorods 90/10 DMSO/H₂O dispersion (a) with 6.9 vol. % nanorods and (b) enlarged image, and (c) with 9.3 vol. % nanorods and (d) enlarged image.131

List of Tables

Table 4-1 Consistency coefficient and rate index of steady shear response of Ag-EG dispersion at different concentrations.	63
Table 5-1 Yield stress, prefactor and shear rate index of steady shear response of 21.3 vol. % SiO ₂ -90/10 DMSO/H ₂ O and SiO ₂ -pure DMSO 30.8 vol. % at different regimes.....	118

Chapter 1 Introduction

Since the discovery of carbon nanotubes by Iijima,¹ there has been great interest in the study of one-dimensional nanomaterials such as rods, wires, disc, belts and tubes. Rod or wire-like nanomaterials with high surface area and other anisotropic electric, optical, and thermal properties are attractive in enabling new applications. In this research, two nanocylinders were studied: silver nanowires and silica nanorods. Silver nanowires have excellent optical, electrical, thermal, and antimicrobial properties and a number of applications such as surface-enhanced Raman scattering (SERS), electrochemical capacitor, optoelectronic devices, and antimicrobial surfaces.^{2,3,4,5} Silica nanoparticles/nanorods have gained plenty of attention recently due to their excellent thermal, electronic, optical, optoelectronic properties and related potential applications for on drug delivery^{6,7,8}, optical resonators,^{9,10} strong glass coatings,¹¹ and imaging agents.¹²

For large scale manufacturing of nanocylinders as building blocks for applications, it is critical to set up processing route for macroscopic assembly of nanocylinders with uniform alignment. Experimental results have shown that nanocylinders films/coatings with uniform orientation have significantly improved optical^{9, 13} and electrical^{14, 15} properties, and they can be used as building blocks for functional devices. Assembly of anisotropic nanomaterials by liquid phase processing is one of the most important approaches to produce large-scale aligned nanomaterials.^{16,17,18} Processing large-scale assembly of nanomaterials from a liquid crystalline phase which already has ordered structures and relative high kinetic stability can facilitate better alignment in the final product. This approach is inspired by the existing knowledge and

commercial success of high strength synthetic polymer fibers such as DuPont's Kevlar[®] and Akzo's Twaron[®] which are both produced from liquid crystalline dispersions.

A liquid crystal (LC) is a state of matter between a liquid and a crystalline solid; LCs flow like a liquid, but have the order of a crystal. The first LC was discovered by an Austrian botanist Friedrich Reinitzer from a derivative of cholesterol in 1888. A German scientist, Zocher in 1925, observed the first inorganic liquid crystal in rod-like vanadium pentoxide (V_2O_5) colloidal aqueous suspensions. So far, more than 80,000 systems have been characterized, but as of late 1990s only 12 inorganic liquid crystals had been discovered.¹⁹ Research on nanocylinder liquid crystal has been limited by several factors including the size polydispersity of inorganic rod-like materials and a perceived lack of interesting applications compared to their organic cousins. However, the development of better inorganic nanocylinder synthesis schemes and discovery of their exciting properties have created new interest in their liquid crystalline self-assembly. Lyotropic liquid crystalline phases have recently been reported in dispersions of boehmite²⁰, goethite²¹, rutile²², CdSe²³, ZnO^{24,25} gold^{26, 27, 28} and polymer-functionalized TiO_2 nanocylinders²⁹.

In this research, we report the liquid crystal phase behavior of two systems: nematic liquid crystals of silver nanowires with high aspect ratio and a large amount of nanosphere aggregates and smectic liquid crystals of silica nanorods with low aspect ratio. For the silver nanowire system, the nanoparticles partitioned to a separate phase and enabled nanocylinder liquid crystal phase formation at lower than expected concentrations. The presence of aligned domains in the dispersion facilitated alignment in silver coatings. The morphology of the resulting silver nanowire coatings could be controlled by unidirectional shear at different shear rates. A worm-like texture of silver nanowires was observed by applying shear with $200s^{-1}$ shear rate on the silver nanowire biphasic dispersion. Further increasing the shear rate resulted in a banded texture

with silver nanowires forming a uniform alignment at the top of the coating and nanospheres being forced to the bottom of the coating.

For the silica system, a detailed investigation of the liquid crystalline microstructure and phase boundaries was performed on silica nanorods dispersed in mixtures of dimethyl sulfoxide (DMSO) and water (H₂O). Consistent with other investigations of nanocylinder liquid crystals^{30, 31, 32} changing the solvent composition (the relative [DMSO]: [H₂O]) had a significant influence on the isotropic-biphasic transition, but little influence on the biphasic-liquid crystalline transition. For solvents containing less than 40% DMSO, increasing the silica concentration initially resulted in a biphasic dispersion, but the biphasic to liquid crystal transition was not achieved by further increasing silica concentration. Above 40% DMSO, the dispersion rheology was consistent with the rod-like polymer lyotropic liquid crystals characteristics which have also been reported for lyotropic dispersions of carbon nanotubes^{30, 33, 34} and silver nanowires³⁵. However, the dispersion microstructure was markedly different from those of nematic systems. Instead of a strand-like morphology, and Schlieren textures, the dispersions exhibited “onion” or “oil streak” structures that depended on the silica nanorod size and shape distribution. Drop casting biphasic films resulted in coffee ring formation, but shearing resulted in more uniform aligned structures. These studies on the phase behavior and processing method are helpful for establish the processing route on better morphology controlled large-scale manufacturing of inorganic nanocylinder thin films/coatings.

Chapter 2 Background

2.1 Silver Nanocylinders

Nanocylinders with 1-D structure have considerable potential applications in microelectronics, optoelectronic devices, catalysts and sensors because of their interesting electrical, optical, thermal, and magnetic properties.^{16,23,36} In general, their unusual properties are due to the discrete electronic bands of nanocylinders, which is different from the continuous electronic bands of their corresponding bulk materials. Besides, the 1-D structure makes the properties of nanocylinders distinct from those of nanospheres. Furthermore, the properties of the same material with different aspect ratio are slightly different. For example, silver nanorod aqueous dispersions with different aspect ratios have different light absorption (Figure 2.1).¹⁶ There are many applications for inorganic nanocylinders based on different aspect ratios. For example, lower aspect ratio metallic nanocylinders which scatter light in the visible range can be used as tunable optical labels.³⁷ The higher aspect ratio metallic nanocylinders which absorb in near-infrared can serve as photo-therapy.³⁸ Silver nanowires with excellent optical, electrical, thermal, and antimicrobial properties have a number of applications such as surface-enhanced Raman scattering (SERS),^{2, 39,40} electrochemical capacitor,⁴¹ optoelectronic devices,^{5,42,43} and antimicrobial surfaces.

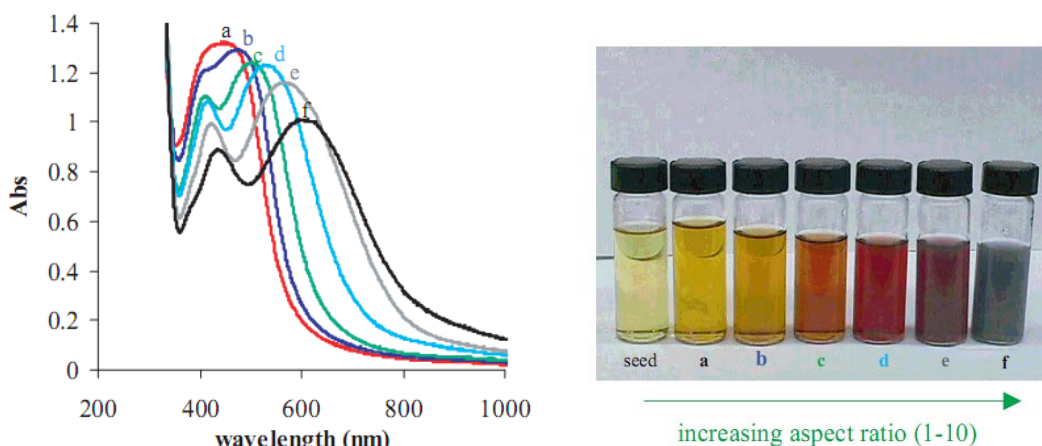


Figure 2.1 Aqueous dispersions of silver nanoparticles with 4 nm diameter and from 1 to 10 in aspect ratio. Uv-Vis absorbance (left) and a variation in visible color (right). The corresponding visible absorption spectra for (a)-(f) are also shown (left).¹⁶

The size and shape of inorganic nanocylinders can influence their properties and application. Thus, for the synthesis, the key issue is how to synthesize the certain nanocylinders with the controlled shape and size. Basically, there are two types of synthesis strategies: top-down and bottom-up approaches. The top-down approach is straight forward cutting down a large piece of material into small pieces through different means such as ball milling⁴⁴ and laser ablation.⁴⁵ Generally, for many classes of solids, it can be extremely difficult to control size, uniformity, and morphology using these methods, which limits their utility.⁴⁶ In contrast, the bottom-up approach synthesizes nanocylinders by the combination of constituent ad-atoms. Most of the synthesis techniques are based on the bottom-up approach. The bottom-up approach can be classified as vapor phase growth or solution based growth of nanocylinders.⁴⁷ Also, it can be classified as synthesis in templates, growth by phase separation, and seed-mediated growth in solution based on the differences in mechanism.

Vapor–liquid–solid (VLS) growth method, template synthesis, and wet chemical synthesis

are the three most frequently used methods for inorganic nanocylinder synthesis. Generally speaking, the vapor–liquid–solid (VLS) growth method is the growth of nanowires via a gas phase deposition reaction with the assistance of catalyst. The advantage of this method is the nanorods/nanowires obtained from this method are well oriented; the disadvantages are requirement of special catalyst and difficulty in removing the catalyst after synthesis.⁴⁸ The template synthesis method, just involves using premade nanoporous template or rod-like surfactants to synthesize nanocylinders with controlled shape and size.⁴⁵ The advantages of this method are the nanocylinders shape and size are scalable and have less contamination than in the VLS method; while the disadvantage is that it is difficult to find appropriate templates.⁴⁸ The wet chemical synthesis simply refers to chemistry done in the liquid phase. New methods continue to emerge including microwave assisted wet chemical synthesis and nanocrystal conversion chemistry. The microwave assisted wet chemical synthesis can benefit to reduce the synthesis time and save energy by using microwave heat to replace the traditional heat. This method have been successfully used in synthesizing Au and ZnS nanocylinders.^{49,50} The nanocrystal conversion chemistry method can enable synthesizing nanomaterials with compositional and morphological complexity. Overall, choosing a method to synthesize certain inorganic nanocylinders need to consider practical situation from the shape and size needed to processing, cost, time, etc.

Many kinds of synthesis methods mentioned above have been used to synthesize silver nanowires. Template synthesis of silver nanowires have been performed by using both hard templates such as mesoporous silica,⁵¹ and soft templates such as surfactant micelles,⁵² and polymers.⁵³ Wet chemical synthesis was also used in silver nanowires synthesis.⁵⁴ Considering the cost and synthesis time, microwave-assisted polyol synthesis of silver nanowires by Gou *et al*¹⁵ was used as the standard synthesis method in this research.

Microwave-assisted polyol synthesis of silver nanowires has been studied for the effects of salt concentration, microwave irradiation power and synthesis time to find the optimal synthesis condition to get a high rod/sphere ratio product. The optimal condition reported in this method is synthesis of silver nanowires by sequentially dissolving 90 mg of silver nitrate (AgNO_3), 110 mg polyvinylpyrrolidone (PVP), and 5 mg of sodium chloride (NaCl) in 20 ml ethylene glycol (EG) and heating the dispersion in microwave at 300 W for 3.5 minutes. Based on Gou et al,¹⁵ silver nanowires with uniform size (average diameter of 45 nm, average length of 4-12 μm) and high purity (> 95%) can be produced. The benefit of this method is it can synthesize silver nanowires in 3.5 minutes by using rapid and dielectric microwave heating, while other methods such as wet chemical synthesis need 1-10 hours. In addition, the microwave-assisted method does not need any external seed crystals, precursors, or mechanical stirring so that has great potential for large-scale synthesis of silver nanowires in industry.

2.2 Silica Nanorods

Silica nanoparticles have gained plenty of attention recently due to their excellent thermal, electronic, optical, optoelectronic properties and related potential applications for on drug delivery,^{6,7,8} optical resonator,^{9,10} high mechanical properties glass coating,¹¹ and imaging agents.¹² Silica nanorods can be synthesized by a wet chemistry method, which was first report by Kuijk *et al.*⁵⁵ This method can synthesize silica nanorods with high yield and relatively uniform size distribution. Based on this paper size and shape of silica nanorods are dependent on reagents, synthesize time, and ammonia concentration in water solution. The diameter of silica nanorods are controlled by the size of the emulsion system of water droplets in pentanol stabilized by sodium

citrate and PVP. And the length of silica nanorods is determined by the amount of tetra-ethyl orthosilicate (TEOS).

2.3 Liquid Crystal Classification

Besides the synthesis, another key issue for inorganic nanocylinders study is how to exploit the unique properties of inorganic nanocylinders for applications. Assembly of nanoparticles from the fluid-phase is a useful approach to synthesize large-scaled order nanomaterials. Processing large-scale assemblies of nanomaterials from liquid crystals can benefit to facilitate better alignment in the final material.

Liquid crystalline phases are phases intermediate between a crystal and liquid. They flow like liquids but have the orientation like crystals. Based on the driving force for liquid crystalline phase formation, they can be classified as thermotropic or lyotropic liquid crystals. For thermotropics, the phase transitions occur as a result of changes in temperature. Small molecules or polymers with rigid cores and semiflexible spacers usually form thermotropic liquid crystals. For lyotropics, phase transitions occur as a result of changes in concentration. Liquid crystals were first classified as nematic, smectic, and cholesteric liquid crystal by Friedel in 1922 based on morphology.⁵⁶ Nematic liquid crystals are the simplest liquid-crystalline phase, they have long-range orientational order but short-range positional order. In contrast to nematic liquid crystals, smectic liquid crystals have both long range orientational and positional order. The two most common types of smectic liquid crystals are smectic A and smectic C. In the smectic A phase, molecules are oriented along the layer normal, while in the smectic C phase they are inclined at an angle to the layer normal. The third class is cholesteric liquid crystals, also known

as twisted nematics: They are organized in layers with long-range orientation order and short-range positional order within layers, but the director axis of each layer is varied. The variation of the director axis tends to be periodic in nature. The period of this variation (the distance over which a full rotation of 360° is completed) is known as the pitch, P . The pitch can vary with temperature and it can also be affected by the boundary conditions when the chiral nematic liquid crystal is sandwiched between two substrate planes. The schematics showing in Figure 2.2 illustrate different Friedelian classes of liquid crystals.

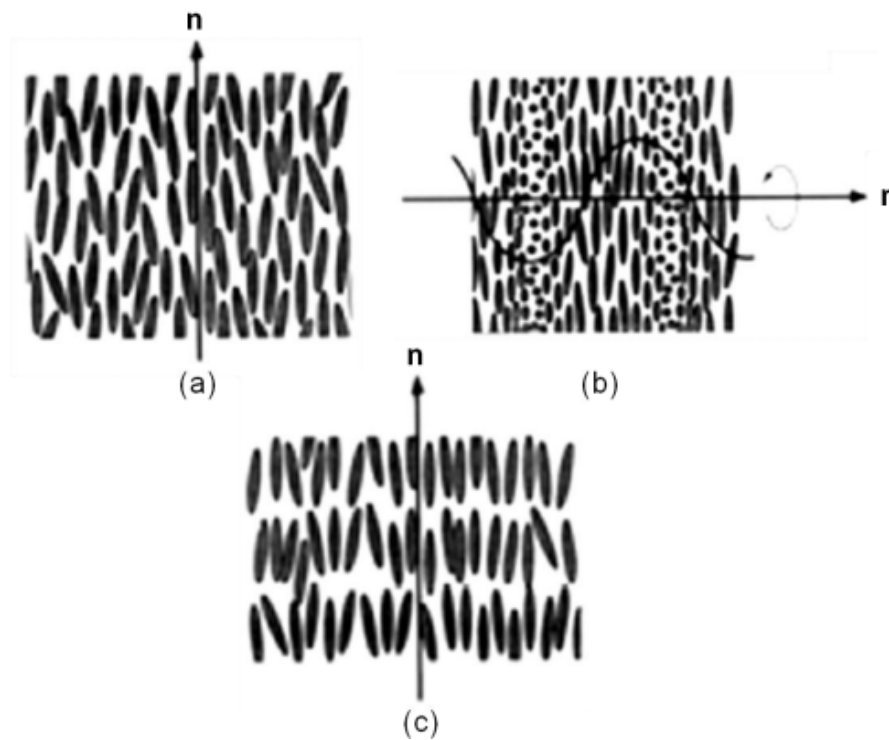


Figure 2.2 Schematic representation of Friedelian classes of liquid crystals: (a) nematic; (b) cholesteric; and (c) smectic.⁵⁷

2.4 Smectic Liquid Crystals

Smectic liquid crystals were originally described and studied by M.G Friedel⁵⁸ and more recently by Bouligand.⁵⁹ The simplest structure of smectic phase is smectic A; it is a lamellar structure made by molecules aligned in the direction perpendicular to the plane of the layers. However, in practice, smectic phases usually show certain distortions or defects. The layers of smectic phase can be bent in the shape of “Dupin cyclides”, to remain the surface orientation and equidistance of each layer.⁵⁸ This defect is called focal conic domain (FCD), defined by singularities of ellipse and hyperbola. When the singularities reduce to one point, a spherical focal conic domain with positive Gaussian curvature forms, which is also called “spherulites”/ “Onion” /multi lamellar vesicles. Focal conic domains usually occur intrinsically in bulk dispersion at the smectic-isotropic interfaces,⁶⁰ or extrinsically at the air-liquid crystalline interfaces⁶¹ due to the anisotropic surface energy.

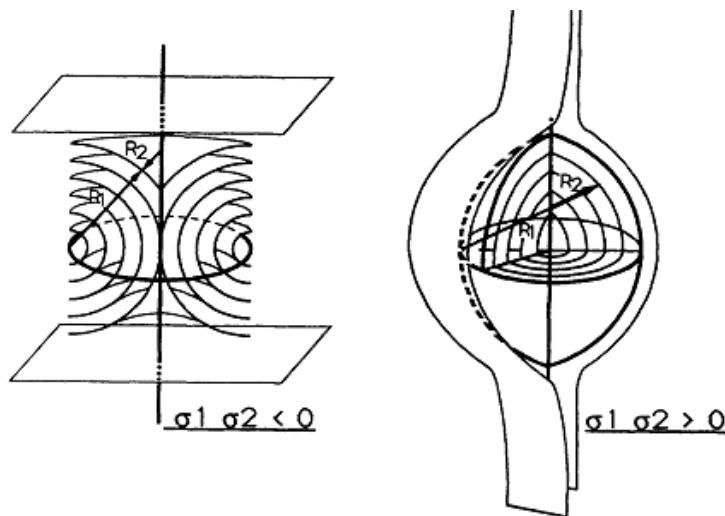


Figure 2.3 The focal conic domain with negative (left) and positive (right) Gaussian curvature.⁶²

2.5 Onsager Theory

Since the discovery of the first liquid crystal in 1888, many theories have been published to predict the phase transition of liquid crystal. Among these theories, the most classical ones are Onsager theory (1949)⁶³ and Flory lattice theory (1955).⁶⁴ Most inorganic nanocylinders studies refer to Onsager theory, while most polymer studies refer to Flory theory. Historically, the Onsager theory is important, because it was the first theory that demonstrated a nematic-isotropic phase transition due to hard rod interactions only.³⁴ This based on steric theory which is used to determine the number of ways to arrange the rods at a certain concentration in a known volume. The key idea of steric theory is that the entropy can be contributed from both transitional and orientational degrees of freedom. It assumes the rods in the system are athermal, which means the temperature does not have any significant effect on the system. It relates the number of arrangements to the entropy of the system by Boltzmann relation. Onsager theory is derived from both the steric theory and virial expansion introduced by Kamerlingh Onnes for rod-like system. It assumes a model of monodispersity system with perfectly rigid, long rods ($L/D \rightarrow \infty$). Based on Onsager theory, the isotropic to biphasic and the biphasic to liquid crystalline phase transition are determined by rod aspect ratio:

$$\phi_I = \frac{3.34}{(L/D)} \quad \phi_N = \frac{4.49}{(L/D)}$$

The order parameter of nematic phase according to this theory is $S = 0.848$. Onsager theory shows the aspect ratio (L/D) of rigid rods determines the phase transitions. It implies that for longer rods a lower volume fraction is needed to achieve a nematic phase. There is no doubt that Onsager theory is successful in predicting quantitative phase behavior of system with dilute hard rods. However, its hypothesis on very high aspect ratio, rigid rods, and monodisperse system

with the interaction only through a hard-core potential, that temperature has no effect on this transition, decide its limitations. Therefore, many adaptations have been made to the original theory.

Although, development of synthesis methods have resulted in more uniform nanostructure, still many nanomaterials are synthesized with size and shape polydispersity, which will influence the phase behavior of the hard-rod system. The problem has been considered and Onsager theory has been extended to system with same diameter but two rods length by Lekkerkerker et al in 1984.⁶⁵ The main points are the longer rods more prefer to enter the nematic phase than the shorter rods; the order parameter for the longer rods tend to be rather greater than that of the shorter rods; and the biphasic region of the phase diagram is much wider than the monodisperse system, the bigger length difference of the two rods, the wider biphasic region of phase diagram. More recently, a fully polydispersed system have been studied by Speranza and Sollich⁶⁶ in 2002. Although they used a proximate second virial term, the core finding is still consistence with Lekerkerker's study. Moreover, theories on the phase behavior of rods and sphere mixtures were also developed. In the last 60 years, great progress has been made on the study of size and shape polydispersity influence on phase behavior based on Onsager theory. Another issue on Onsager theory is that they only consider interaction between two particles in the system. It is only true for the system with rods aspect ratio at hundred or higher. For the system with lower aspect ratio, the higher order viral terms become more significant and cannot be neglected, which means multi-particles interaction should be considered. This was considered and discussed by Vroege and Lekkerkerker⁶⁷ in 1992. More recently, Khokhlov's adaptations⁶⁸ by considering attractive interactions and solvent quality extended Onsager theory and enable it to be used for a broader range of real systems. Besides, Green *et al*'s extension to account for polydispersity and

attractive interactions showed good agreement with the experimental results of the nematicogenic SWNT-superacid dispersions.⁶⁹ However, challenges remain existence on system with both size and shape polydispersity and complex interaction.

2.5.1 Onsager Theory and Inorganic Nanorods

Onsager theory has been used to successfully predict the phase transition of many inorganic nanocylinders. For example, the experimental nematic order parameter S of V_2O_5 sol derived from the distribution of scattered intensity measured by SAXS, is in very good agreement with the predictions from Onsager theory. However, Onsager theory is not enough to predict the phase behavior of all the inorganic liquid crystal systems. Complicated interaction potentials such as positive or negative surface electric charges play an important role in some inorganic systems. In this circumstance, both Onsager theory and the DLVO theory (named after B. V. Deryagin, L. Landau, E. J. W. Verwey, and J. T. G Overbeek, which describe colloidal stability as a balance between attractive van der Waals interaction and repulsive electrostatic) should be discussed together to predict the phase behavior of inorganic liquid crystal. For instance, boehmite (γ - $AlOOH$) nanorods with diameter from 1–30 nm and length from 100–300 nm grafted with polymer layers to mimic a pure hard core potential, have a good agreement between the experiment and Onsager theory predicted phase behavior.⁶⁶ For the non-grafted boehmite nanorods, at low ionic strength, electrostatic repulsion dominates, thus the phase stability can also be described by Onsager theory. However, at higher ionic strength, van der Waals attractions play a more important role than electrostatic repulsion. Thus, van der Waals attractions result in the formation of dense isotropic gels in the system, through the electronic contrast between the

mineral moieties and the solvent.

2.6 Phase Behavior of Lyotropic Liquid Crystal

Based on Doi–Edwards’ (1986) theories, there are several different phase behavior regimes of dispersed rods with increasing rod concentration: dilute, semidilute, isotropic concentrated, biphasic and entirely liquid crystalline. In the dilute regime, rods are free to rotate and translate under Brownian motion. When the rod concentration reaches to the semidilute regime, the rotation of rods is inhibited. Further increasing the rod concentration to isotropic concentrated causes both the rotation and translation of rods to be inhibited. At a critical concentration of ϕ_I , the system reaches to the biphasic regime: portions of rods start to orient and form liquid crystalline domains, while portions of rods are still isotropic. Further increasing the rod concentration causes the portion of liquid crystalline domain to increase, while the portion of isotropic domain decreases. When the rod concentration reaches to another critical concentration of ϕ_N , all rods are aligned and entirely liquid crystalline phase are formed. The phase behavior of lyotropic liquid crystals is usually related to the concentration, aspect ratio, solvent quality, and the temperature. Considering a monodisperse system with the aspect ratio of the system is fixed, the phase diagram for lyotropic rigid rod liquid crystal can be plotted with the volume fraction as the x-axis, and the solvent quality as the y-axis, which is shown in Figure 2.4. The solvent quality is similar to the Flory-Huggins interaction parameter. The phase diagram shows the solvent quality is better the biphasic region is narrower and full liquid crystalline phase can be achieved at lower concentration. If the system is size or length polydisperse, the phase diagram will be more complex. For instance, the system with length polydispersity has been reported to form

isotropic-nematic-nematic three phases coexistence.

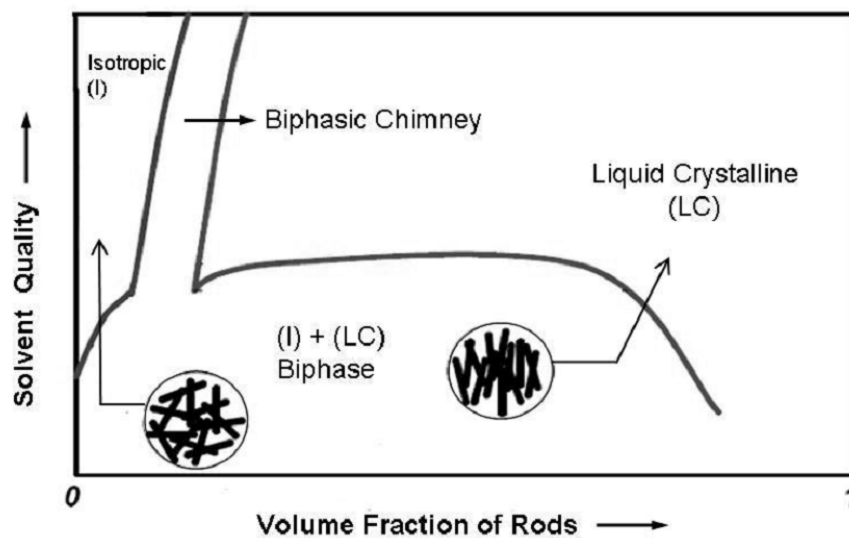


Figure 2.4 Schematic representation of a phase diagram⁷⁰

2.7 Rheological Signatures of Liquid Crystalline Polymers

Rheology is a useful tool to probe the microstructure and shear response of dispersions. Although the rheology of nematic liquid crystalline polymers (LCPs) is still not fully understood, it usually contains several characteristics: the viscosity versus concentration curve shows a maximum; start up shearing tests shows the shear stress and first normal force difference oscillate over 100 shear units before reaching steady state; the Cox-Merz rule is not obeyed; and the viscosity versus shear rate curve often shows three distinct regions.

It should be noted that it is possible that a LCP system lacks of one or more rheology features listed above, due to the complexity of the system and the shearing history of the dispersion. For example, not all the LCP show the Region I shear thinning behavior.⁷¹ Besides, due to the sensitivity of first normal stress different to the shearing history, the negative first normal stress differences behavior is not always observed.⁷¹

2.7.1 Maximum in Viscosity versus Concentration Curve

The most well known rheological property of LCP is the nonmonotonic relationship of viscosity versus concentration. For lyotropic liquid crystals, viscosity versus concentration typically goes through a maximum in biphasic regime rather than continuing to increase as in isotropic dispersions. Similar behavior is also observed in thermotropic liquid crystals that the viscosity versus temperature shows a maximum. Generally, for LCP, viscosity increases with concentration in the isotropic region, when concentration reach to biphasic region viscosity increases slower and finally reaches the maximum and then begins to decrease. This is not hard to understand, since the mesogens are aligned and can easily slide pass each other in the nematic state.

In some cases, the transition of viscosity drops suddenly at the transition from biphasic to the nematic phase with the concentration increase for lyotropic liquid crystals and temperature increase for the thermotropic liquid crystals.⁷² The transition of biphasic to single phase liquid crystalline phase is believed to be at the right shoulder of the viscosity versus concentration curve.⁷³ Once the concentration reach to the biphasic to liquid crystalline transition point, the viscosity begins to increase again with the concentration.⁷⁴

Figure 2.5 is a typical viscosity versus concentration curve reported by Kiss and Porter.⁷⁴ It shows the concentration with maximum viscosity is slightly shear rate dependent. With the shear rate increase, the viscosity maximum shifts to lower value of concentrations.

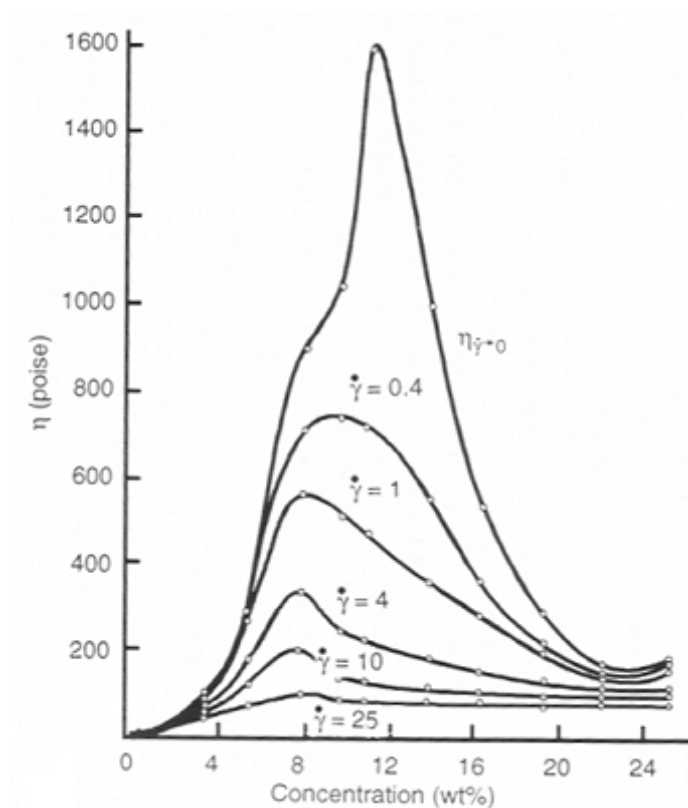


Figure 2.5. Viscosity versus concentration curve of PBG in m-cresol at several different shear rates⁷⁴

2.7.2 Three Region Behavior of Viscosity Versus Shear Rate Curve

Three region behavior of viscosity versus shear rate curve is one of the most important characteristic behaviors of LCPs. For isotropic polymer solutions, the viscosity versus shear rate usually contains two regions: a low shear Newtonian plateau region and a high shear rate shear thinning region. However, for some lyotropic liquid crystals, three regions are found in viscosity versus shear rate curve. They are a low shear rate shear thinning region (Region I), plateau region (Region II), and high shear rate shear thinning region (Region III). Thus, compared to isotropic polymer solutions, the most distinguishing feature of nematic LCP on flow curve is the Region I shear thinning behavior. The Region I low shear rate shear thinning behaviors was first reported by Onogi and Asada⁷⁵ and is usually associated with a yield stress⁷³ (see Figure 2.6).

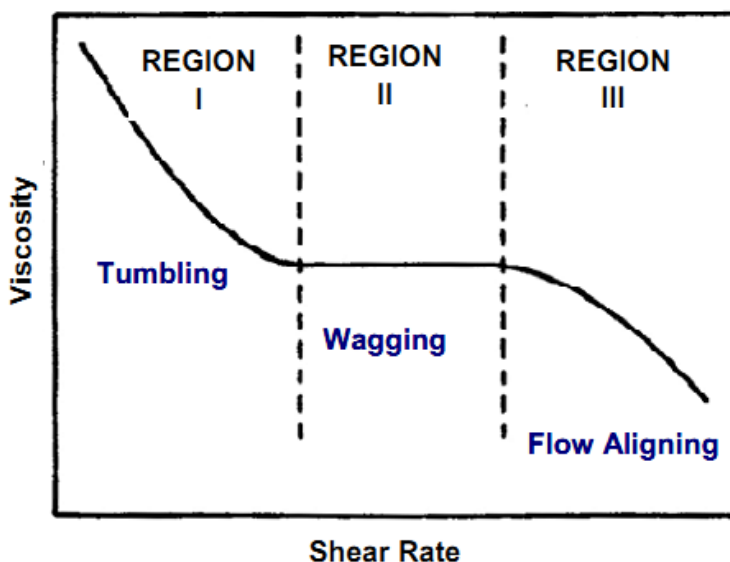


Figure 2.6. Three regions flow curve by Onogi and Asada.⁷⁵

However, Region I behavior which is related to the “tumbling” nematics, has not been observed in all the LCPs. “Tumbling” means the director of the molecule cannot find the suitable angle at certain shear rate range and prefers to rotate continuously in shearing flow.⁷⁶ This

“tumbling” behavior is usually found in nematic solution of rigid macromolecules and associated with a negative Leslie viscosity.⁷⁶ It is rarely seen in small molecule nematics. Correspondingly, the appearance of Region I behavior also depends on polymer molecule size. In lyotropic liquid crystals, polymer concentration is also an important factor effect the low shear rate Region I behavior. For example, the Region I behavior was found in PBLG solution with PBLG concentration higher than 37 wt%, while it did not appear for all the solutions with PBLG concentration lower than 37 wt%.⁷⁷ Furthermore, the existence of Region is sensitive to the shear history. For example, Walker and Wagner reported an enhancement of Region I observation in PBLG solution after preshearing the solution at its critical shear rate ($\sim 3 \text{ s}^{-1}$).⁷⁷ Besides, the Region I behavior may be difficult to observe experimentally at low shear rate due to the detection limits of shear stress.

Region I shear thinning behavior is one of the most complex and least understood feature associated with LCPs. There are typically three proposed mechanisms.⁷³

- The Region I shear thinning result from the competition between orientation of the molecules at the boundary and in the shear field. This mechanism can be explained by continuum theory and specifically the constitutive equations of Leslie and Ericksen. The yield stress is the static stress required to deform the uniform orientation director field to the one in equilibrium in the imposed flow.
- Shear thinning and the associated yield stress result from the “piled polydomain texture” of the liquid crystal.
- Both the shear thinning and yield stress result from the phase separation during flow.

The polydomain structure is believed to be preserved in both Region I and Region II. Region II is often called a “wagging” state. The viscosity plateau is related to the balance

between shear stress ($\eta\dot{\gamma}$) and the elastic stress (K/a^2) associated with the defect texture. This balance can be characterized by Ericksen number ($Er = \eta\dot{\gamma}/(K/a^2)$).⁷⁸

In Region III, the shear stress is sufficient to overcome the elastic stress and change the orientation of nematics. Typically, the slope of flow curve in Region III is lower than the slope of Region I.

2.7.3 Long Oscillatory Transients

For LCPs, different transitions are often observed when shear flow is started, the shear direction is reversed, or the shear rate is suddenly changed.⁷¹ For ordinary fluids, the start-up of flow usually results the shear stress rapidly increasing, undergoing an overshoot and then reach to steady state. However, for LCPs, the start-up of flow shows an oscillation of the shear stress and normal force with time, and the oscillation can last around and over 100 shear unit until the steady state is reached.^{79, 80, 81} Furthermore, in Region II, the viscoelastic oscillatory response times are found to be inversely proportional with the shear rate.⁷⁹ Correspondingly, the transient stress versus shear unit curves at all shear rate in Region II (time multiplied by shear rate) collapse to a single curve.^{81, 82, 83} Figure 2.7 is an example of scaling behavior of shear stress versus shear unit at the transient of start up of shear. This scaling behavior implies that the period of the oscillatory transient is inversely proportional to the shear rate. The long oscillatory transients together with the scaling behavior suggest that the polymer molecules are tumbling rather than shear-aligning in the low shear rate range.⁷¹

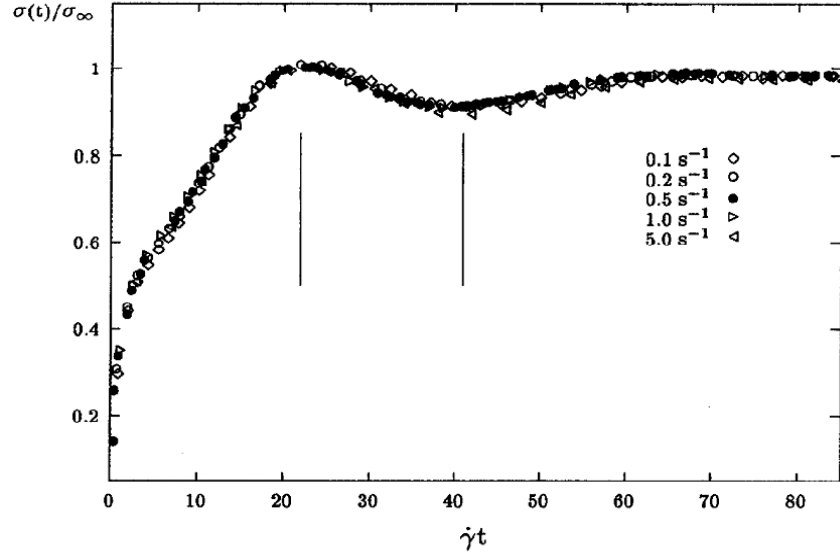


Figure 2.7. Reduced shear stress versus shear unit curve of 37 wt% PBLG in m-cresol solution by walker *et al.*⁷⁷

Analogous scaling behavior is also observed after cessation of shear. For example, Molenaers and Mewis reported a scaling behavior of linear moduli G' and G'' after cessation of shear.⁷⁹ This indicates that the elastic energy stored in shear induced texture is proportional to the shear rate. Similarly, the recoverable strain versus shear unit curves after applying different imposed shear stresses collapse to one common line for PBLG solutions.⁸⁴ This result suggests an elastic microstructure with the texture relaxation time inversely proportional to the shear rate.

2.7.4 Negative First Normal Force Differences

Another rheology signature of LCPs is that the first normal stress difference changes sign from positive to negative in Region II and back to positive with increasing shear rate. The negative N_1 feature was first reported by Kiss and Porter in 1978 for a PBLG solution.⁸⁵ The three N_1 Regions are shown in Figure 2.8. So far, the negative N_1 have all been the onset of

Region II.⁷¹ As a result, the three regions of N_1 are widely believed to be associated with the flow curve three region behavior.

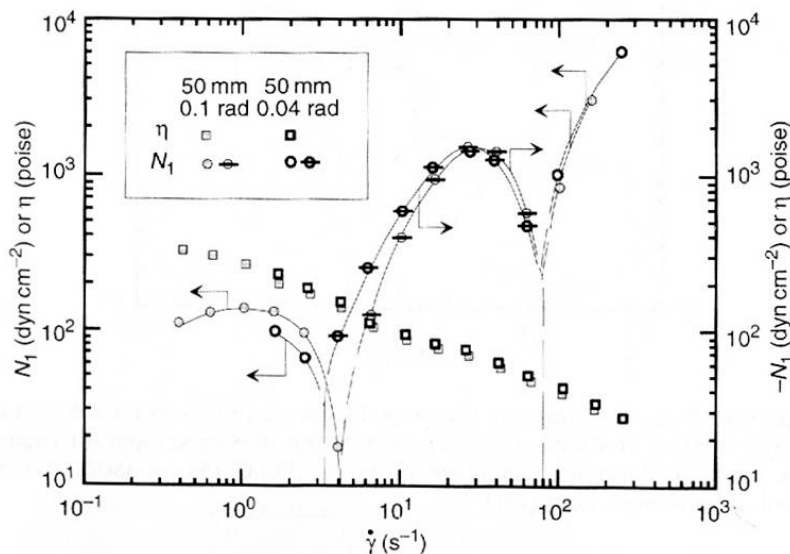


Figure 2.8. N_1 versus shear rate of 17 wt% PBLG ($M_w = 350000$) and m-cresol for two cone angles⁸⁶

The origin of negative N_1 is still controversial. Typically, there are three kinds of theories used to explain the negative N_1 feature: molecular, domain, and continuum. It is widely believed that the negative N_1 is due to the transition from “tumbling” to “wagging” by considering a polydomain fluid structure. The fine theoretical work by Marrucci firstly clearly linked the negative N_1 to a tendency of the direction of average molecule orientation about the flow direction by solving two-dimensional Doi theory.⁸⁷ Larson extended Marrucci’s work and reported the wagging Region in between “tumbling” and “flow aligning” regions, where the birefringence axis wags around a fixed direction.⁸⁸ Negative N_1 has also been related to vorticity alignment.

Similar to three region behavior, the observation of N_1 also depends on the polymer concentration and molecular weight. For some LCPs, not all three N_1 regions or only positive N_1 were found at steady state. It is possible that the experimental measurement range did not cover

the entire three N_1 Regions. It is interesting to note that the N_1 feature is not only found in nematic LCPs but also found in cholesteric PBLG.⁸⁹ Negative N_1 has also been reported in thermotropic LCPs. However, none of these reported thermotropic LCPs so far have shown all three regions.⁷¹

2.7.5 Cox-Merz Rule Not Obeyed

Dynamic rheological measurements are one of the important measurements to probe the dispersion microstructure. For example, the relative magnitude of elastic moduli G' and loss moduli G'' show whether the dispersion is more solid-like (higher G') or more liquid-like (higher G''). The dynamic viscosity versus frequency curve (which is defined as $\eta^*(\omega) = G^*(\omega)/\omega$), for ordinary fluid, is equal to the viscosity versus shear rate curve, the so-called Cox-Merz rule. However, this empirical rule is not obeyed for lyotropic liquid crystals. Figure 2.9 shows an example of Cox-Merz not being obeyed for HPC liquid crystalline dispersions by Grizzuti et al.⁹⁰ This is not surprising since in LCPs, the microstructures, and thus the rheology evolved by continuous shear and oscillatory shear are usually different. The dynamic rheological properties highly depend on the shear history and thus can probe the state of the dispersion. Oscillatory testing in the linear viscoelastic region should be performed prior to perturbing the structure with high amplitude or steady shear rate testing. However, for consistent results, low shear preshear protocols may be needed to erase unintended shear history.⁵⁷

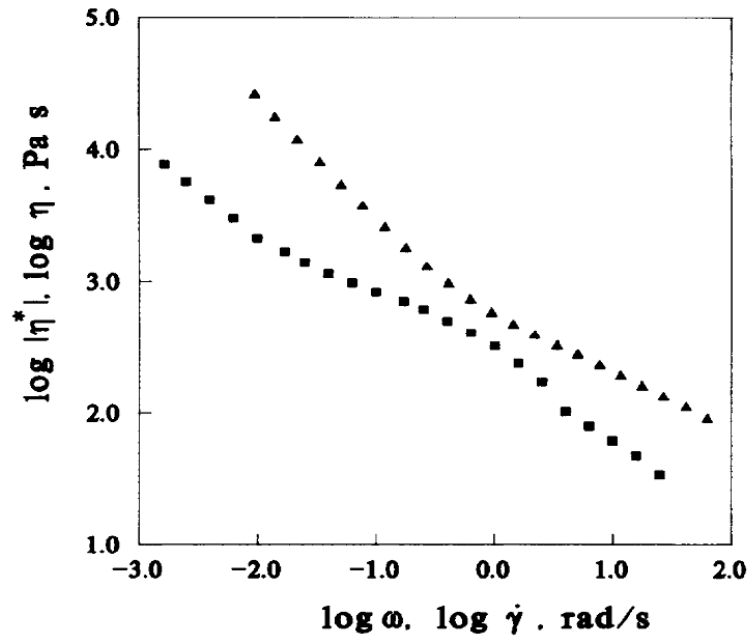


Figure 2.9 Comparison between steady shear and complex viscosities for 50 % wt. HPC in water. η (square); η^* (triangle).⁹⁰

2.8 Rheological Behavior of Smectic Liquid Crystals

Much of the attention has been focused on nematic phase rheology, but little is known on the rheological behavior of smectic phase.^{71, 91, 92, 93} Rheology of smectic liquid crystals which have both positional order and orientational order are much more complicated than rheology of nematic liquid crystals with only orientational order.

2.8.1 Hydrodynamics of Monodomain Smectic A Phase

The smectic A phase is the simplest structure of a smectic liquid crystal with lamellar phases and mesogens perpendicular to layers. The smectic phase is different from nematic phase since it has lower translation symmetry. This symmetry reduction directly results in very

different nature of defects existing in smectic phase and different rheology behavior. For a smectic A phase with a monodomain consisting of planar and equidistant layers, it is intrinsically viscoelastic. It behaves as an ordinary viscous fluid, the layers of the fluid slide one over another when the shear direction is parallel to the layers; and behaves as elastic solid when under compression and dilation.

There are typically three basic shear geometries for the monodomain smectic A phase. In the first geometry (Figure 2.10a), the normal vector of the surface is perpendicular to both the velocity and the velocity gradient. In the second geometry (Figure 2.10 b), the normal vector of the surface is perpendicular to the velocity while parallel to the velocity gradient. For these two geometries, the smectic phase is expected to behave more like a liquid than solid, characterized by a viscosity coefficient close to an ordinary fluid whose molecular size is similar. In the third geometry (Figure 2.10c), the normal vector of the surface is parallel to the velocity and perpendicular to the velocity gradient. In this case, flow is more difficult, the smectic phase behaves very different from an ordinary fluid, and it requires the permeation of mesogens between the layers. The permeation coefficient, which was firstly introduced by Helfrich⁹⁴ may be used to evaluate the flow ability in this case. On macroscopic level, shear perpendicular to the layer will cause compression due to the elastic energy between each layer. From an experimental observation perspective, considering a rheology experiment with a rheometer equipped with a polarized light optical microscopy, when the layers flat and parallel to the plates, the structure is not visibly effect by shear at any speed, since the layers can slide freely over each other (Figure 2.10b). Otherwise, the structure changes with shear rate and shear time (Figure 2.10 a and c).

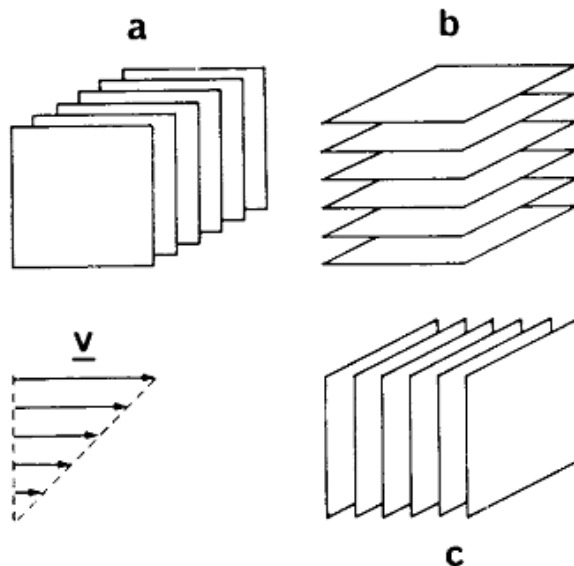


Figure 2.10 The three basic shear geometries in a smectic A phase, showing the orientations of the smectic layers with respect to velocity field.⁹⁵

2.8.2 Rheology of Smectic Phases with Defects

As discussed above, the shear response of monodomain smectic A phase should theoretically behave as an ordinary fluid when smectic layers are parallel to the shear direction, and as an elastic solid when under compression or dilation perpendicular to the layers.⁹² However, in practice, the appearance of both defects and dislocations in smectic liquid crystal systems result in very different rheological behavior from either an ordinary fluid or elastic solid. Larson *et al* found there might be similar kinetics of aligning shared by lamellar block copolymers and smectic liquid crystal at low frequencies under oscillatory shear due to their similar smectic fluctuations and defects; this was as measured by moduli during shearing.⁹¹ This similarity of lamellar block copolymers and smectic liquid crystals results from the universal dynamics controlled by smectic fluctuations and defects. However, it is important to note that there are the rheological distinctions between thermotropic and lyotropic liquid crystals. The defects encountered (i.e. “leek”

(multilayer cylinders) for thermotropic and “onion” (multilayer vesicles) for lyotropic) are different.⁹²

Many experiments have showed that the smectic systems behave like fluids with a strong internal yield stress.^{93, 95, 96} Horn and Kléman studied the rheological behavior and shear-induced texture of 8CB (a thermotropic liquid crystal which is the most commonly used smectics for rheological study) by Weissenberg rheometer using a cone-plate geometry fixture and equipped with an optical microscope.⁹⁵ The 8CB smectic liquid crystal used was treated with lecithin to promote homeotropic alignment of the sample with the layers parallel to the surfaces. However, the sample was only quasi-homeotropic due to the small angle ($< 1^\circ$) cone and plate geometry of the fixture and also unavoidable small amount of defects in the system. They observed focal conic defects induced by the dust in the system, and shear can facilitate the growth of the focal conic defects. They also showed that the 8CB smectic liquid crystalline dispersions with focal conic defects behaved like a Bingham fluid where:

$$\sigma = \sigma_s + \eta_{app}\dot{\gamma}$$

In this expression, σ_s represents a yield stress below which the sample does not flow. η_{app} represents an apparent viscosity, defined as stress divided by the shear rate. Horn *et al* estimated the defect density by measuring the light intensity I transmitted through crossed polarizers. By measuring the shear stress versus shear rate at different defect density, they found that both the yield stress σ_s and apparent viscosity η_{app} were associated with the initial defect in the dispersion. The two terms increase more or less linearly with the fraction of defects in the system as shown in Figure 2.11.

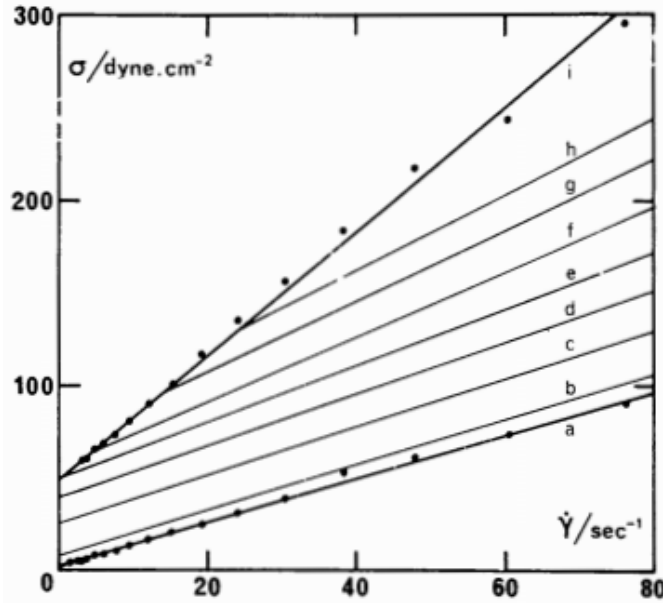


Figure 2.11 Shear stress versus shear rate curve of 8CB smectic liquid crystal with different defect density. Defect density evaluated by the light intensity I transmitted through crossed polarizers. (a) $I=0$ (quasi-homeotropic sample); (b) $I=0.5$; (c) $I=1.5$; (d) $I=2.5$; (e) $I=3.5$; (f) $I=4.5$; (g) $I=5.5$; (h) $I=6.5$ (80% of the sample containing disordered texture); (i) the maximum shear stress measured at each shear rate.

The mechanism of the appearance of yield stress is still unclear. Horn *et al* believe the yield stress possibly results from the immobilization effect of a collection of focal conic defects coming from the obedience to the rules of association between the neighboring domains,⁹⁷ which impede the flow when the stress is below certain value-yield stress. Oswald *et al* suggests that the yield stress could be explained by lubrication effect.⁹² More specifically, the focal conic domain might hinder the motion of edge dislocation due to the internal stress of elastic origin, which must be overcome so that sample may flow. However, lubrication theory is not sufficient to explain the increase of the apparent viscosity with the growth of defect. In practice, the apparent viscosity of a sample is affected by hindering of layer slipping with each other due to the edge dislocations. Besides, Horn *et al* proposed an approximation on yield stress by an energy based approach:

$$\sigma_s \sim \frac{K}{l^2}$$

Where K is the curvature elastic constant (\sim dyne) and l is the size of focal conic domain. They calculated the yield stress σ_s is at the order of $100 \text{ dyne}\cdot\text{cm}^{-2}$ ($\sim 10 \text{ Pa}$) for a sample full of defect, by assuming the domain size at the order of $1 \text{ }\mu\text{m}$ and $K \sim 10^{-6} \text{ dyne}$.

More recently, Mayer et al⁹⁸ reported a rheology study of 8CB without any surface treatment, which meant that the sample are strongly disoriented and contained high density of defect. They found the sample was shear thinning under continuous shear, following a power law: $\dot{\gamma} \sim \sigma^m$, where $\dot{\gamma}$ is the shear rate, σ is the shear stress, and the exponent $m \approx 1.7$ (close to $5/3$). They also proposed a model for this shear thinning behavior, which is derived from a theory of high temperature creep in metals and alloys and then adapted to liquid crystals. This model explained the exponent $m = 5/3$ as a result from the screw dislocations.

In general, smectic liquid crystal systems show a critical yield stress beyond which the smectic phases start flowing and the rheological response is highly affected by the texture (i.e. defects and dislocations) of the system.^{95, 98, 99} The thermotropic smectic liquid crystal – 8CB has been extensively studied, however, there have been few studied on lyotropic smectic liquid crystals composed of macromolecular mesogens.

Chapter 3 Experimental Section

3.1 Preparation of Silver Nanowires Dispersions

3.1.1 Synthesis of Silver Nanowires

The silver nanowires used in this research were synthesized using the microwave-assisted polyol method described by Gou et al.¹⁰⁰ Although this method quickly produces a large quantity of nanowires, it produces a large number of polyvinylpyrrolidone (PVP)-coated nanoparticle aggregates that are roughly spherical in shape and difficult to separate from the nanowires. In a typical experiment, a 125 ml glass bottle was used as the reactor. The reactor was first cleaned, then rinsed with acetone and deionized water. After drying, 90 mg of silver nitrate (AgNO_3) and 110 mg polyvinylpyrrolidone (PVP, MW = 58,000) were sequentially dissolved in 20 ml ethylene glycol (EG). Next, 5 mg of sodium chloride (NaCl) was added. All chemicals were purchased from Sigma-Aldrich (Milwaukee, WI) and used as received. The mixture was then sonicated for 5 – 10 minutes using a Cole Parmer bath sonicator (12 Watt, 55 KHz) in order to accelerate the dissolution of NaCl. The actual sonication time depended on when the NaCl appeared to be totally dissolved. During sonication, the appearance changed from colorless to opalescent as a result of the conversion of silver nitrate to silver chloride. The sonicated mixture was heated in a household General Electric 1.1 ft³ capacity countertop microwave (1000W, 2.45 GHz) for 3.5 min at a power level of 3 (Approximately 300W). The conversion of the silver ions to solid nanomaterials, the length of the resulting nanorods, and the fraction of nanocylinders compared to

nanoparticles could be tailored by changing the power level (frequency of magnetron oscillating on and off) and the total heating time. Research grade microwaves with constant power input were found to provide little advantage since rapid heating, even at low wattages, resulted in rapid nanoparticle seed formation and breakdown of nanowires back into particulates. It should be noted that caution should be used during and after microwave heating. The dispersions heat rapidly to the ethylene glycol boiling point of 197 °C, and care must be taken to avoid boiling over the solution or creating a significant quantity of potentially ignitable vapor in the microwave. The dispersions should also be allowed to cool before handling to avoid the potential for burns and inhaling EG vapor. After cooling, the sample should be sealed with cap to prevent the moisture absorption in EG dispersion.

3.1.2 Silver Nanowire Purification and Solvent Transfer

Several approaches for increasing the number fraction of nanowires to nanoparticle aggregates were investigated. In the majority of this research, the synthesized silver nanowire and nanoparticles dispersions were first concentrated by sedimentation for at least 48 hours, and then removing the supernatant. To remove the excess PVP and other chemicals, the concentrated Ag was first washed with acetone and then with deionized water by centrifuging at 2000 g for 20 minutes. For phase behavior studies, the sample after sedimentation and washing were transferred to EG/H₂O and then further fractionated by centrifugation using a Cole-Parmer ultracentrifuge at 5000 rpm for 5 min, and the sidewall portion or all of the sediment was gathered. For rheological characterization, the sample after sedimentation and washing process was transferred to EG/H₂O by centrifuge twice at 2000 g for 20 minutes in the EG/ H₂O to remove the

residual acetone or H₂O, and then dispersed in fresh EG/ H₂O.

3.2 Preparation of Silica Nanorod Dispersions

3.2.1 Silica Nanorod Synthesis

Silica nanorods were synthesized by the wet chemistry method reported by Kuijk et al.⁵⁵ In a typical experiment, 30 g of polyvinylpyrrolidone (PVP, MW 40,000, Sigma-Aldrich) was dissolved in 300 ml of 1-pentanol ($\geq 99\%$, Sigma -Aldrich) by sonication for 2 hours in a Branson 8510 bath sonicator at a frequency of 40 kHz and voltage of 120 V. When all the PVP had been dissolved, 30 ml of absolute ethanol (Baker), 8.4 ml of ultrapure water, 2 ml of 0.18 M sodium citrate dihydrate (99%, Sigma Aldrich) solution in water and 6.75 ml of 25 wt% aqueous ammonia (Merck) were added to the 1-pentanol (Sigma). This mixture was shaken by hand, then 3 ml of tetraethyl orthosilicate (TEOS: Si(OC₂H₅)₄, $\geq 98\%$, Fluka) was gradually added to the well mixed dispersion. After additional mixing by hand, the flask was left to rest and the reaction was allowed to proceed overnight. During that time, the conversion of TEOS to silica nanorods resulted in the dispersion changing from colorless to opalescent.

Wet Chemistry Synthesis

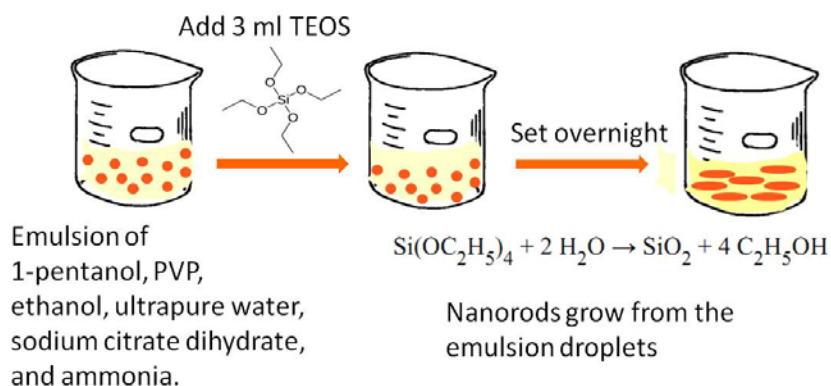


Figure 3.1. Schematic drawing of silica nanorods synthesis procedure by a wet chemistry method.⁵⁵

3.2.2 Silica Nanorod Purification and Separation

Centrifugation was used to both remove the excess reactants and fractionate the silica nanorod size distribution. The reaction mixture was centrifuged at 1500g for 1 hour. The supernatant was removed and the silica nanorods in the sediment were redispersed in ethanol. This centrifugation procedure was repeated at 1500g for 15 minutes, twice with ethanol, then twice with water and finally again with ethanol to remove residual chemicals. To remove small rods and reduce size polydispersity, the dispersions were then centrifuged three times at 700 g for 15 minutes remove the supernatant and then redispersed fresh ethanol. For the phase behavior study, silica nanorods were transferred to DMSO by centrifugation twice with DMSO at 1500g for 30 minutes, removal of the supernatant and redispersing the remainder in fresh DMSO. For silica nanorods in a DMSO/water system, the nanorods were dispersed in DMSO first, after which certain volume of water was added. In all cases, the stated DMSO/water ratio is by volume.

3.3 Shape and Size Distribution Characterization of Silver/Silica Nanocylinders

For silver nanowires and nanosphere aggregates, the shape and size distribution of the samples was characterized by both optical microscopy and scanning electron microscope (SEM). The nanowire length and rod/sphere ratio were characterized using a Nikon Eclipse 80i transmission color optical microscope equipped with cross-polarized differential interference contrast (DIC), a Retiga camera, and digital imaging workstation with Element/ImagePro software. After image capture, the magnification of the image was set in order to calibrate the length scale. The area selected to count could be adjusted using the shadow histogram bar. Parameters like rod/sphere ratio, rod length, and rod diameter were then extracted from the image. Figure 3.2 is an example of how the shadowing process works.

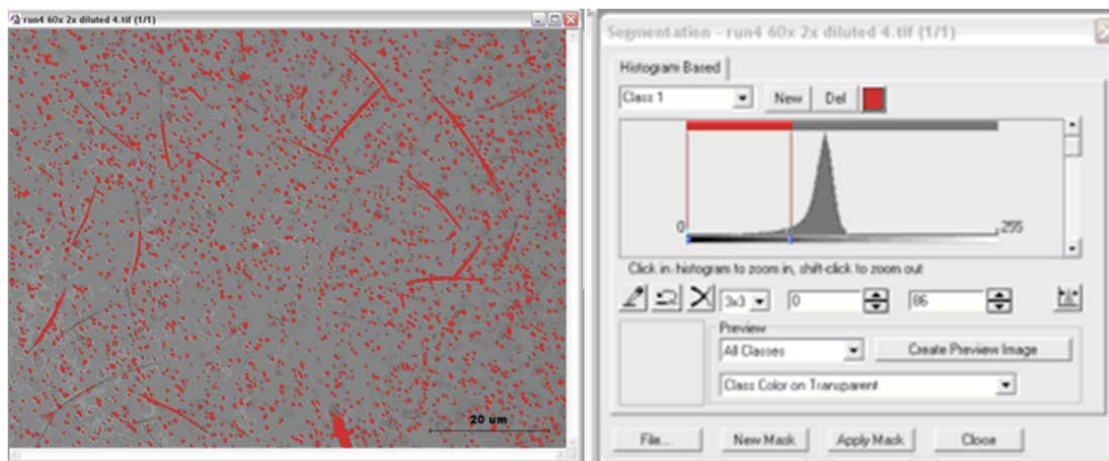


Figure 3.2 Schematic example for silver nanowire length distribution and wires/particle ratio counting. (Left) Shadowed image; (Right) Shadow histogram bar.

However, the true diameter of silver nanowires and aggregated nanoparticles cannot be measured by optical microscopy. This is due to the diffraction of light limiting the ability to resolve fine details of such small objects. The diffraction limit is determined by both the wavelength of light λ , and the refractive index of the materials used to manufacture the lens and aperture of the

microscope objective. The diffraction limit d can be calculated as follows:

$$d = \frac{\lambda}{2NA} \quad (3.1)$$

In our case, λ is approximately 550 nm, the medium for the 60 \times objective is oil with NA up to 1.5. Therefore, the lowest value of d is about 180 nm. Due to the resolution limitation of optical microscopy, the diameter distribution of silver nanowire and silver nanoparticles aggregates was characterized by using a JEOL 7000-F Field Emission SEM and ImageJ software.

3.4 Shearing Experiment Sample Preparation

Sheared samples with different concentration, shear rate, and drying methods were studied and analyzed by optical microscopy and SEM. Sample preparation methods for each microscopy type also were varied.

3.4.1 Shearing Experiment Sample Preparation on Glass Slide

For this method, a 3'' \times 1'' \times 1 mm microscope glass slide, and a 60 \times 24 mm cover slip glass obtained from Fisher Scientific were used. First, 7 μ l of the silver nanorod dispersion was dropped on the glass slide and covered with the cover glass. Then a certain amount of normal force (not measured) was applied to the cover glass by hand while simultaneously moving the glass slide laterally to quickly shear the sample. The gap between the cover slip and glass slide and the moving distance were measured by a micrometer and ruler, respectively. The shearing time was recorded by a stopwatch. The edges between the cover slip and the slide were sealed by nail polish to avoid solvent evaporation. This sheared glass slide sample was mainly used optical

microscopy characterization.

3.4.2 Shearing Experiment Sample Preparation on SEM Specimen Mounts

Two different samples were prepared on JEOL aluminum Ø12.5 x 10 mm SEM Specimen Mounts (bought from Ted Pella, Inc.). In one method, the sample was sheared directly on the bare SEM stub. Approximately 20 µl of silver nanowire dispersion (aq) was dropped directly on the SEM stub. The side of a pipette tip was then used to shear the sample for ~ 30 seconds. The sheared sample was placed into the vacuum oven to dry for at least 12 hours. The influence of different drying conditions on the silver nanowire alignment was studied. In a second preparation, the sample was sheared on a certain length of copper tape. The tape was then cut to fit on the SEM stub. This method was mainly used to gain a preliminary understanding of the influence of shear rate on the silver nanowire alignment. The dispersion was sheared on a 6.3 mm wide copper tape of 0.04 mm thickness. The gap between the stubs was maintained using a single-walled carbon nanotube-polypropylene fiber of diameter 60-300 µm. The fiber diameter was measured by optical microscopy to determine the shear gap. Samples sheared with different shear rates and then dried by vacuum oven at 100°C, -25 mmHg for at least 12 hours before characterization by SEM.

3.5 Microscopy

3.5.1 Optical Microscopy

Birefringence and various textures are the most important characterization methods of

liquid crystals by cross-polarized optical microscopy. Birefringence is the decomposition of a ray of light into two rays (the ordinary ray and the extraordinary ray) when it passes through optically anisotropic material. Thus, the anisotropic property of liquid crystals enables them to exhibit birefringence. Birefringence with dark and bright regions show up periodically by rotating the sample stage depends on the director of the liquid crystalline sample is parallel or perpendicular to the polarizer. The different defects can be observed to characterize the different kinds of liquid crystals. Thread and Schlieren textures are for characterizing nematic liquid crystals. Thread textures can be observed in the transmitted light microscope without crossed polarizers, while Schlieren textures can be observed in optical microscope with crossed polarizers. The characteristic texture of smectic liquid crystal is focal conic texture, which is also a characteristic texture for cholesteric liquid crystal. Both the fingerprint texture and focal conic texture can be used to identify cholesteric liquid crystals.

The morphology of both silver nanowire dispersions and silica nanorod dispersions were characterized by a Nikon Eclipse 80i optical microscope. Sample preparation for optical microscopy was mentioned in Section 3.3. Either transmitted light or reflected light or both were used to illuminate the sample, depending on the sample thickness and transparency. Bright or dark field, polarized or non-polarized light were varied to obtain different images. A 10 \times , 20 \times or a LU Plan Fluor oil 60 \times /1.4 objectives with up to 2 \times magnification in front of camera was frequently used for the characterization. Images were processed and analyzed by Nikon ImagePro or Element software.

3.5.2 Scanning Electron Microscopy (SEM)

The detailed morphology and alignment of dried samples were characterized by scanning electron microscope (SEM). A JEOL 7000-F Field Emission-Scanning Electron Microscope equipped with Energy Dispersive Spectroscopy (EDS) was used to characterized the morphology and alignment of both silver nanowire and silica nanorod died coatings. SEM sample preparation was also mentioned in Section 3.3. Most of the images were taken under 20 kV electron beam, with approximately a 10 mm working distance.

3.6 Thermal Analysis

3.6.1 Thermogravimetric Analysis (TGA)

Concentrations of the silver nanowire and nanoparticle mixtures were measured using a TA Instruments Q500 Thermal Gravimetric Analyzer (TGA). 8-20 μl of sample was first loaded into a cleaned and tared platinum pan. Then platinum pan was then covered with the sample chamber. Samples were heated from room temperature to 500°C with a constant temperature ramp rate of 5°C/min. The sample chamber was purged with a nitrogen balance flow of 40 cm^3/min and a sample flow rate of 60 cm^3/min . After the temperature reached to 500°C, it was held isothermal for 20 minutes until the final weight became stable.

3.6.2 Differential Scanning Calorimetry (DSC)

Differential scanning calorimetry (DSC) is a thermoanalytical technique can be used to test

heat required for glass transition, crystallization, and melting, by testing the difference in the amount of heat required to increase the temperature of a sample and reference is measured as a function of temperature. It can be used to characterize liquid crystalline phase transition from the biphasic to the entirely liquid crystalline phase by measuring the melting temperature and enthalpy changes with increasing mesogen concentration increase. The mechanism of this method is based on that the solvent associated with the ordered mesogens also shows partial ordering, and the partially ordered solvent that exhibits thermal properties which are different with the free or the bulk solvent. When the dispersion reaches a liquid crystalline phase, all the solvent present in the dispersion is associated with the mesogens and therefore no melting peak will be observed. This method is usually supplemented with X-ray scattering to show the aligned species and solvent associated with it. Here, DSC was used to study the phase transition of silver nanowires liquid crystals.

A TA Instruments Q-2000 DSC was used on silver nanowires dispersions with different concentrations to understand the extent of solvent associating with the silver nanowires. Approximately 10 μl of sample was hermetically sealed in an aluminum pan. The sample was heated or cooled three times (heating-cooling-heating) in the range of -200 to 600°C with a heating or cooling rate of $50^{\circ}\text{C}/\text{min}$. Heat flow during that temperature range was recorded, and be used to calculate the enthalpy change in melting process.

3.7 Spectroscopy

3.7.1 UV-Vis Spectroscopy

To determine the concentration of dilute dispersions, UV-Vis spectroscopy was carried out

with a Nanodrop 2000C spectrometer using both direct drop testing (2-5 μ l samples) and a 0.5 or 1 cm quartz cuvette. The UV-vis absorption was measured with a wavelength range of 200–900 nm. Pure DMSO, pure H₂O, and mixture of DMSO and H₂O were measured as the references.

3.7.2 Raman Spectroscopy

To characterize the chemical residues on the silica and silver coating, and to also qualitatively measure the silver nanowire alignment, a Renishaw inVia Raman Spectrometer attached to a Leica optical microscope was used. Both silver and silica samples were irradiated using a 514 nm Spectra-Physics air-cooled ion excitation laser with a 50 \times objective. For a typical silver nanowire coating alignment measurement, the orientation was determined by comparing the ratio of signature peak intensities of the sample aligned parallel and perpendicular to the laser. Dried sample spectra were collected at 0°, 45°, and 90° angles to the incident polarization by carefully rotating the sample stage. Data were collected by accumulating 5 scans of Raman shift from 600–1800 cm^{-1} with 10% laser power and 10 seconds exposure time. For a typical surface chemical measurement of silica nanorod coatings, the samples were also irradiated using a 514 nm Spectra-Physics air-cooled ion excitation laser with a 50 \times objective. Dried sample spectra either directly on the glass slide or the SEM specimen mount fixed on the glass slide, were collected by accumulating 10 scans of Raman shift from 100-3200 cm^{-1} with 50% laser power and 10 seconds exposure time. It is noted that the laser power and times of scan accumulation may varied to ensure the counts of Raman signal in a reasonable range (Peak saturated at 250,000 counts).

3.8 Rheology and Shear-Induced Texture Study

3.8.1 Rheology

Rheology was characterized at 20 °C using an Anton Paar MCR 301 rotational rheometer equipped with a P-PTD200 peltier temperature control device and H-PTD 200 peltier upper oven. Generally, for high concentration silver nanowire dispersions with silver nanowire volume fractions above 1.7 vol.%, a parallel plate fixture with 25 mm diameter was used. To increase the accessible shear rate range for low concentration dispersions, a parallel plate fixture with 50 mm diameter was used. Due to the large diameter of silver nanoparticle aggregates and large length of silver nanowires, the cone and plate fixture which has a markedly smaller measurement gap (0.048mm for CP25 and 0.052mm for CP50) was not used for the rheology test.

For silica nanorod dispersions, rheology tests were performed at 20 °C for all dispersions. To increase the accessible shear rate range, a 50 mm cone and plate fixture with angle of 2.018° and gap of 0.052 mm was used for low concentration dispersions; While a 25 mm cone and plate fixture with angle of 1.979° and gap of 0.048 mm was used for high concentration dispersions. For silica nanorods dispersed in pure DMSO or 90/10 DMSO/H₂O, rheology measurements were performed on two sample loads and two runs for each load.

The temperature of the samples was controlled at 20 °C for all the rheology tests to reduce the solvent evaporation. For Ag-EG and SiO₂-DMSO dispersion, silicon oil is used to seal the upper hood and prevent the moisture absorption by EG or DMSO.

3.8.2 Rheo-SALS

Small-angle scattering (SAS) is a well-established technique for structure analysis and interactions of systems with the size on the order of 10 to 1000 Å. It includes light scattering, small angle X-ray and neutron scattering. For small angle light scattering, the elastic scattering predominates, and the resulting scattering pattern provides the information about size, shape and sample microstructure. There are two main scattering processes, depending on the diameter of the particles in the medium. Rayleigh light scattering scatters photons on particles, which are small compared with the wavelength of the laser beam. Mie light scattering scatters the light on particles, which are larger than the wavelength of the laser beam. Here, a Rheo-SALS system was used to analyze the dynamic structure of dispersion under shear. The combination of rheology and SALS (Rheo-SALS) allows the investigation of shear-dependent structural changes or crystallization spontaneously with the rheological measurement. Rheo-SALS tests were performed by using an Anton Paar MCR 301 rotational rheometer equipped with SALS with a 658 nm laser. The SALS setup is illustrated in Figure 3.3. The 632 nm laser beam first went through the quartz glass and then interacted with the nanoparticle dispersion. The laser beam impinged on a screen, where the elastically scattered light was recorded with a CCD (charge coupled device) camera. This measurement was carried out by using parallel plate geometry constructed out of transparent quartz glass. The plate radius used in all experiments was 43 mm transparent quartz glass. The gap was set between 0.3 and 1.0 mm for all measurements. The SALS system is not equipped with any temperature controlling device except that of the cooling water circulation. However, the water temperature at the device inlet was monitored via the Rheo-SALS system.

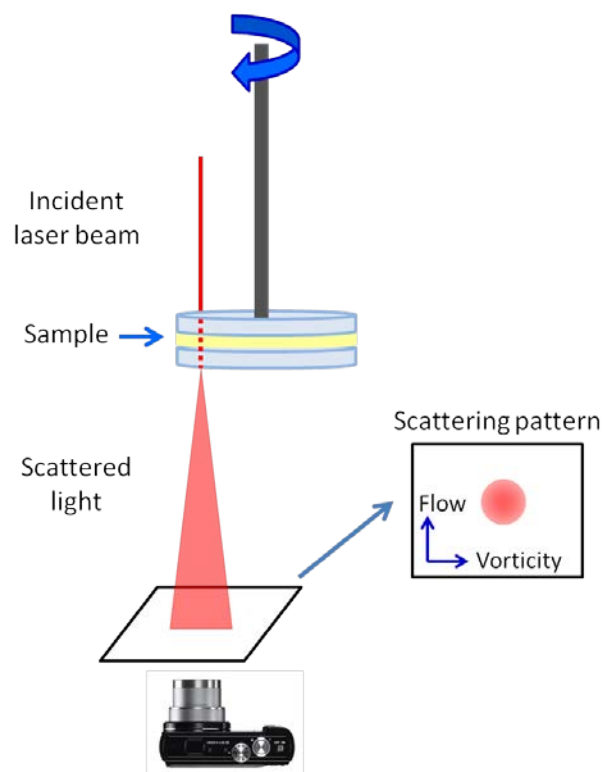


Figure 3.3 Schematic illustration of Rheo-SALS set-up.

3.8.3 Rheo-Optical Study

Shear induced textures of nanoparticle dispersion were also studied by optical microscopy equipped with Linkam optical shearing system (CSS450) and recorded by a CCD camera. The system allows structural dynamics of complex fluids to be directly observed, while they are under precisely controlled temperature and shear. By using the optical shearing cell, it is possible to study the microstructure evolution of complex fluids in great detail for many physical processes, including coarsening of binary fluids during their phase separation, flow-induced mixing and demixing of polymer blends, defects dynamics of liquid crystals, and aggregation of red blood cells and their deformation under flow. This method is useful for correlating microstructural dynamics with rheological data. Figure 3.4 shows the general Rheo-optical setup for dynamic dispersion microstructure study. The typical gaps used for the shear cell were 30–100 μm ,

depending on dispersion concentration and the average size of the nanoparticle. The exact gap depended on the sample. To avoid confinement effects, the gap should be at least 10 times larger than the longest particle dimension.

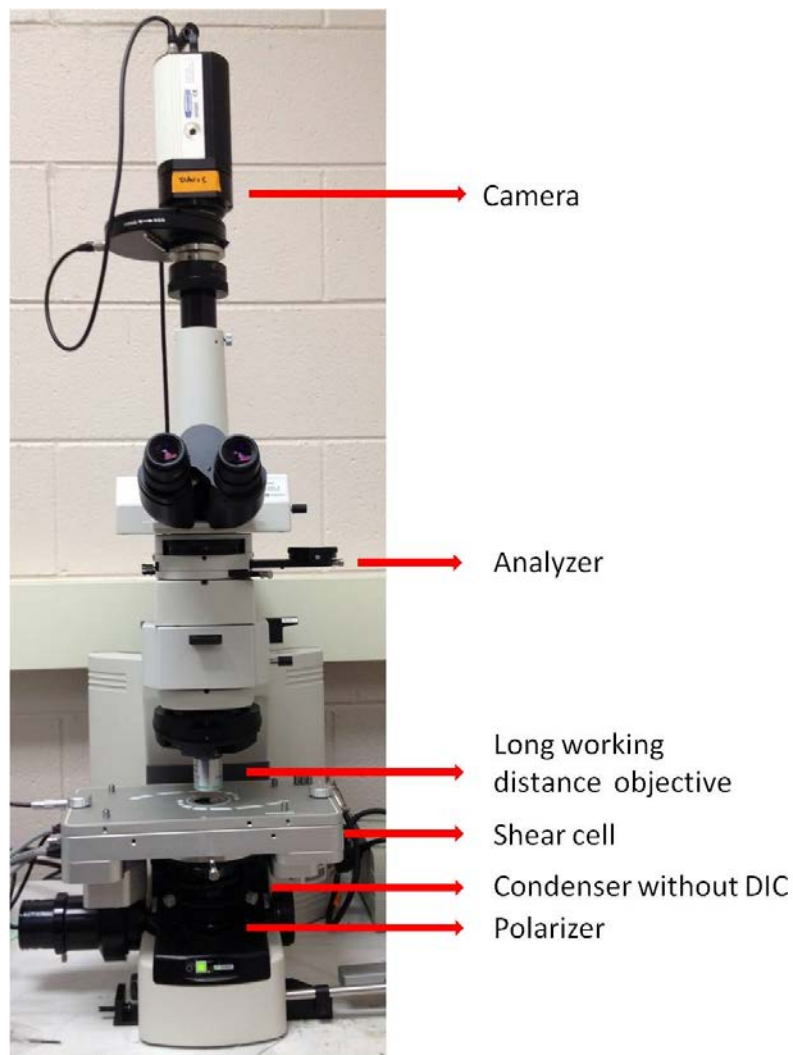


Figure 3.4. Rheo-optical system for studying changes in dispersion microstructure under shear.

3.9 Electrical Properties of Silver Nanowire Coatings

The electrical properties of the silver coatings were characterized by a Keithley 4200-SCS

semiconductor characterization system with four-point probe method. Silver nanowires were coated on an insulated substrate-glass slide and use silver painting to enhance the connection of the probes to the silver coatings. Figure 3.5 shows a typical silver coating for electrical property measurement. The thickness of the coating was $\sim 2 \mu\text{m}$. The sheet resistance of the coating was calculated by

$$R_{sheet} = \frac{V}{I} \times CF$$

Where V is the measure DC voltage across the two voltage probes and I is DC current passing through the current probes. CF is the geometric correction factor, which is usually required for sheet resistance calculation by four-point probe method, with $CF = \frac{t/s}{\ln(2)}$, t is the thickness of the thin film and s is the probe spacing.

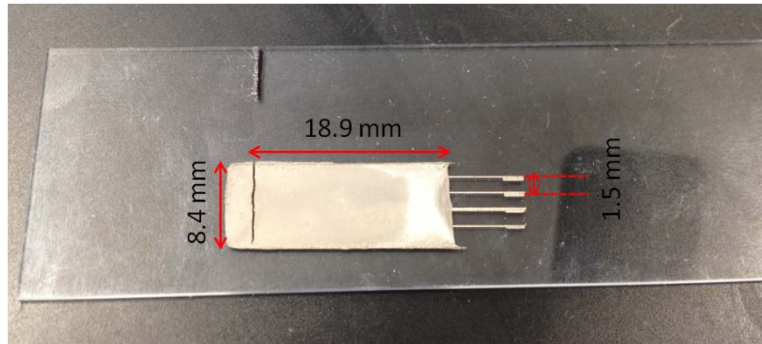


Figure 3.5 Silver nanowires coating on glass slide substrate for the electrical property measurement.

Chapter 4 Silver Nanowire Nematic Liquid Crystal

4.1 Silver Nanowire Synthesis and Purification

The merit of the microwave-assisted polyol method is that it can produce a significant number of nanowires in a short amount of time due to the rapid dielectric heating by microwave irradiation. The synthesis time was 3.5 minutes rather than the several hours required for traditional heating. A setting of power level 3 and 3.5 min of total time was found to produce the highest number fraction of nanowires compared to nanoparticle aggregates. At these conditions, the dispersions could be qualitatively characterized by their light brown color and slightly shiny appearance. However, the number fraction yield of nanowires was typically less than 0.10. Consistent with the findings of Gou *et al*, both higher power levels and longer times resulted in both shorter and a lower percentage of nanowires due to the competition amongst seed formation, nanowire growth, and dissolution reactions. This competition likely also contributed to the nanowire size polydispersity.

Synthesized silver nanowires after sedimentation were characterized by both optical microscopy and SEM. This revealed a broad distribution of both length and diameter with an average length L of 5.9 μm and average diameter D of 56 nm. This results in an average aspect ratio of $L/D \sim 100$. SEM images showed that what appeared to be nanoparticles using optical microscopy were actually large aggregates of spherical and cubic nanoparticles overcoated with a layer of PVP.

Silver nanowires for phase behavior studies after further fractionation were also

characterized. These results showed the nanowire length typically decreased after multiple centrifugation processes. The average length of silver nanowire in EG at sidewall, whole bottom, and in H₂O whole bottom were: 4.8, 3.5, and 5.3 μm . A representative histogram of the nanowire and nanoparticle aggregates diameter distribution is shown in Figure 4.1. The total diameter of the nanoparticle aggregates varied widely but was typically several times larger than that of the nanowires.

Silver nanowires for rheological study were also characterized by both optical microscopy and SEM. Size measurements made on more than 5000 total count by optical microscopy showed the similar broad length polydispersity of silver nanowire with average length $\langle L \rangle = 4.8 \mu\text{m}$ shown in Figure 4.2 (a) and low number ratio of silver nanowire: silver nanoparticle aggregate ~ 0.05 . The diameter distribution of both silver nanowire and silver nanoparticle aggregate was characterized by SEM shown a broad diameter distribution of silver nanoparticle aggregate with average diameter $\langle D \rangle = 170 \text{ nm}$ (Figure 4.2 (c)) and relatively narrow diameter distribution of silver nanowire with average diameter $\langle D \rangle = 60 \text{ nm}$ (Figure 4.2 (b)). These results equate to an average nanowire aspect ratio $L/D = 80$.

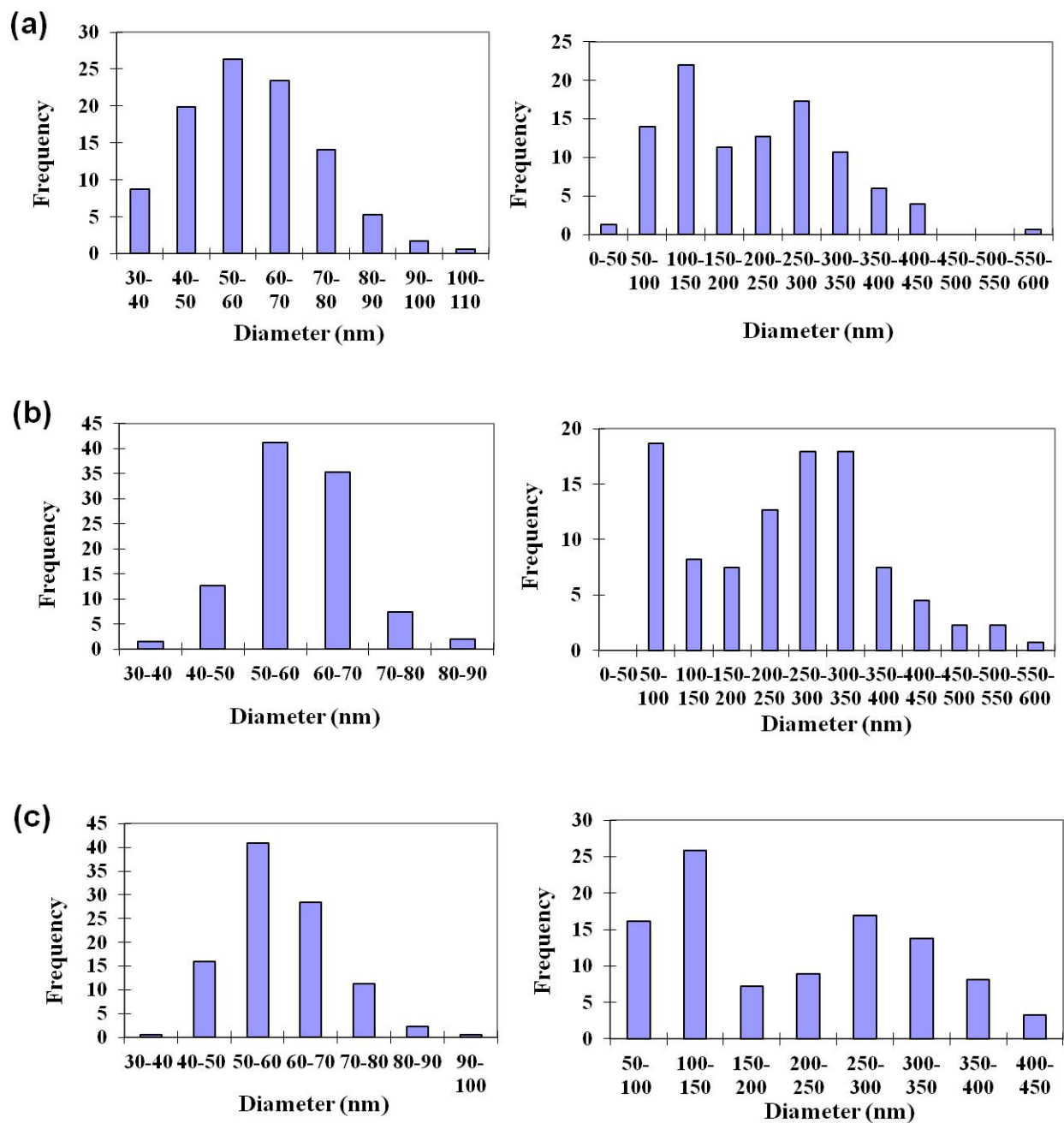


Figure 4.1 Histogram of silver nanowire (left) and nanoparticle aggregates (right) diameter distribution (a) Ag-EG sidewall portion, (b) Ag-EG whole bottom portion, (c) Ag-H₂O whole bottom portion.

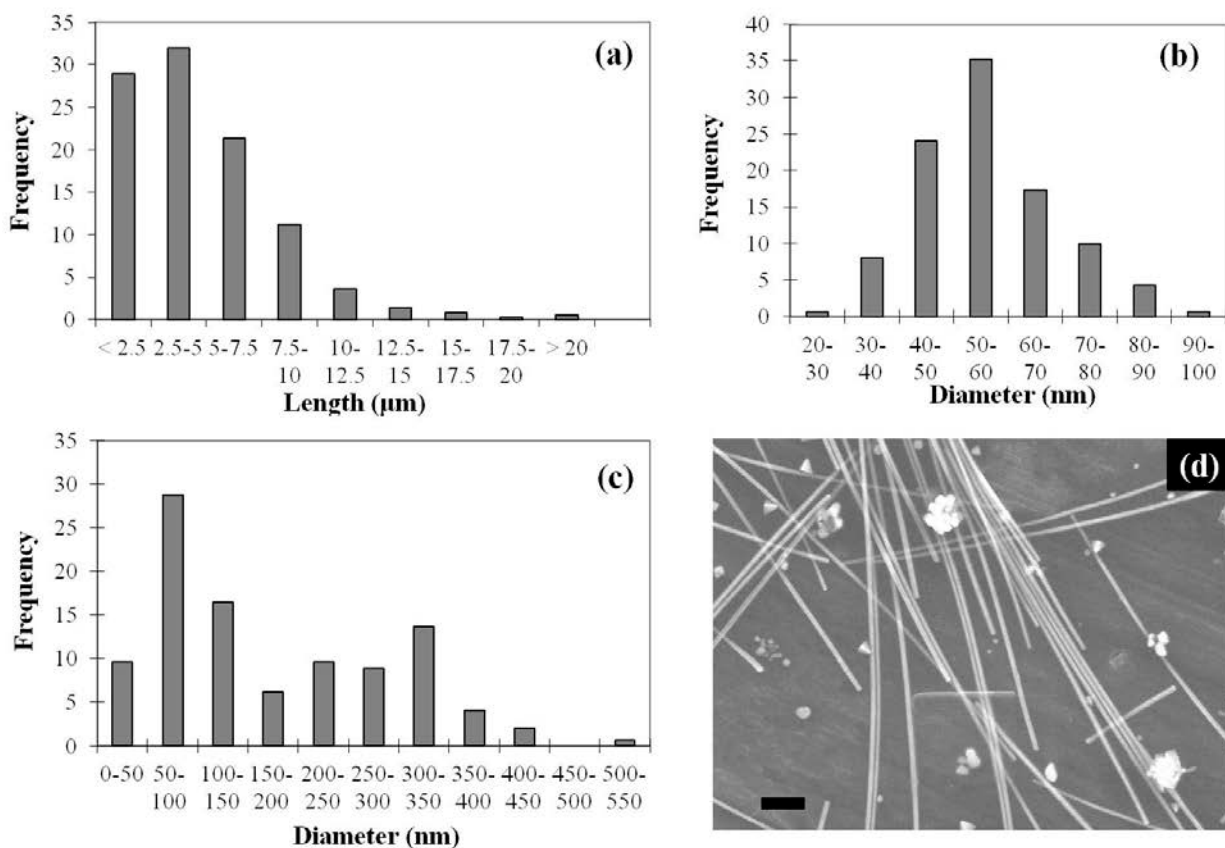


Figure 4.2. Histogram of (a) silver nanowire length, (b) diameter distribution and (c) silver nanoparticle diameter distribution after purification process. (d) SEM image of silver nanowires and nanoparticle system. The scale bar in the SEM image is 500 nm.

4.2 Dispersion Morphology

4.2.1 “Spaghetti” Structure

Cross-polarized microscopy of the Ag-EG dispersions in the biphasic region showed a “spaghetti” morphology, which was first reported for biphasic dispersions of 500 nm long SWNTs in 102-120% H₂SO₄.³⁰ In our previous research, this morphology was also observed and reported in Ag-EG biphasic dispersion without any washing procedure by Murali et al.³⁵ Here, optical microscopy showed agreement with our previous observation that in biphasic region the nanowires self-assemble into birefringent strands where silver nanowires are free to translate along the length of the strand, while the nanoparticle aggregates primarily partitioned toward the bottom surface of the sample. Figure 4.3 shows a representative image of a single focal plane under crossed polarizers. The mechanism of this unusual morphology formation is still not completely understood. It was suggested by Murali *et al* that there is an underlying physics dictating the formation of the unusual strand-like liquid crystalline domains in both SWNTs and Ag nanocylinders.³⁵ We proposed that the large persistence lengths and attractive interactions in both SWNTs and Ag nanocylinders might contribute the key difference of SWNTs and Ag nanocylinders to the “rodlike” polymers which form well-characterized globular domains.

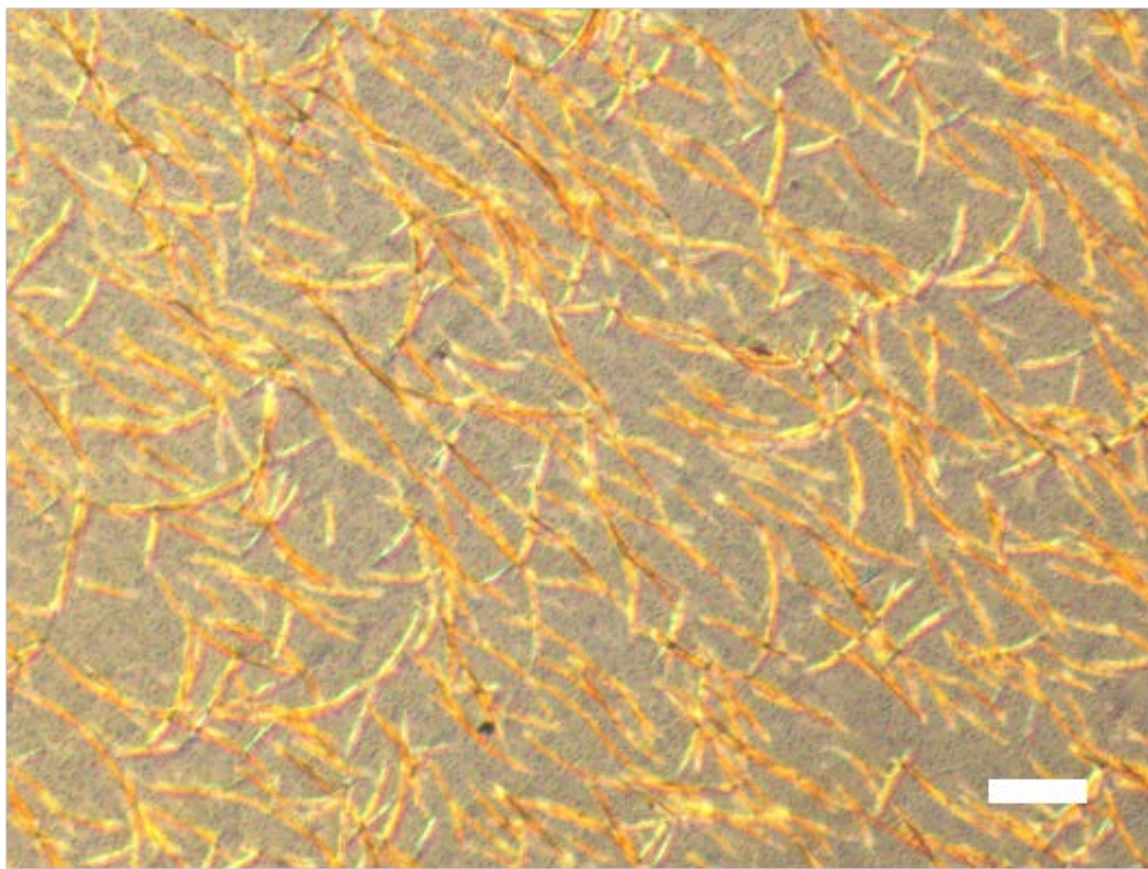


Figure 4.3 Color transmission microscopy image of silver nanowires self-assembled liquid crystalline strands observed by cross-polarized light using a 20x DIC 0.45 NA objective and 2x additional magnification in front of the camera. The scale bar is 20 μm .

4.2.2 Schlieren Texture

The detailed structure of silver nanowire dispersions near the biphasic to liquid crystalline transition was characterized. Figure 4.4 shows a representative polarized optical microscopy images of silver nanowire-H₂O biphasic dispersions. The strong birefringence with black brush patterns in Figure 4.4 (a) shows typical Schlieren textures of a polydomain nematic phase. The polydomain structure shown in Figure 4.4 is believed to be the result of “spaghetti” strand coalescence. Figure 4.4. (b, c) also shows the polydomain regions changed alternately from dark to bright base on the relative alignment of the nematic director and the polarization vector of the light. On large length scales, the domains are globally randomly oriented with respect to each other. These structures provide further evidence of liquid crystallinity and have also been observed in other nanocylinder liquid crystals such as goethite nanorods in water,²¹ ZnO in DMS,^{24,25} oxidized MWNT in water,¹⁰¹ and SWNTs in 102% H₂SO₄.³⁰

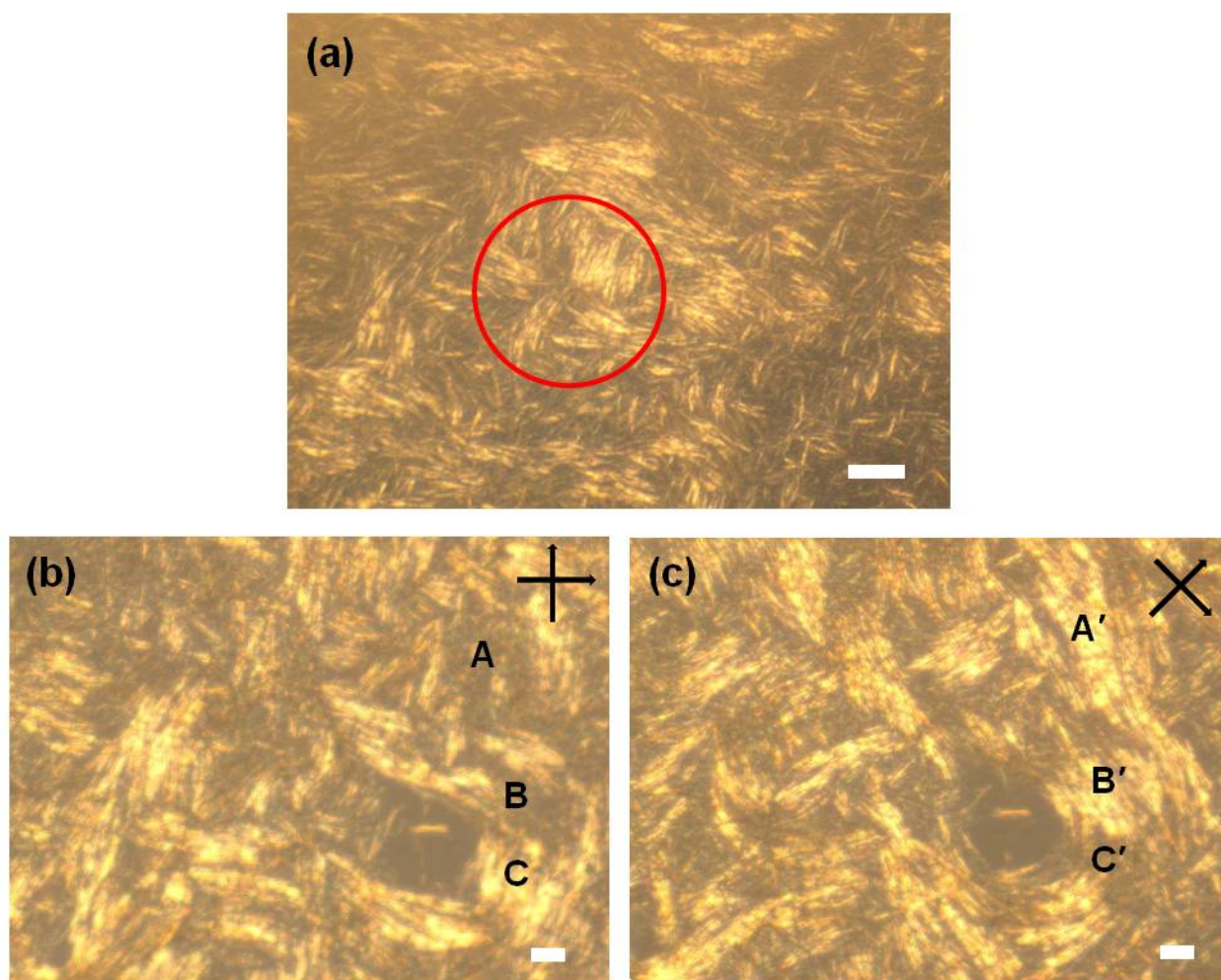


Figure 4.4 (a) Schlieren structure of silver nanowires aqueous dispersion; Polarized optical microscopy images of Schlieren textures in the nematic liquid crystalline phase silver nanowires in water. The polydomains become bright and dark as the crossed polarizers rotate. Regions A', B', and C' of the (c) image correspond A, B, and C of the (b) image after 45° rotation of crossed polarizers. The scale bars are 20 μm in all images.

4.2.3 Nanowire Concentration Effect on Morphology

The dispersion microstructure of silver nanowire and nanoparticle aggregates at different concentrations was studied by polarized optical microscopy. The silver nanowires and nanoparticle aggregate isotropic-biphasic transition ϕ_I , where the characteristic “spaghetti” strands begin to form was 0.1 vol.% in EG. As shown in Figure 4.5, as the silver nanowire concentration increased, the fraction of birefringent liquid crystalline domain size increased. It is interesting to note that there is a dramatic microstructure change at silver nanowire volume fractions between 0.6 and 0.8 vol.%. It seems like that a more networked structure forms in Ag-EG with 0.8 vol.% silver nanowires. When the silver volume fraction reached to approximately 2.8 vol.%, a single phase polydomain lyotropic liquid crystal formed in ethylene glycol. This entirely liquid crystalline phase is a demixed nematic state, which contains both strong birefringence rod-rich region and spheres-rich (dark brown) region. The rod-sphere demixing phase was also reported in our previous research³⁵ and the modeling system of polymer spheres and rod-shape filamentous bacteriophage *fd* virus¹⁰².

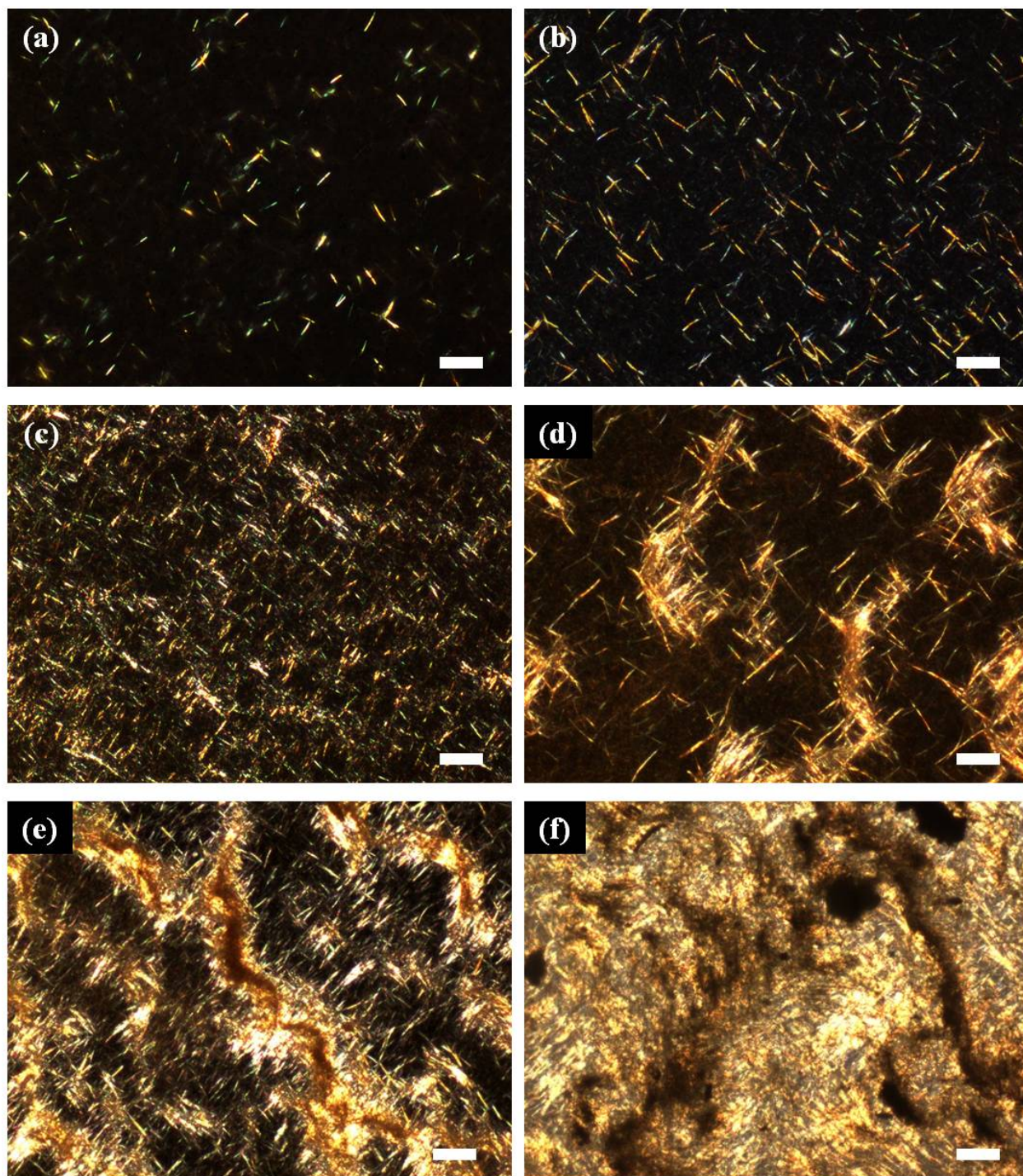


Figure 4.5. Color transmission microscopy images of silver nanowire ethylene glycol dispersions at different concentration under cross-polarized light using a 20x DIC 0.45NA objective. The silver nanowires and nanoparticle aggregates concentration are (a) 0.1 vol. %, (b) 0.6 vol. % (c) 0.8 vol. % (d) 1.6 vol. % (e) 2.2 vol. %, (f) 2.8 vol. %. Scale bars are 20 μm .

4.3 Solvent Effect on Silver Nanowire Dispersions

Differential scanning calorimetry (DSC) was used to determine the phase transition from the biphasic region to the entirely liquid crystalline phase by studying the interaction between the mesogen and solvent.¹⁰³ Silver nanowire and nanosphere mixtures in both aqueous and EG dispersions obtained from the bottom of centrifuge tubes were explored at different concentrations. These data were also compared with the data for silver nanowire and nanosphere EG dispersions obtained from the side-wall portion of the centrifuge tube. As shown in Figure 4.6a, pure ethylene glycol shows a melting peak with the enthalpy change of 188 J/g at -15 °C. As the concentration of silver nanowires and nanospheres mixture increased, the enthalpy started decreasing dramatically until volume fraction reached 0.02 vol.% and then slowly decreased showing a plateau until volume fraction reached 0.14 vol.%. After that, it decreases dramatically again and finally goes to zero at volume fraction equal to 0.42 vol.%. This suggests the transition from biphasic to liquid crystal phase occurs at the volume fraction (ϕ_N) around 0.42 vol.% for the Ag-EG dispersion obtained from the side wall of the centrifuge tube. DSC data of a Ag-EG dispersion sample, from the bottom of centrifuge tube, showed a similar trend of dramatic decreased, slow decreased and another dramatic decreased. The only difference is that the transition volume fraction from biphasic to liquid crystal phase was 1.29 vol.%, instead of 0.42 vol.%. For the Ag-H₂O samples obtained from the bottom of centrifuge tube, the enthalpy did not reach zero even at the volume fraction as high as 15.6 vol.% (66 wt.%). The results of Ag-EG dispersion and Ag-H₂O dispersion suggested that EG is a better solvent than water, as Ag-EG dispersions can reach a liquid crystal phase at a much lower concentration. Comparing the data of the two kinds of Ag-EG dispersions showed the silver nanowires and nanospheres ratio and size of silver nanowires and nanosphere could also influence the liquid crystal phase formation.

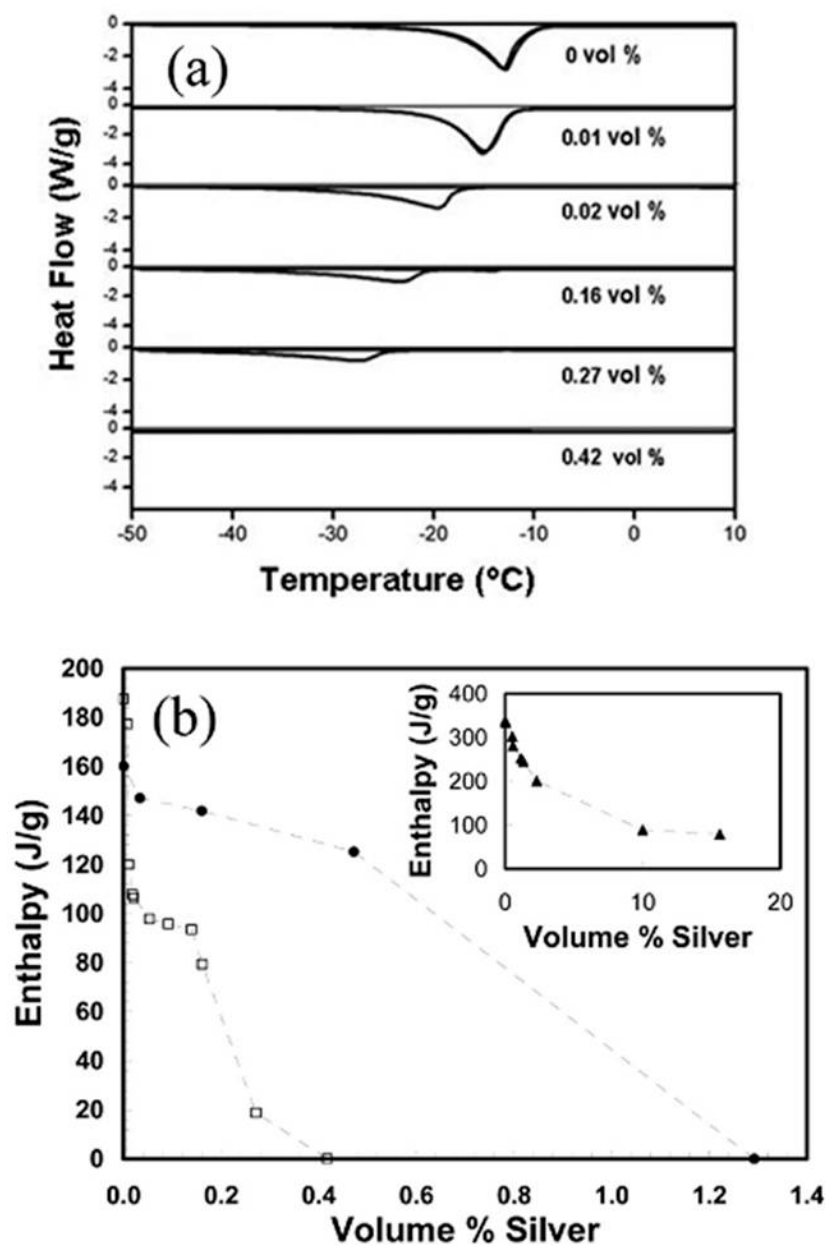


Figure 4.6 Differential scanning calorimetry of silver dispersions. (a) The shift in melting temperature and decrease in enthalpy for successively higher concentration of Ag-EG obtained through centrifugation and sampling the centrifuge tube sidewall. (b) Plot of enthalpy versus volume fraction for Ag-EG from the centrifuge tube sidewall shown in (a) (squares), a different region of the sidewall (circles), and the entire sediment of samples transferred to water Ag-H₂O (inset). Dashed lines are merely intended to guide the eye.³⁵

4.4 Rheology

4.4.1 Start-up of Shear

For liquid crystalline dispersions, the start-up of steady shear results in the viscosity and first normal stress difference oscillating for over 100 shear units (a shear unit is the product of shear rate and time). This behavior is very different from that of isotropic dispersions, where oscillatory transients last for a few shear units at most.¹⁰⁴ Unlike the inconsistent oscillations in low concentration biphasic dispersions, uniform and long oscillatory transients were found in all concentrated samples whose ϕ is higher than 1.90 vol.%. For example, Figure 3.6 shows the response to the start up of shear for a concentrated sample at 1.90 vol.% sheared at 1 s^{-1} . The response was in very uniform long oscillatory transients which persisted for over 1500 shear units for both viscosity and first normal stress difference. In this case, for silver nanowire dispersion at 1.90 vol.%, a true steady state measurement at a shear rate 1 s^{-1} was needed over 1500s (0.4 hours), at a shear rate of 0.1 s^{-1} was needed over 15,000s (4.2 hours), at a shear rate of 0.01 s^{-1} was needed over 150,000s (42 hours). This influences the accuracy of the viscosity versus shear rate curve. Taking Figure 4.7 at 1 s^{-1} shear rate as example, measurement of the crest and trough of the oscillatory will cause about 6.8 % difference. Due to sedimentation of the dispersions, it is impossible to do a true steady state measurement which needs hours to measure the viscosity at a certain shear rate and for days to measure the whole viscosity versus shear rate curve. Considering both the sedimentation effect and the time needed to reach steady state, measurement on the whole viscosity versus shear rate curve ($0.01\text{-}100 \text{ s}^{-1}$ shear rate) usually took several hours.

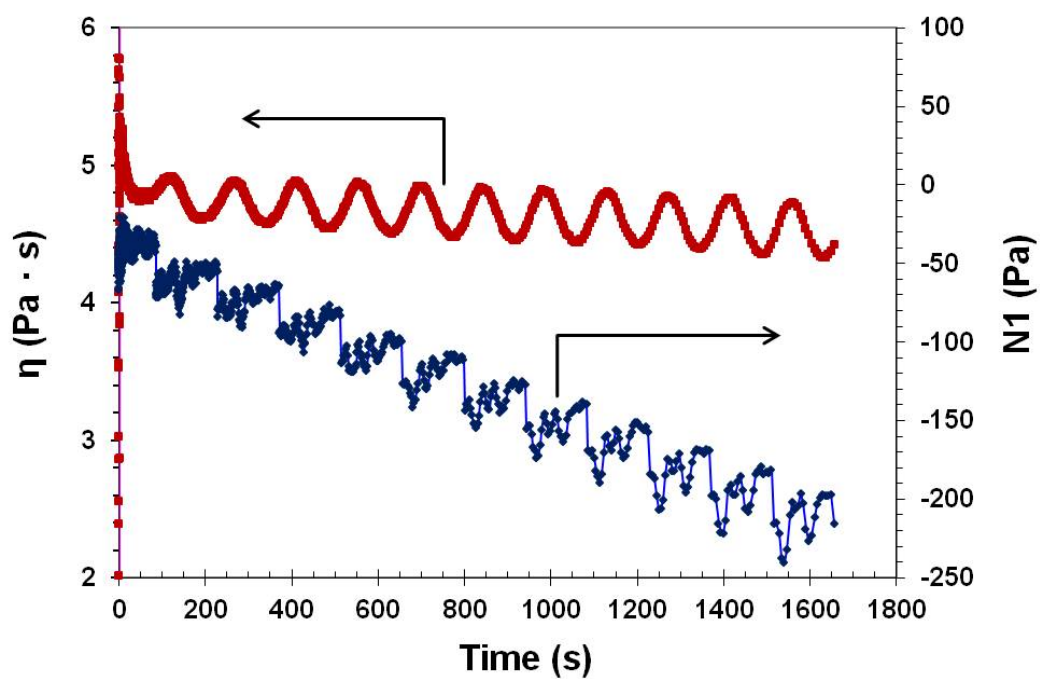


Figure 4.7 The response of the start up of shear for concentrated Ag-EG dispersion at 1.90 vol.% shearing at 1 s^{-1} shear rate shows a oscillatory of both viscosity and first normal force difference with time.

4.4.2 Steady Shear Rheology

Steady shear tests were performed for silver nanowire EG dispersions at different concentrations. A pre-shear at 1 s^{-1} for about 1000 s was applied to each experiment to ensure a well-defined shear history. The steady shear viscosities versus shear rate curves of dispersions at different concentrations are shown in Figure 4.8. At an Ag concentration of 0.6 vol. %, the dispersion was isotropic and behaved as a Newtonian fluid in the measured shear rate range. When the Ag concentration increased to 0.8 vol.%, the dispersions began to show a shear thinning behavior. The viscosity at a given shear rate kept increasing monotonically with silver concentration from 0.9 to 1.8 vol.%, the viscosity showed a maximum in the biphasic regime (Figure 4.8 a). Further increasing the Ag concentration caused the viscosity to decrease due to the increasing predominance of ordered domains (Figure 4.8 b). The viscosity reached the minimum at an Ag concentration of 2.2 vol.%, this is indicative of the ϕ_N transition to a completely liquid crystalline phase. After this transition point, the viscosity started to increase again with increasing Ag concentration. This nonmonotonic behavior of viscosity as a function of concentration can be better seen in Figure 4.9 at shear rate of 0.1, 1 and 10 s^{-1} . It shows that at each shear rate, viscosity versus concentration curves all go through a maximum, while the magnitude of the maximum steady shear viscosity is depressed. The transition from a biphasic system to a single phase liquid crystal occurs in the concentration range between the maximum and the minimum in viscosity.¹⁰⁶ In this case, an Ag-EG dispersion single phase liquid crystal could be obtained at a concentration between 1.9 vol.% to 2.9 vol.%. This is consistent with the optical microscopy result shown in Figure 4.5. It is interesting to note that the viscosity drops abruptly at the transition point, which has also been observed in PBLG lyotropic liquid crystals.⁷²

Furthermore, the viscosity versus shear rate curves in biphasic and entirely liquid

crystalline region showed a shear thinning behavior associated with a power law:

$$\eta = K\dot{\gamma}^{n-1}$$

where $\dot{\gamma}$ is the shear rate, K is the consistency coefficient and n is the rate index, $n < 1$ indicates shear thinning, $n = 1$ indicates to Newtonian, and $n > 1$ indicates to shear thickening behavior. For dispersions with Ag concentration from 0.8 vol.% to 1.6 vol.% and from 1.9 to 2.9 vol.%, the flow curve showed an inflection point which separated the curve into two different shear thinning regions. However, close to the maximum in biphasic region (1.7 and 1.8 vol. %) and high concentration liquid crystalline region (3.7 and 4.1 vol. %), the flow curve showed only one shear thinning region. Furthermore, the n was very close to 0, which results in $\eta \sim \dot{\gamma}^{-1}$. The consistency coefficient and rate index of each dispersion at Region I and Region III are summarized in Table 4-1. In general, the n values in Region I are lower than those in Region III for all dispersions with Ag concentration from 0.9 to 4.1 vol. %. This is consistent with previous observations for lyotropic polymer liquid crystals. For both Region I and III, the n value first decreased with the increasing Ag concentration, then increased with the increasing Ag concentration, and then decreased again. The transitions points are highlighted in Table 4-1. Interestingly, the transition points for both Region I and Region III are closed to the maximum viscosity in biphasic region and biphasic to entirely liquid crystalline transition.

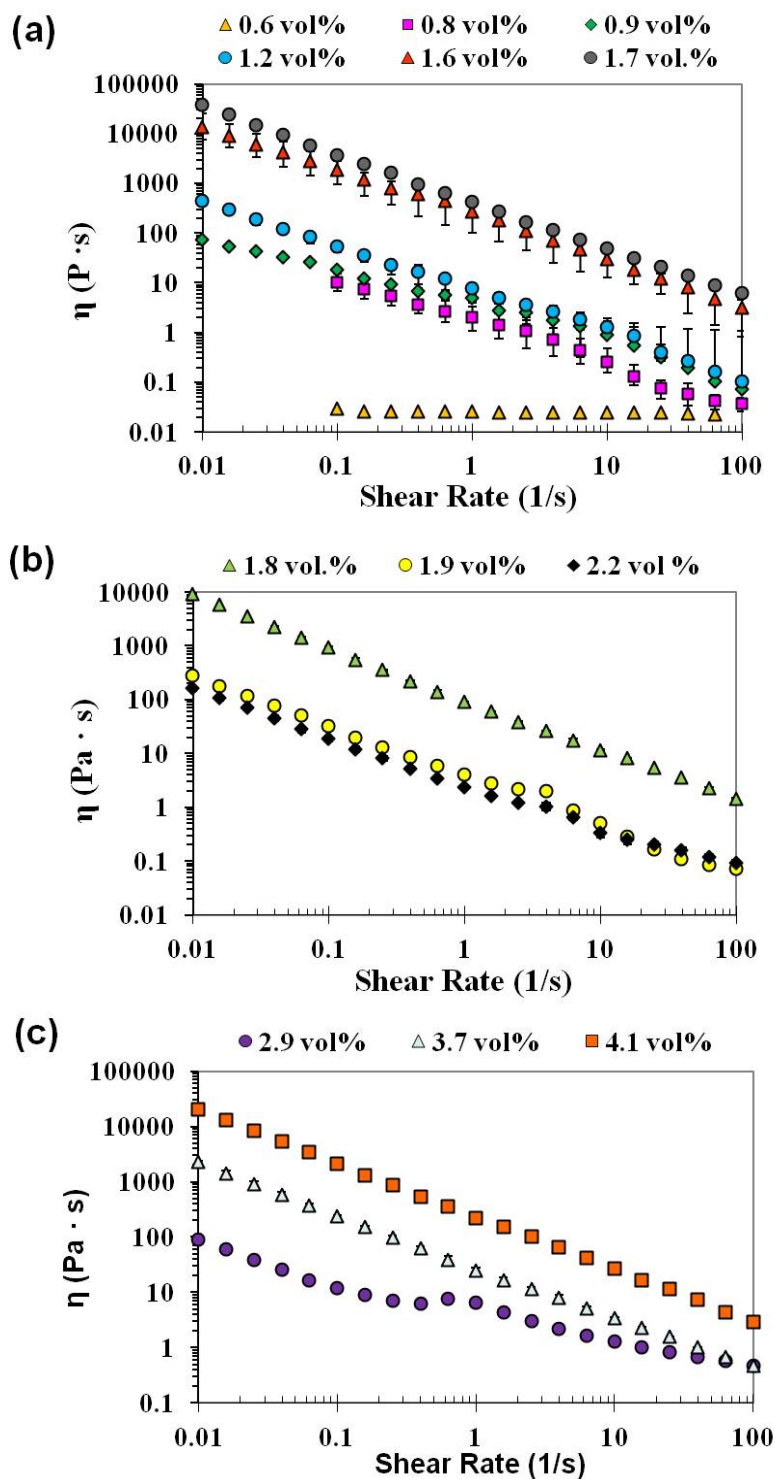


Figure 4.8 The steady shear viscosity of Ag-EG dispersions at (a) increasing region of viscosity versus concentration curve; (b) Decreasing region of viscosity versus concentration curve; (c) Entirely liquid crystalline region.

Table 4-1 Consistency coefficient and rate index of steady shear response of Ag-EG dispersion at different concentrations.

Ag Concentration (vol. %)	Regime I		Regime III	
	K	n	K	n
0.8	2.0	0.29	0.76	0.32
0.9	3.9	0.35	4.5	0.31
1.2	7.3	0.11	7.2	0.25
1.6	251.4	0.14	276.0	0.03
1.7	438.8	0.05	~	~
1.8	103.0	0.06	~	~
1.9	4.1	0.1	3.1	0.14
2.2	2.4	0.1	1.7	0.36
2.9	1.7	0.15	4.7	0.48
3.7	28.2	0.08	~	~
4.1	233.4	0.04	~	~

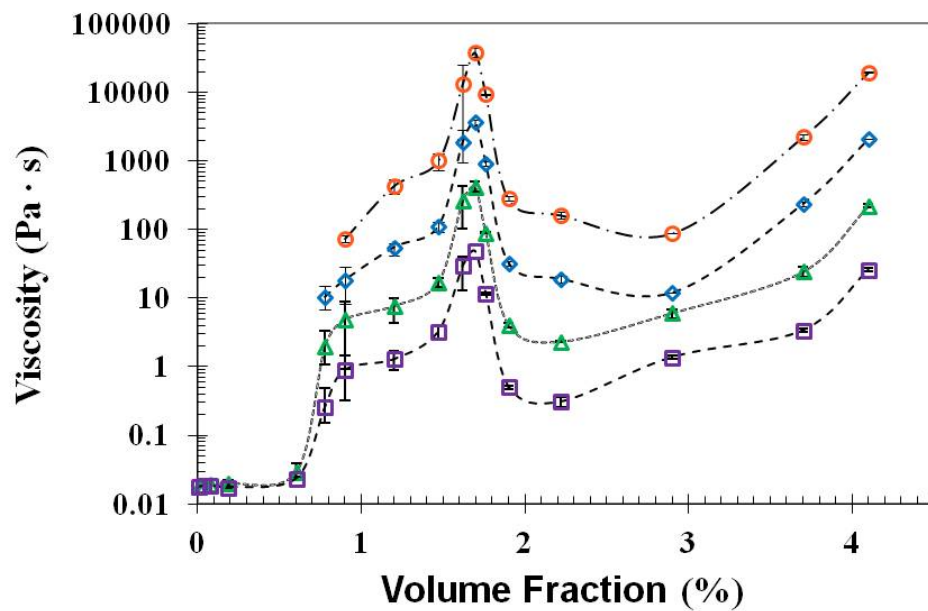


Figure 4.9 Relationship between viscosity and volume fraction of silver nanowires and nanospheres-ethylene glycol dispersions at a shear rate of 0.01 (orange circles), 0.1 (blue diamonds), 1 (green triangles), and 10 (orange circles) s^{-1} .

This behavior is similar to the three region behavior observed in some LCPs and is associated with a lyotropic nematic liquid crystal-polydomain texture.⁷⁸ For example, an Ag-EG dispersion at a concentration of 1.90 vol. % (Figure 4.10) showed the three region behavior with a very narrow Region II, at shear rate around 3 s^{-1} , which has also been observed in SWNT superacid liquid crystal dispersions.³⁰ It also shows that the power law coefficients are very different in Region I and Region III. In Region I, $\eta = 4.10 \dot{\gamma}^{-0.9}$ ($R^2=0.997$); at Region III, $\eta = 3.1 \dot{\gamma}^{-0.86}$ ($R^2=0.956$). This is consistent with the previous reports of Region I that the scaling of viscosity with shear rate follows a power law.⁷¹ Besides, the different scaling in Region I and Region III implies a different mechanism undergoing in this two shear thinning Region and also confirms the three Region behavior. Although, the origin of the three region curve is still partially understood, the shear thinning behavior in Region I is generally believed to be due to the tumbling of the nematic phases and is usually associated with a yield stress.

The plateau behavior in Region II is because of wagging of nematics due to the competition between tumbling and the flow alignment by shear force. In Region I and II, the polydomain structure is preserved in spite of the shear stress.¹⁰⁵ At higher shear rates in Region III, the flow orients the director in the shear direction throughout the dispersion, and polydomains of rods changes to an aligned structure.

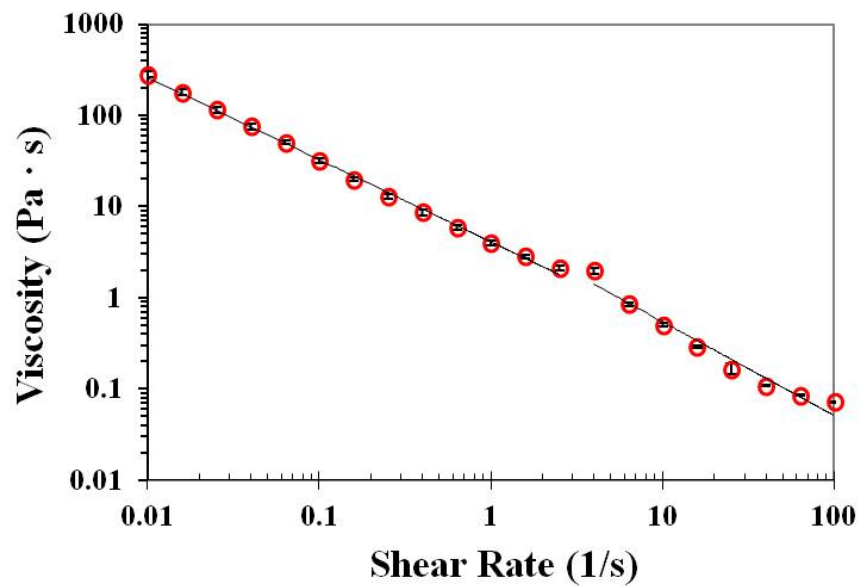


Figure 4.10 Viscosity versus shear rate curve of 1.90 vol.% silver nanowires and nanoparticles in ethylene glycol shows a three Region behavior.

The yield stress is the static stress required to deform the director field to one in equilibrium with the imposed flow. As shown in Figure 4.11, there is an obvious yield stress for Ag-EG dispersions with silver nanowire volume fractions higher than 0.8 vol.%. The dramatic change of viscosity versus shear stress curve between volume fraction of 0.6 vol.% and 0.8 vol.% is associated with the dispersion microstructure change shown in Figure 4.5. Furthermore, the yield stress of the Ag-EG dispersions also exhibits non-monotonic relationship with concentration shown in Figure 4.11. The yield stress reaches to the maximum at silver nanowire volume fraction of 1.7 vol.%, which is consistent with the viscosity versus volume fraction curve Figure 4.9.

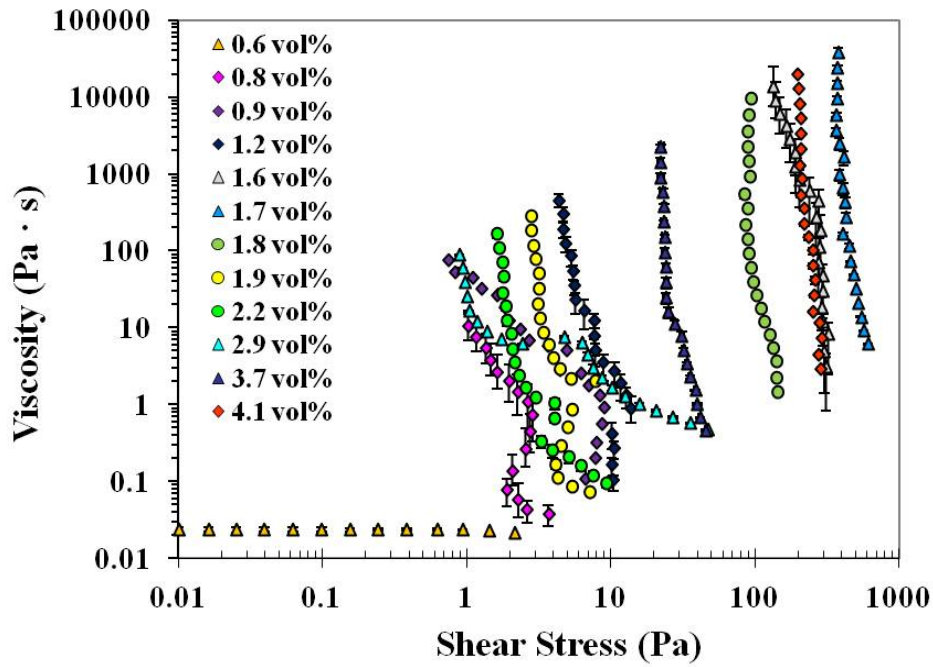


Figure 4.11 Viscosity versus shear stress curve of Ag-EG dispersions at different concentrations shows obvious yield stress at concentration higher than 0.8 vol.%.

The flow behavior of lyotropic liquid crystalline phases, which usually contain complicated microstructures, is strongly dependent on the shear history and original texture of the dispersion. Preshear is usually applied on the liquid crystalline dispersion before test to reduce the effects of the uncontrolled past history in order to get reproducible transient rheological data. Previous research has also shown that applying preshear, especially preshear at critical shear rate before test can help the observation of Region I.⁷¹ The preshear influence on the viscosity versus shear rate curve is studied on Ag-EG dispersion at 2.90 vol. % shown in Figure 4.12. Ag-EG dispersions with same concentration of 2.90 vol. % were loaded and applied with constant shear at 0.01, 0.1 or 1 s⁻¹ shear rate for 2000 seconds. The observation of low shear rate shear thinning behavior (Region I) is highly depend on the concentration of dispersion and shear history.⁵⁷ Previous experiments on liquid crystal polymers and nanocylinder liquid crystals, show Region I behavior can only be observed at high concentration liquid crystalline dispersion and applying preshear, especially preshear at critical shear rate before test can help the observation of Region I.⁷⁷ Comparing flow curve differences for same dispersion after preshearing at 0.01, 0.1 and 1 s⁻¹, shows shear history has critical influence on the rheological properties at low shear rate (Region I and II) but not high shear rate (Region III). It also shows applying preshear to a dispersion around the critical shear rate (shear rate in Region II) results in the viscosity in Region I being smaller than when the dispersion was not presheared with a critical shear rate.

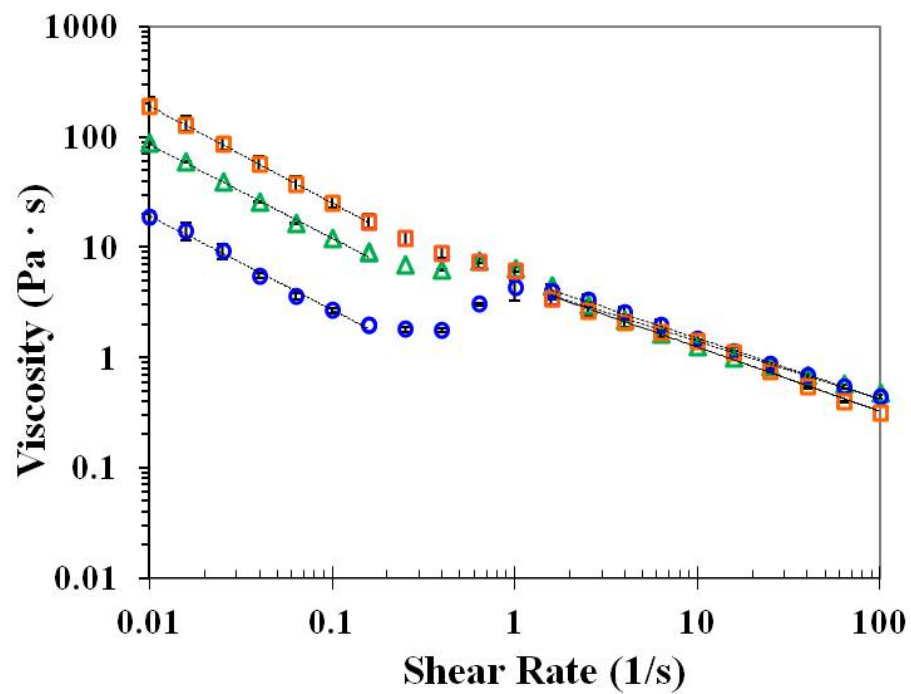


Figure 4.12 Viscosity versus shear rate curve of Ag-EG dispersion at 2.90 vol% after preshearing at 0.01 (orange squares), 0.1 (blue circles) and 1 s⁻¹ (green triangles) shear rate for 2000 s.

4.4.3 Cox-Merz Rule

Ordinary fluids follow the empirical Cox-Merz rule that the steady shear viscosity and complex viscosity at the same shear rate and angular frequency overlap. However, this rule is not obeyed for lyotropic liquid crystalline polymers in the anisotropic regime.^{57, 71} Not obeying the empirical Cox-Merz rule was observed for Ag-EG dispersions at silver volume fractions from 1.6 vol.% to 1.8 vol.%. Figure 4.13 shows an example of the failure of Cox-Merz rule for a Ag-EG dispersion with 1.6 vol.% silver. The dynamic viscosity versus frequency curves at lower concentrations were not obtained due to the insufficient torque. Interestingly, the two curves showed a bigger deviation at lower shear rate than that at higher shear rate. The failure of Cox-Merz rule is additional evidence of liquid crystalline phase formation in silver nanowire dispersions.

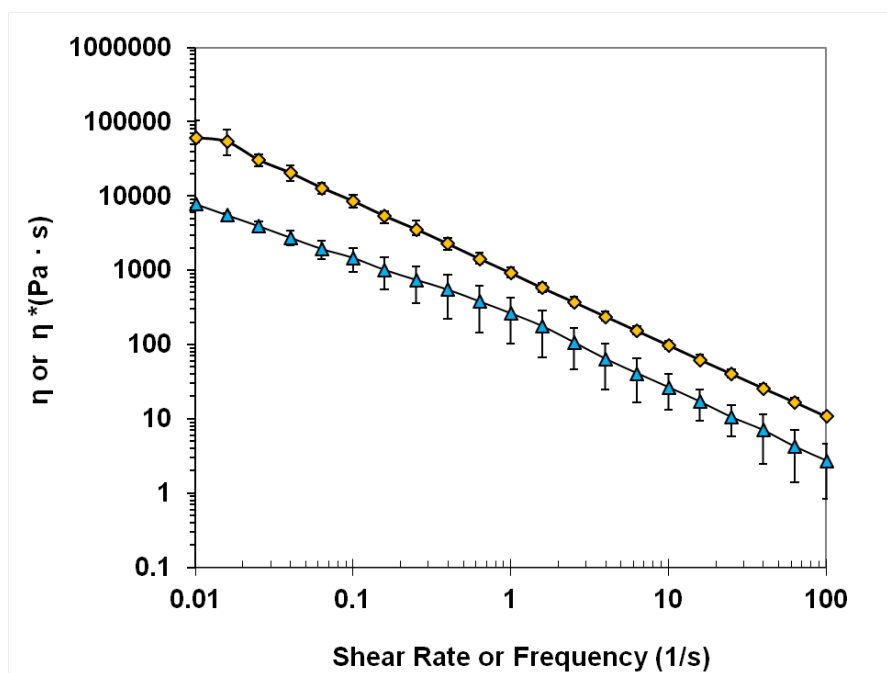


Figure 4.13. Cox-Merz rule not obeyed at silver concentration of 1.6 vol. % dispersed in EG. Constant shear viscosity (blue triangles) and complex viscosity (yellow diamonds).

4.5 Shear Induced Texture

4.5.1 Nanowire Concentration Influence on Texture

Processing of liquid crystalline dispersions to form coatings, films, or fibers typically involves the application of shear; therefore, it is important to understand the shear response of the systems. Shear alignment tests were performed on both isotropic and biphasic silver nanowire dispersions by both manually shearing or in a Linkam shear cell. The results were characterized by optical microscopy or SEM at room temperature. Ag-EG dispersions with 0.5 vol.% Ag (onset of biphasic region) and 1.0 vol. % Ag were both sheared with a controlled gap of 30 μm and controlled shear rate of 2000 s^{-1} in the Linkam shear cell and observed by optical microscopy. For a 0.5 vol. % Ag-EG dispersion, the cross polarized optical microscope images before and after shearing showed that significant amount of Ag nanowires aligned in one direction after shear; the birefringence was highly enhanced. (Figure 4.14 a, b). For a 1.0 vol. % Ag-EG dispersion, the optical images not only showed a greater alignment after shear, but also suggested a banded texture formation. Time-lapse images after cessation of shear showed the banded texture relaxing over time, but that the texture can still remain a long time after shear, which is due to the elastic energy stored in the bands.

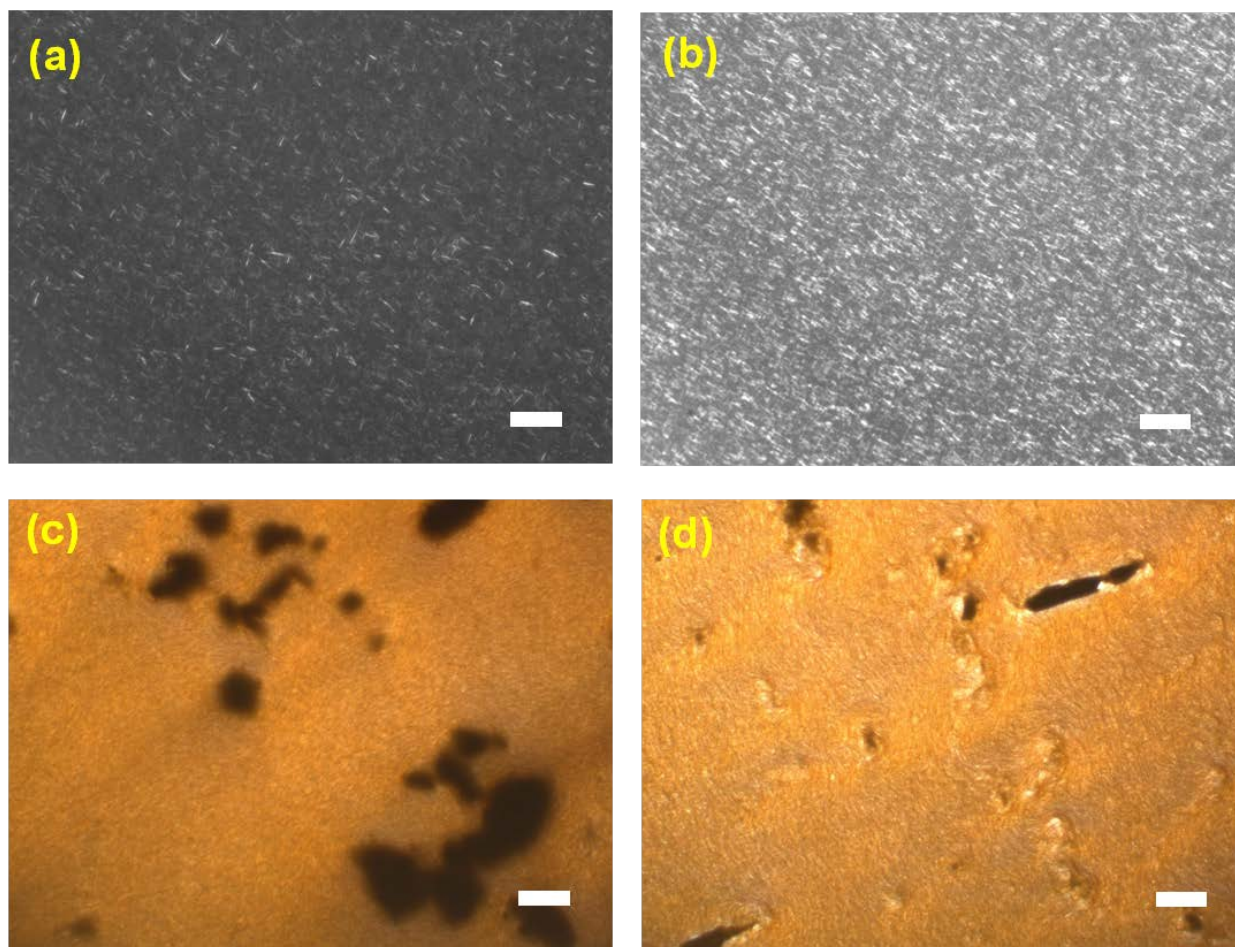


Figure 4.14 Cross polarized light optical microscopy images of (a, b) 0.5 vol. % and (c, d) 1 vol. % Ag-EG dispersion (a, c) before and (b, d) after shearing at 2000 s^{-1} shear rate. The scale bars are $20 \text{ }\mu\text{m}$.

4.5.2 Shear Rate Influence on Texture

Based on the previous research on liquid crystal polymers, it has been shown that the texture of liquid crystal dispersions is a function of shear rate. With increasing shear rate, the texture of domain along with the disclination array can be refined.^{107, 108, 109} After shearing at a relatively high shear rate of 200 s^{-1} , a worm texture was observed in biphasic Ag-H₂O dispersions. This shows the dispersion polydomain structure was retained due to the high disclination density associated with the relatively high shear rate.⁷¹ A worm texture is a constantly fluctuating of domain under flow; these textures have been previously observed in liquid crystalline polymers.^{107, 110} As shown by Figure 4.15, the densely packed disclinations are generally aligned along the shearing direction. This worm texture remained for several hours after cessation of shear and could be preserved during solvent removal. The high stability of the worm-like structure may be due to the large persistence length, high attractive interactions and the presence of the demixed nematic phase.³⁵ These factors may also explain why the worm-like texture was obtained at much higher shear rate than the 1 to 100 s^{-1} typical shear rate range for liquid crystalline polymer.^{57, 107, 111}

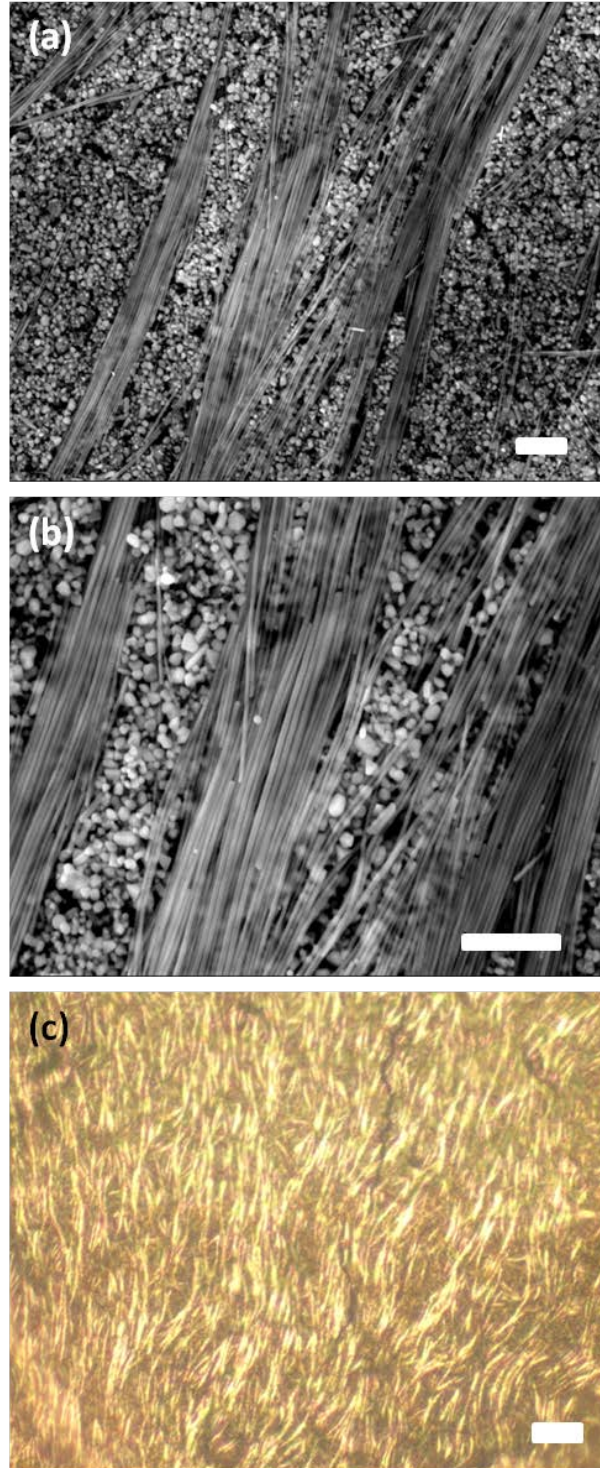


Figure 4.15 (a)(b) SEM images of dried coating made by shearing Ag-H₂O dispersion with initial concentration 1.0 vol.% at 200 s⁻¹ shear rate showing a worm-like texture with the disclination aligned in the shearing direction. (c) Optical image of same coating under cross-polarized light using a 20x DIC 0.45 NA objective and 2x additional magnification in front of the camera. Scale bars are 1 μ m in (a) and (b); 20 μ m in (c)

Shearing the same sample at 900 s^{-1} and then drying at the same condition resulted in a finer texture with more uniform alignment and fewer disclinations as shown in Figure 4.16. The higher shear rate also increased the segregation of the nanowires and nanoparticle aggregates. The nanowires aligned along the shear direction on the top of coating and the nanoparticle aggregates segregated to the bottom of the coating. This is consistent with the suggestion by Alderman and Mackley that with increasing shear rate, the domain size will become smaller, until at a critical shear rate, uniform monodomain structure with molecules aligning along the shear direction can be obtained.¹⁰⁷

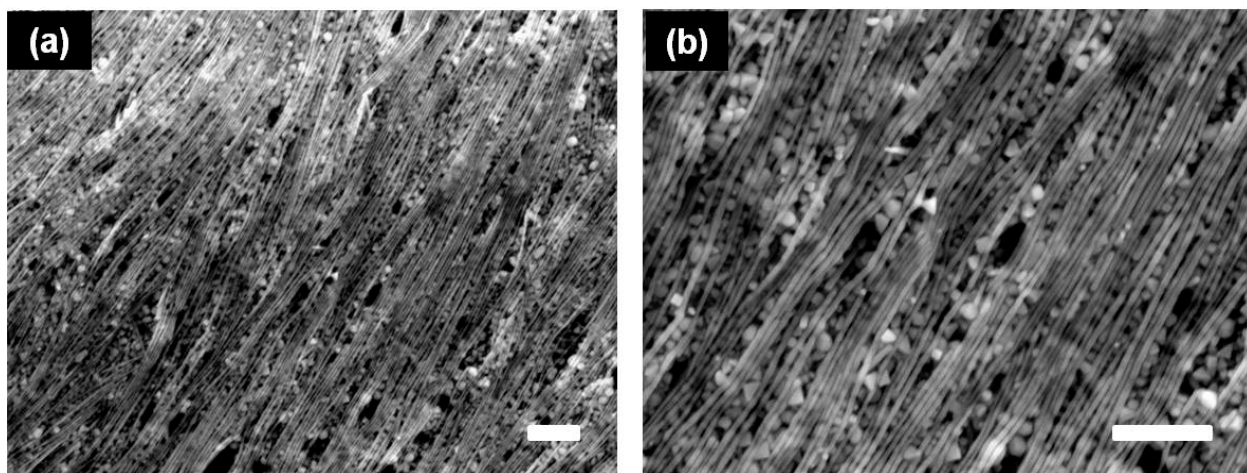


Figure 4.16 Scanning electronmicroscopy images of dried coating made by shearing Ag-H₂O dispersion with initial concentration 1.1 vol% at 900 s^{-1} shear rate showing a monodomain aligned in the shearing direction. Magnifications are (a) $10,000\times$ and (b) $20,000\times$. All scale bars are $1\text{ }\mu\text{m}$.

4.5.3 Shear Band Textures

Shear band textures are interesting structures that can form after cessation of shear or even during shear. They were first observed in liquid crystalline dispersions used to make KevlarTM fibers.¹¹² They are commonly found in both thermotropic and lyotropic liquid crystal systems after processed by thin-film shearing,^{89, 113} uniaxial fiber drawing,¹¹⁴ and injection molding.¹¹⁵ They can be observed using either dark field transmission electron microscopy or polarized light microscopy. Dark bands lie perpendicular to the direction of shear, and represent a periodic fluctuation of molecules aligned around the shear direction. This periodic oscillation of molecules ordering director is induced by the strain relaxation (stored elastic energy of the texture) after cessation of shear,^{107, 116} or during continuous shear.^{89, 117}

Dried thin films with 1–2 μm thickness made by unidirectional shearing of 0.8 vol. % silver nanowire and nanosphere aggregates water biphasic dispersion at 500 s^{-1} showed a banded texture. Here, the tilt angle of molecules relative to the shearing direction was determined using the method introduced by Wang et al.¹¹⁸ In this method, the polarizer and analyzer are kept crossed all the time, the bands are perpendicular with either the polarizer or analyzer at the starting point, and then the microscope stage is rotated to make the image change as a function of angle. When the molecules in certain bands are aligned with either polarizer or analyzer, the bands will appear completely dark. The tilt angle can then be calculated by the rotated angle of the stage. In this case, when the polarizer and analyzer are crossed, and the direction of shear is parallel to the polarizer direction, the polarized light microscopy image in Figure 4.17 (a) exhibited bright bands and dark lines which are alternate and perpendicular with the shear direction (stage angle equal to 0°). When the microscopy sample stage was rotated clockwise (appeared counterclockwise in Figure 4.17 (b) due to the inversion by lens) with an angle θ of 53° the bright bands alternatively

turned to completely dark, while the half of the bands are still bright as shown in Figure 4.17 b. While when the stage was rotated counterclockwise with an angle θ of 53° , the dark bands shown in Figure 4.17 b turned to bright and the bright bands in Figure 4.17 b turned to dark as shown in Figure 4.17 c. This method can be used to measure the molecular tilt angle relative to the shearing direction. In this case, the tilt angle α of molecules relative to the direction of shear can be calculated as $\alpha = 90^\circ - \theta$, which equals to 37° . For polymer liquid crystals, the band size was found to be a function of shear rate, polymer molecular weight, sample thickness, solution concentration, type of solvent and solvent evaporation rate etc.^{118,119} In this study, silver nanowire thin films made by shearing 0.8 vol.% Ag-H₂O biphasic dispersions with a dispersion thickness of 300 μm at 500 s^{-1} showed a band size from 10 to 70 μm . This band size range is significantly bigger than 4–10 μm the band size reported for a model system, aqueous hydroxypropyl cellulose (HPC). This is possibly due to the significant higher persistence length of silver nanowires. It is noted that the Ag-H₂O banded texture was only observed at shear rates higher than 200 s^{-1} . This is consistent with previous observations on HPC, which showed that the banded texture can only form when the magnitude of shear rate exceeded a certain threshold value.^{116, 120, 121}

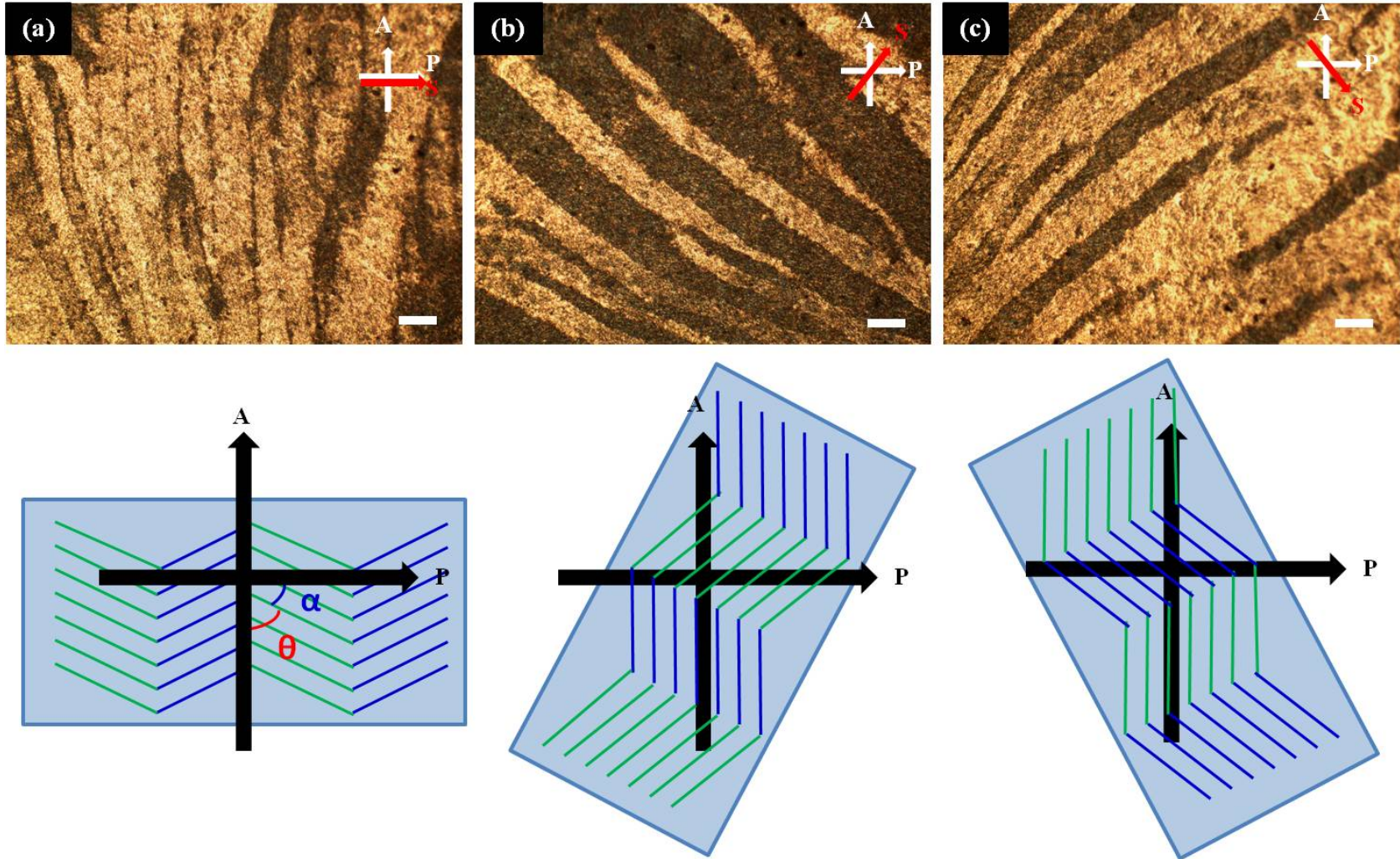


Figure 4.17 Banded texture of silver nanowire thin film made by unidirectional shear and dried in vacuum oven and then observed under cross polarized light microscopy. (a) Direction of shear parallel to the polarizer; (b) Stage was rotated clockwise with 53° ; (c) The stage was rotated counterclockwise with 53° . All scale bars represent $40\text{ }\mu\text{m}$. A: analyzer; P: polarizer; S: direction of shear.

4.6 Coating Fabrication

4.6.1 Drop Casting

Drop casting is an important small scale fabrication method for inkjet printing, washing and coating processes. It has been used for small scale assembly of both colloidal particles and nanoparicles. Drop casting of anisotropic nanomaterials including single-walled and multi-walled carbon nanotubes,^{122, 123} gold nanorods,¹²⁴ and CdSe nanorod resulted in coffee ring structure formation with nanotubes/nanorods aligning parallel to the edge of the droplet. In this research, drop casting was investigated for the Ag-H₂O system. A 0.8 vol.% Ag-H₂O disperison was dropped on a SEM stub and vacuum dried at 80 °C and -25 mmHg for over 10 hours. The morphology of the dried coating was then characterized by SEM. The SEM images show the dried coating made from 0.8 vol.% Ag-H₂O with few liquid crystalline domains had little alignment. There was also no coffee ring structure formation in this system. This is possibly due to the capillary force itself being insufficient to carry the Ag nanowires with their relatively large diameter, high aspect ratio, and long persistence length to the contact line. Furthermore, it is also possible that the nanoparticle aggregates with larger diameter prevented capillary force induced motion of the nanowires. This is consistent with a recent study on polystyrene colloidal particles.¹²⁵ It showed that the aspect ratio affected the coffee ring structure formation. High aspect ratio ellipsoids with strong long-range interparticle attractions led to a loosely packed structure rather than coffee ring structure.

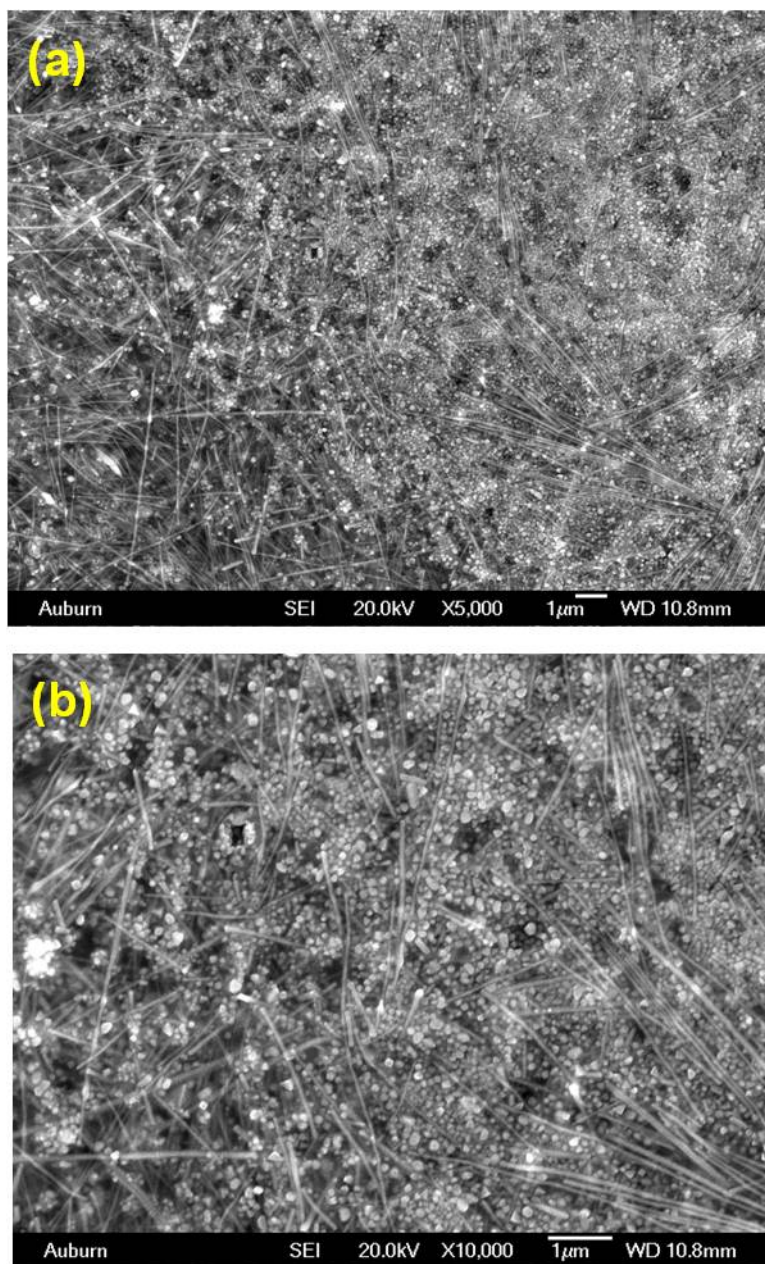


Figure 4.18. Scanning electron microscopy images of drop casting dried samples from Ag-H₂O dispersions with 0.8 vol. % Ag showing a low degree of alignment.

4.6.2 Shear Alignment

Since capillary force itself is insufficient to align silver nanowires, external shear force was applied to enhance the alignment between domains. Two Ag-H₂O dispersions with 0.16 vol.% (isotropic) and 0.88 vol.% (biphasic) Ag were dropped on SEM stub, sheared at the same rate and then vacuum dried at 80 °C and -25 mmHg for over 10 hours. Dried samples were then imaged by SEM and imaged at 10, 000 and 20, 000 magnifications. As shown in Figure 4.19 a,b, coatings made by applying shear to a predominantly isotropic Ag-H₂O dispersions ($\phi = 0.16$ vol.%) resulted in little alignment. However, as shown in Figure 4.19 c,d, the same method resulted in significant alignment when starting from largely birefringent Ag-H₂O dispersions with $\phi = 0.88$ vol.%. Furthermore, higher concentrations showed a greater extent of nanowire-spherical aggregate demixing. At the higher concentrations, the system was almost fully demixed after shear with the aligned nanowires ordering themselves above the spherical aggregates. These results suggest that shearing the biphasic dispersion with initially ordered microstructure is easier to produce dried coating with significant alignment than shearing isotropic dispersion. The higher viscosity and elastic energy stored in the biphasic dispersion facilitated the segregation of nanowires and nanoparticle aggregates and helped retain the alignment structure during solvent removal.

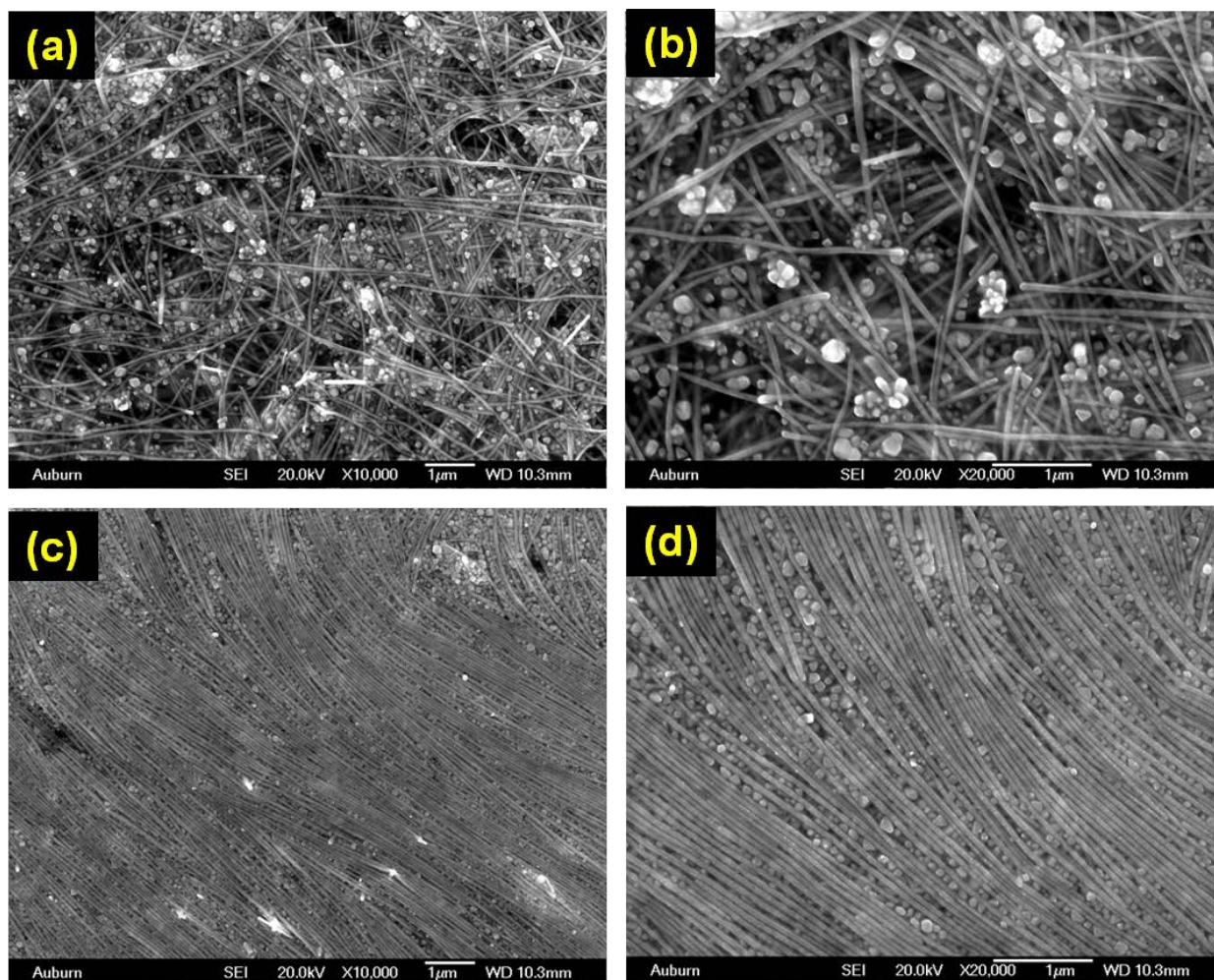


Figure 4.19. Scanning electron microscopy images of sheared and dried samples from Ag-H₂O dispersions showing a lower degree of alignment and demixing at lower concentrations: (a, b) initial concentration 0.16 vol% (1.7 wt%); (c, d) initial concentration 0.88 vol% (8.5 wt%). Magnifications are 10 000x in (a, c) and 20 000x in (b, d). All scale bars are 1 μm .³⁵

4.7 Alignment Characterization

While SEM provides a visual image of the degree of alignment, each image can only provide information in a limited area. Polarized Raman spectroscopy was used to quantify the alignment of silver nanowires and in the coatings. Dried coatings made from dispersions with 0.16 vol.% Ag and 0.88 vol.% Ag were characterized by polarized Raman spectroscopy, as shown in Figure 4.20. The combination of carbonyl strength ν (C=O) at $\sim 1600\text{ cm}^{-1}$, and the (CH₂ bend) at $\sim 1350\text{ cm}^{-1}$ indicated that there are small amount of PVP left on the surface of silver nanowires, which was consistent with the SEM images shown in Figure 4.2 d. Similar to the Platinum (Pt) enhanced Raman spectra,¹²⁶ a strong red shift of the PVP carbonyl frequency on the order of 70 cm^{-1} indicates the formation of C=O–Ag bonds. For free PVP the carbonyl vibration was at 1667 cm^{-1} . It is interesting to note that the ratio of intensities $I(\text{C=O}) / I(\text{CH}_2\text{ bend})$ for both coatings is higher than 1, which is opposite with the pure PVP Raman data, while consistent with the Pt enhanced PVP spectra.¹²⁶ This suggests a selective enhancement of C=O stretching than CH₂ bending. Similar to Pt-PVP system, both the red shift of the carbonyl and the selective enhancement of C=O bond suggest that PVP adheres to the nanoparticles through a charge-transfer interaction between the pyrrolidone rings and surface Ag atoms.¹²⁶

The relative alignment ratio was obtained by measuring the Raman spectroscopy intensity of the coated PVP at 0° , 45° , 90° orientation (Figure 4.20). The highest signature peak ($\sim 1600\text{ cm}^{-1}$) intensity of PVP was from 45° ; while the lowest intensity of PVP was from 0° . The relative degree of alignment I^{45}/I^0 of the sample shown in Figure 4.19 c, d is 11:1, indicating a significant degree of alignment; this compares to less than 2:1 for the samples shown in Figure 4.19 a, b.

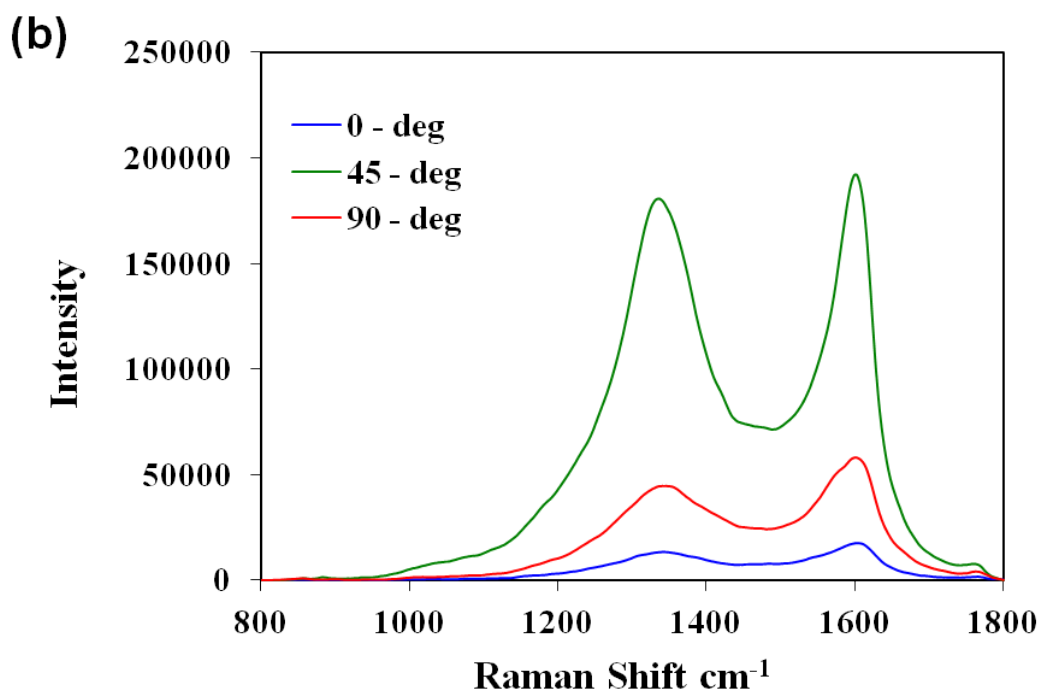
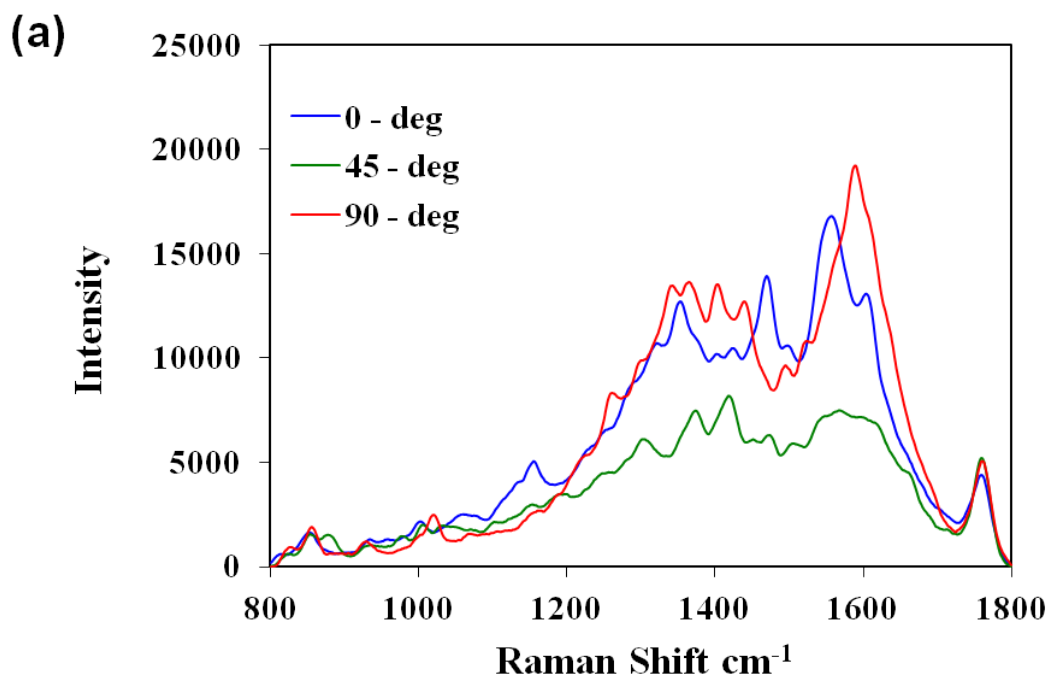


Figure 4.20 Polarization dependence of Raman spectra of dried coating made from dispersion with (a) initial concentration 0.16 vol. %; (b) initial concentration 0.88 vol. % at various angles with respect to the electric field vector.³⁵

4.8 Electrical Properties

The electrical resistivity of the silver nanowire thin film with shear banding texture shown in Figure 4.17 was characterized by four-point probe station in both the parallel and perpendicular direction relative to the silver nanowire alignment. The geometric correction factor F , which is usually required for sheet resistance calculation by four-point probe method, was simplified to $F = \frac{t/s}{\ln(2)}$, t is the thickness of the thin film and s is the probe spacing. Based on the measured voltage/current ratio $\frac{V}{I}$, the sheet resistances for thin film were calculated by the equation $R_{sh} = 2\pi s/t F \frac{V}{I}$, so $R_{sh} = \frac{\pi}{\ln(2)} \frac{V}{I}$. The extracted sheet resistance and corresponding resistivity of silver film in the direction parallel to the alignment $R_{sh\parallel} = 0.71 \Omega/sq$, $\rho_{\parallel} = 95 \mu\Omega \cdot cm$, while the sheet resistance in the direction perpendicular to the alignment $R_{sh\perp} = 1.3 \Omega/sq$, $\rho_{\perp} = 221 \mu\Omega \cdot cm$. The sheet resistance and resistivity in both direction are much smaller than the previous report on silver nanoparticle thin films.¹²⁷ The ratio of resistivity perpendicular/parallel to the alignment direction is about 2.3. The higher resistivity of Ag thin film than bulk Ag is due to both the PVP coated on the Ag surface and the small thickness. However, the silver thin film with anisotropic electric property has potential applications in anisotropic opto-electronics.⁵

4.9 Conclusion

The results in this chapter built on previous work.³⁵ Together these works provide a foundation for coupled liquid crystalline self-assembly and flow alignment of high aspect ratio inorganic nanowires. We have demonstrated liquid crystalline phase formation in a highly polydisperse system of silver nanowires and spherical nanoparticle agglomerates dispersed in ethylene glycol or water. The microstructure and phase behavior of dispersion was shown to be a function of silver nanowire and nanosphere volume fraction. Shearing predominantly isotropic dispersions resulted in little demixing or alignment. However, shearing predominantly liquid crystalline dispersions resulted in coatings with significant alignment and demixing. A worm-like texture of silver nanowires by applying shear with 200s^{-1} shear rate on the silver nanowire biphasic dispersion, and this texture are proved to be stable enough to persist for several hours. Further increasing the shear rate resulted in a banded texture with silver nanowires forming an uniform alignment at the top of the coating and nanospheres being segregated to the bottom of the coating. Such aligned coatings have potential applications as SERS substrates, opto-electronics, and antimicrobial coatings.

Chapter 5 Silica Nanorods Smectic Liquid Crystal

5.1 Shape and Size Distribution of Silica Nanorods

As shown in Figure 5.1, the nanorods are generally rod shaped. However, they can be classified more specifically to two typical shapes: tapered rod with two rounded ends and bullet-shape rod with one rounded end as reported by Kuijk.^{55, 128} The silica nanorod size and shape distribution were measured after removing the residual reactants but before the fractionation process, and also after the fractionation process. The size and shape measurement on silica nanorods after the original synthesis was not obtained due to large amount of residual PVP and other chemicals embedded the silica nanorods. Measurements made on more than 500 nanorods after the removal of residual reactants but before fractionation process showed the polydispersity: $\langle L \rangle = 0.95 \mu\text{m}$ with length standard deviation $\delta_L = 0.43 \mu\text{m}$, and $\langle D \rangle = 227 \text{ nm}$ with diameter standard deviation $\delta_D = 46 \text{ nm}$. The removal of small rods during the fractionation procedure, resulted in $\langle L \rangle = 1.23 \mu\text{m}$ and $\langle D \rangle = 255 \text{ nm}$, with $\delta_L = 0.35 \mu\text{m}$, $\delta_D = 55 \text{ nm}$. This results in an average aspect ratio of $L/D = 5.0$ with $\delta_{L/D} = 1.0$. Fractionation reduced the length polydispersity $\sigma_L = \delta_L/L$ from 46% to 27%, but had little effect on the diameter polydispersity which changed from 20% to 22%. The system is particularly intriguing because of the few detailed studies of smectic nanorod phases and the fact that the average aspect ratio is near theoretical lower Onsager limit of 4.1 for smectic phase formation and 4.7 for nematic phase formation in systems of uniform hard spherocylinders.¹²⁹ Also, as pointed out by Vroege et al, length polydispersities above 18% have been believed to theoretically preclude smectic phase formation.²¹

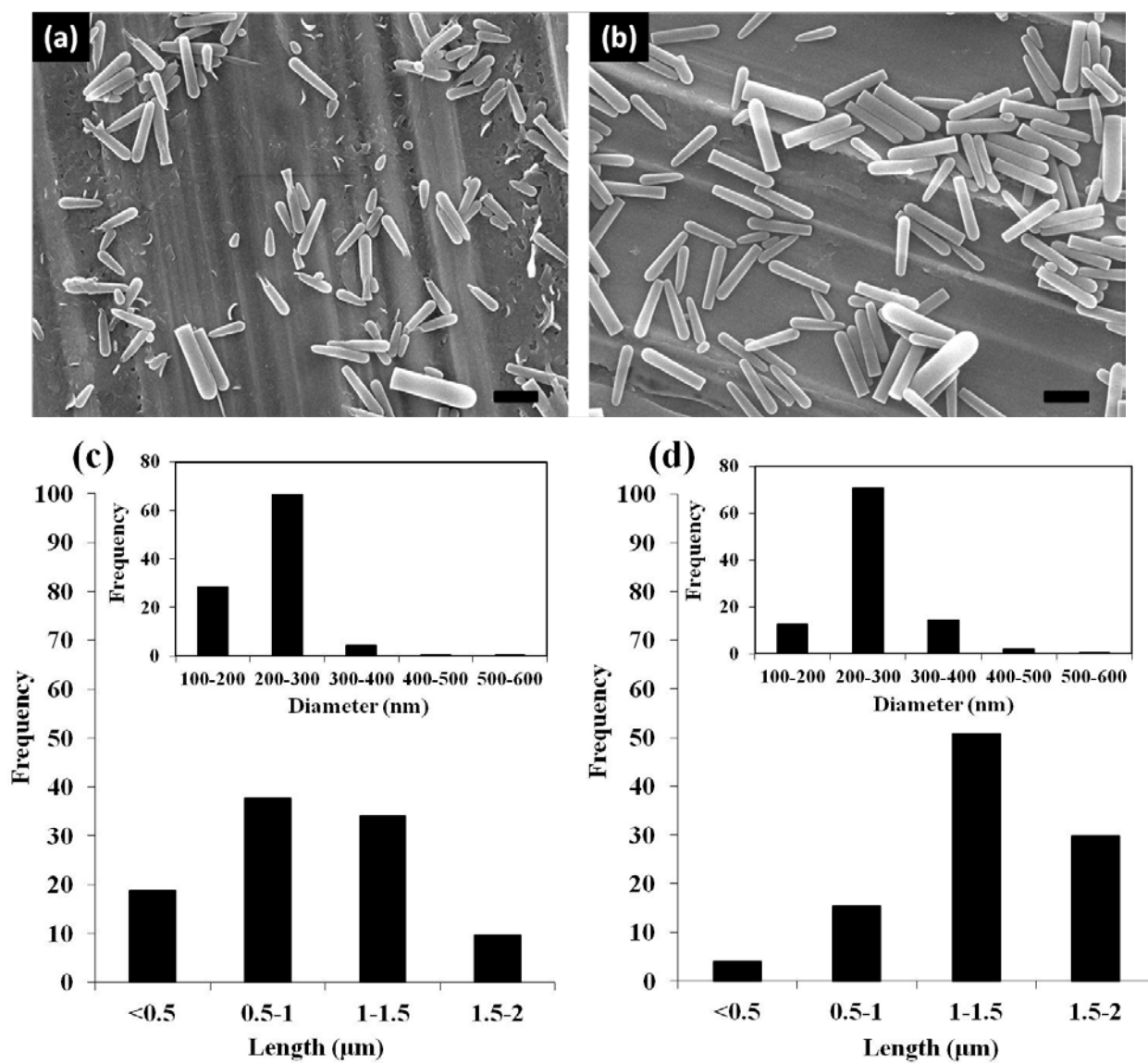


Figure 5.1. SEM images of silica nanorods (a) before and (b) after fractionation process by centrifugation. Histogram of lengths and diameter (insert) distribution of silica nanorods (c) before and (d) after fractionation process. The scale bar is 1 μm.

Furthermore, the shape dependence of the nanorods on length distribution was evaluated by the taper degree (defined as $\text{taper} = D/H$). In general, the rods were ~64% tapered rods and ~36% bullet-shaped rods. The bullet shaped rods typically had a longer length than the tapered rods. All the tapered rods were shorter than 1.5 μm , while 84 % bullet-shaped rods were longer than 1.5 μm . For bullet-shaped rods, the diameter throughout the entire rods was extremely uniform with a taper degree below ~3%, and cone angle below 1°. In contrast, for the tapered rods, the diameter difference throughout the entire rod and was highly dependent on the length of the rods. Figure 5.2 shows the taper degree and cone angle dependence on the length range (including both tapered rods and bullet-shape rods). It shows the taper degree and the cone angle both increased with decreasing rod length. Especially, for nanorods longer than 1.5 μm , the taper degree was smaller than 3%, and the cone angle is smaller than 1°, For the nanorods shorter than 0.5 μm , the taper degree was as high as ~15% with the cone angle ~8°.

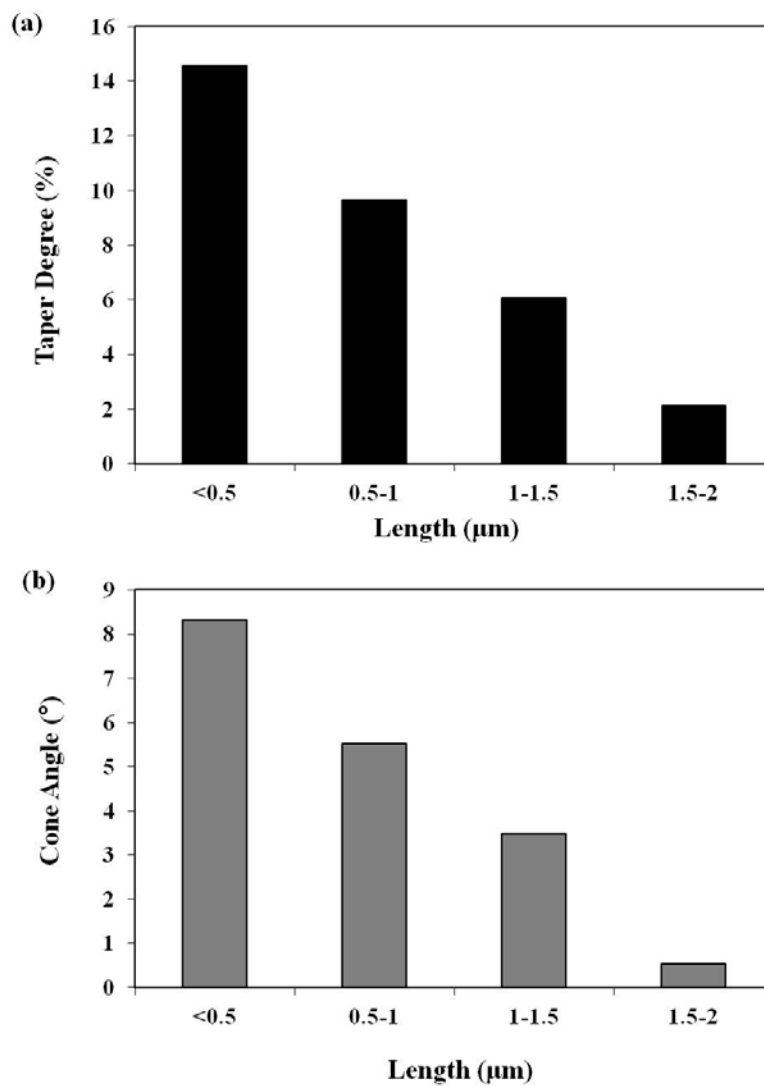


Figure 5.2. (a) Taper degree and (b) cone angle of silica nanorods after fractionation process at each length range.

5.2 Silica Nanorod Characterization

5.2.1 UV-Vis Absorbance

Bulk silica glass has no UV absorption for light between 200-900 nm wavelength.¹³⁰ However, silica nanoparticles have UV absorption around 210 nm wavelength.¹³¹ For the silica nanorods used in this research with an average diameter of 255 nm and average length of 1.3 μm , the UV absorption was at ~ 200 nm shown in Figure 5.3 (a). For all the solvents tested: pure DMSO, pure H_2O DMSO/ H_2O at 90/10 and 80/20, the UV absorption of silica nanorods was proportional to concentration; the dispersions obeyed the Beer–Lambert law (Figure 5.3 (b)). Thus, UV-Vis absorption here is used to measure silica nanorod concentration in the dilute region. Figure 5.3 shows a typical UV-Vis absorbance and related calibration curve of silica nanorods dispersed in DMSO/ H_2O at 80/20 dispersions.

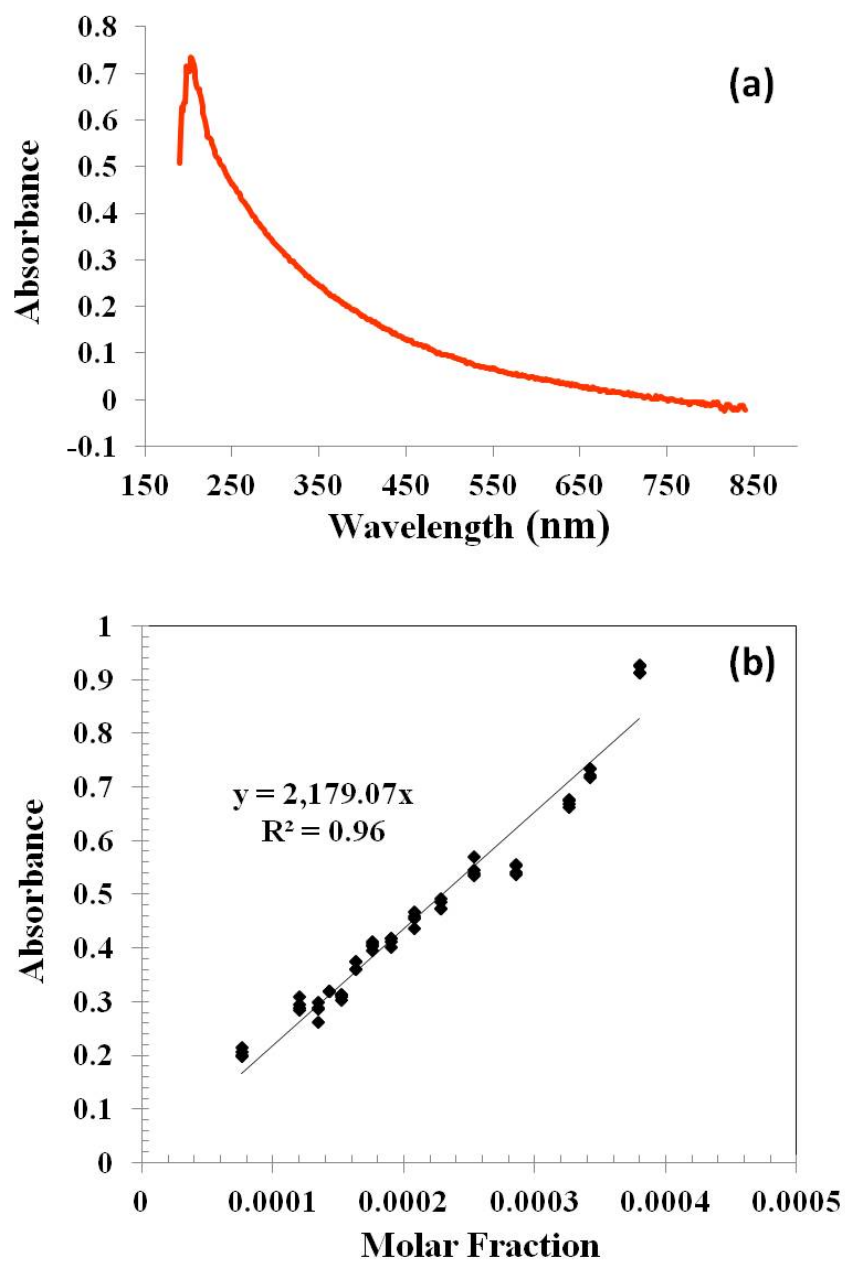


Figure 5.3. (a) UV-Vis absorbance of silica nanorod dispersed in 80/20 DMSO/H₂O. (b) UV-Vis calibration curve of silica nanorods dispersed in 80/20 DMSO/H₂O at 202 nm wavelength.

5.2.2 Raman Spectra

A Raman spectra of silica nanorod-DMSO dispersion after freeze drying is shown in Figure 5.4. The combination of carbonyl strength $\nu(\text{C}=\text{O})$ at $\sim 1600\text{ cm}^{-1}$, the $(\text{CH}_2\text{ bend})$ at $\sim 1440\text{ cm}^{-1}$ and the C-H strength even at $\sim 2900\text{ cm}^{-1}$ are indicate that small amount of PVP is still left on the surface of silica nanorods after several times washing process. The shift of C=O from the literature reported value 1680 cm^{-1} to 1600 cm^{-1} is possibly the result of the adsorbed of water in the system.¹³² The present of PVP is further evidenced by the ratio of intensities $I(\text{C}=\text{O}) / I(\text{CH}_2\text{ bend})$ is less than 1.¹²⁶ The peaks at 680 cm^{-1} indicate that certain amount of DMSO from the dispersion may still remain in the dry coating. The multiple peaks in the range of $300\text{-}500\text{ cm}^{-1}$ is an evidence of Si-O-Si bond. However, the detailed relative peaks intensity and shape highly depend on the structure of silica compound, and can be used to identify the crystal matrix structure.¹³³

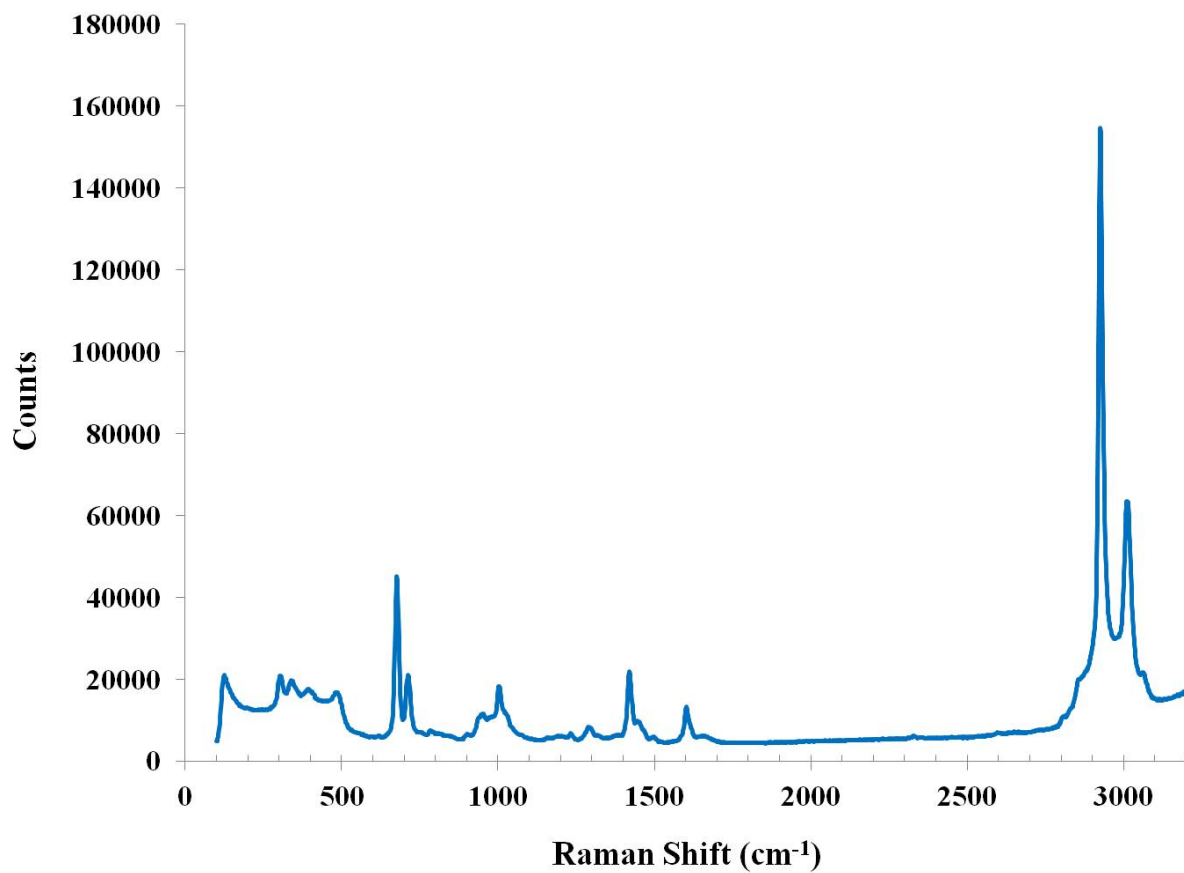


Figure 5.4. Raman spectra at 514 nm excitation of silica nanorod dry coating with the Raman shift range of 100-3200 cm⁻¹

5.3 Solvent Effect on Silica Nanorod Dispersion

5.3.1 Solvent Effect on Dispersion Stability

Large scale assembly of nanocylinders usually requires a liquid phase processing method. Difficulties in this process include the maximum concentration of the nanocylinders that can be stably dispersed. To evaluate the solvent quality of DMSO and H₂O, the solubility of silica nanorods dispersed in 80/20 DMSO/H₂O and pure H₂O were investigated by performing sedimentation studies and spectroscopy characterization. A mixture of 80/20 DMSO/H₂O was used instead of pure DMSO, because pure DMSO easily absorb the moisture, which can result in unintended variations in solvent composition. Figure 5.5 (a) shows a UV-vis absorbance of the supernatant of silica-H₂O dispersion over time under sedimentation. The silica nanorod concentration of the supernatant decreased overtime. It is noted that the silica absorbance peak shift to lower wavelength, which indicates there are shorter rods left at the top layer. This is because the rods with higher aspect ratio self-assemble to liquid crystalline domain prior than the shorter rods.⁶⁷ Figure 5.5 (b) shows the silica nanorod concentration change with time during sedimentation process for silica nanorods dispersed in 80/20 DMSO/ H₂O and pure H₂O. For the two different solvents, the rate of sedimentation associated with stability of the dispersions is different, leading to different sedimentation curves. It shows that silica nanorod dispersed in 80/20 DMSO/H₂O sedimentated much slower than dispersed in pure H₂O. Besides, more silica nanorods can be stabilized by 80/20 DMSO/ H₂O (~0.6 vol. %) than pure H₂O (~0.003 vol. %). It is clear that DMSO is better solvent than H₂O, since the dispersion is more kinetically stable and can disperse more silica nanorods.

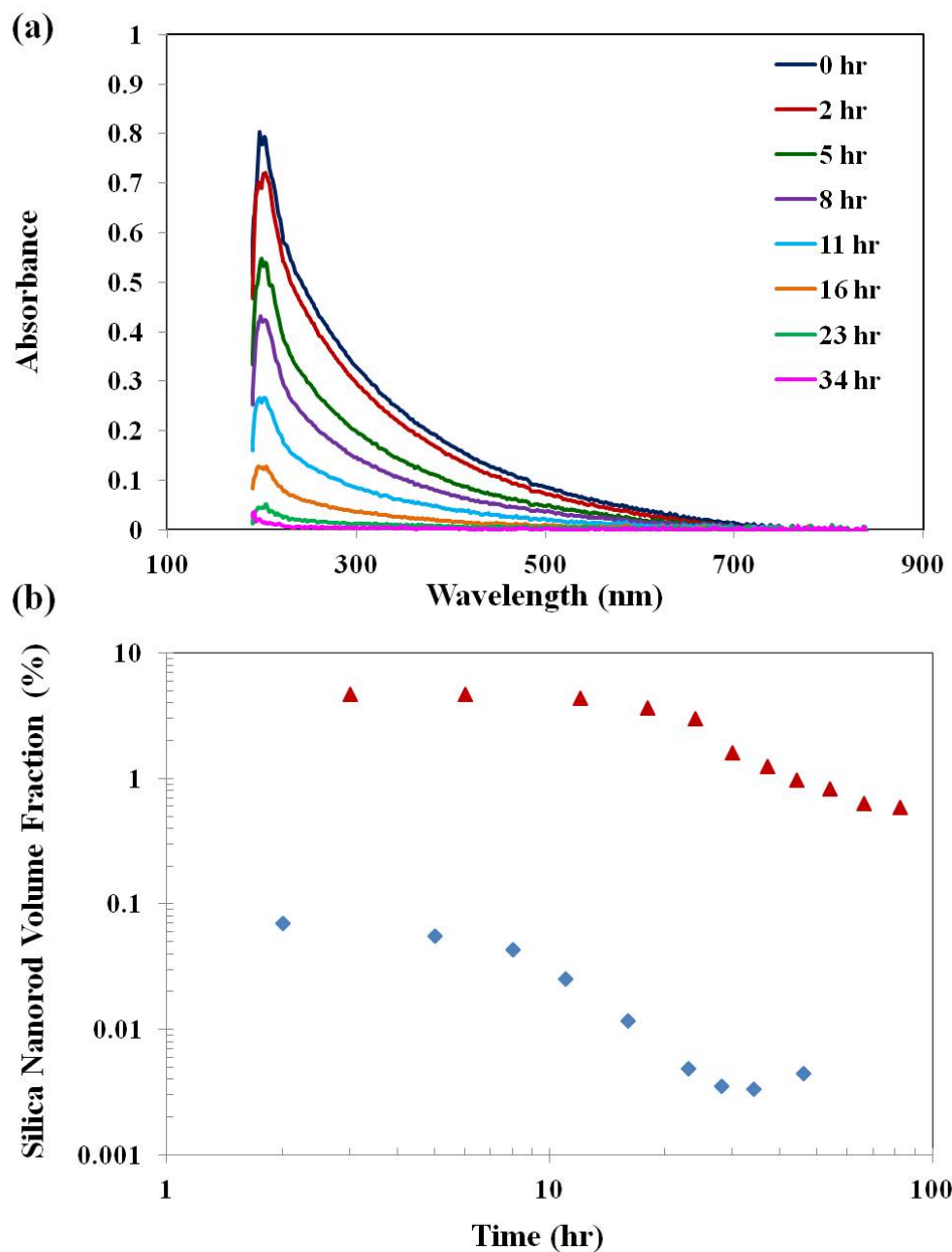


Figure 5.5 (a) UV-vis absorbance of silica nanorod-H₂O biphasic dispersion during sedimentation. (b) Silica nanorod concentration change during sedimentation for silica-80/20 DMSO/H₂O dispersion (red triangles) and silica-H₂O dispersion (blue diamonds).

5.3.2 Solvent Effect on Phase Transition

Figure 5.6 shows polarized light optical microscopy images of certain volume percentages of silica nanorods dispersed in different solvents by varying the H₂O percentage in binary mixture of DMSO and H₂O ratio from 0, 1/10, 2/10, and 10/10. The optical images show that as the silica nanorod volume fraction increases, the birefringence domain percentage increases; this is associated with the growth of liquid crystalline phase. The solvent effect significantly influenced the isotropic to biphasic transition ϕ_I , with increasing percentage of H₂O, solvent quality decreases, which results in a decrease in ϕ_I . It is noted that ϕ_I values at each H₂O percentage are much lower than the Onsager theory prediction.

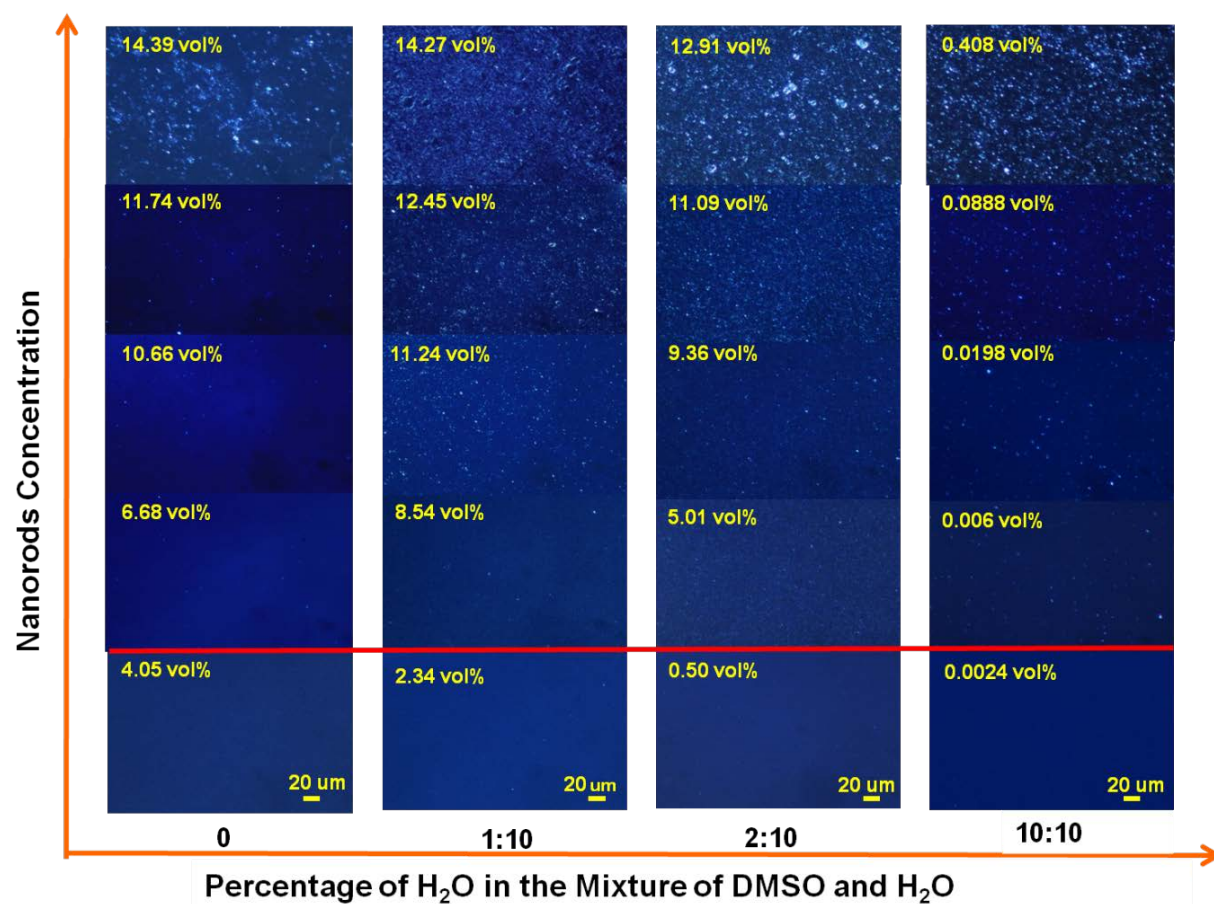


Figure 5.6 Polarized light optical microscopy images of silica nanorods dispersed in different ratio of DMSO/H₂O binary solvents

5.4 Smectic Liquid crystalline Phase Formation and Morphology

Kuijk et al⁵⁵ reported smectic liquid crystalline phase formation of silica nanorods based on alignment observed in confocal microscopy images, but did not include cross polarized optical microscopy more commonly used for liquid crystalline systems. Figure 5.7 shows high magnification cross-polarized optical microscopy images on biphasic dispersions of 15.9 vol. % silica nanorods in 90/10 DMSO/H₂O. The images are reminiscent of spherical focal conic defects (FCD),^{134, 135} (also called spherulites, onions, and multilamellar vesicles) which have been reported in smectic liquid crystals. These structures are spherical multilamellar structures with nanorod alignment perpendicular to each layer. It has been shown that the self-assembly texture of liquid crystal can be manipulated by designing and controlling the shape of the molecular used.¹³⁶ There have been several reports on spherical liquid crystalline self-assembly formed by tapered and conic shape dendrimers.^{137, 138} Therefore, the self-assembly of silica nanorods to spherical multilamellar texture may relate to the taper shape of silica nanorods. It is interesting to note that the focal conic defects observed in this system are not perfectly spherical shape, which are similar as the FCD with kinks resulting from a topological interaction at the points of junction.^{139, 140}

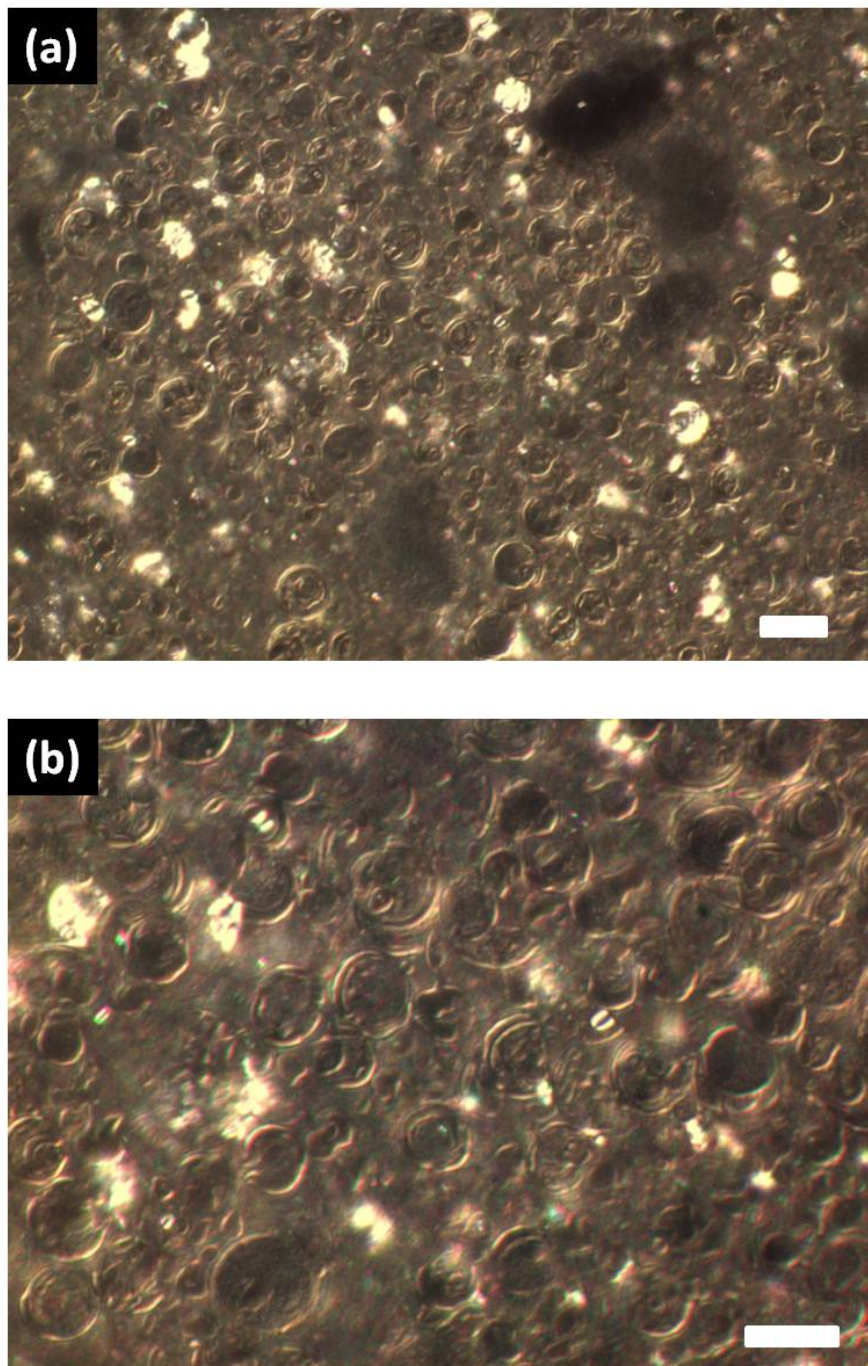


Figure 5.7 Optical images of 15.9 vol. % silica nanorods dispersed in 40% DMSO 60% H_2O . Images was taken under cross-polarized light on a Nikon Eclipse 80i with LU Plan Fluor oil 60x/0.45 objective with (a) 1 \times and (b) 2 \times magnification in front of the camera. The scale bars are 20 μm .

5.5 Phase Diagram

The phase diagram for silica nanorods dispersed in binary mixtures of DMSO and H₂O was established using cross-polarized light optical microscopy and rheology for silica nanorods in pure DMSO and 90/10 DMSO/H₂O. Since the optical microscopy and rheology results were consistent for those solvents, the phase transitions in other solvents were estimated by only optical microscopy. This phase diagram (Figure 5.8) is similar to those developed for rod-like polymers,^{141,57} and single-walled carbon nanotube/superacid dispersions.³¹ It shows that changing the solvent composition (the relative [DMSO]:[H₂O]) affects the solvent quality. As for nanotube/superacid dispersions, the solvent has a profound influence on the isotropic-biphasic transition ϕ_I , but little influence on the biphasic-liquid crystalline transition ϕ_{LC} . Higher water concentration decreased the solvent quality resulting in markedly lower values of ϕ_I . For all DMSO concentrations, the biphasic region was much wider than the hard rod model prediction. Our experimental measurement of the phase transition ratios ϕ_{LC}/ϕ_I for 100% to 40% ranged from 7.9-3840 at room temperature, which are all significantly larger than the Onsager theory prediction ($\phi_{LC}/\phi_I = 1.34$) and even larger than predictions for nematics with length polydispersity.^{66, 142, 143} Since there have been fewer studies on smectic systems it is difficult to compare these results to other works. However, similar observations were made for nematic CdSe nanorod-anhydrous cyclohexane dispersions,²³ and both experimental and theoretical studies on SWNTs-superacid dispersions showed a broad biphasic region resulted from a combination of polydispersity and attractive interactions.^{144, 145} We therefore attribute the broad biphasic region to a combination of nanorod polydispersity, the not completely cylindrical shape, and poor solvent quality, but additional studies would be needed to determine the relative contributions of each of these characteristics.

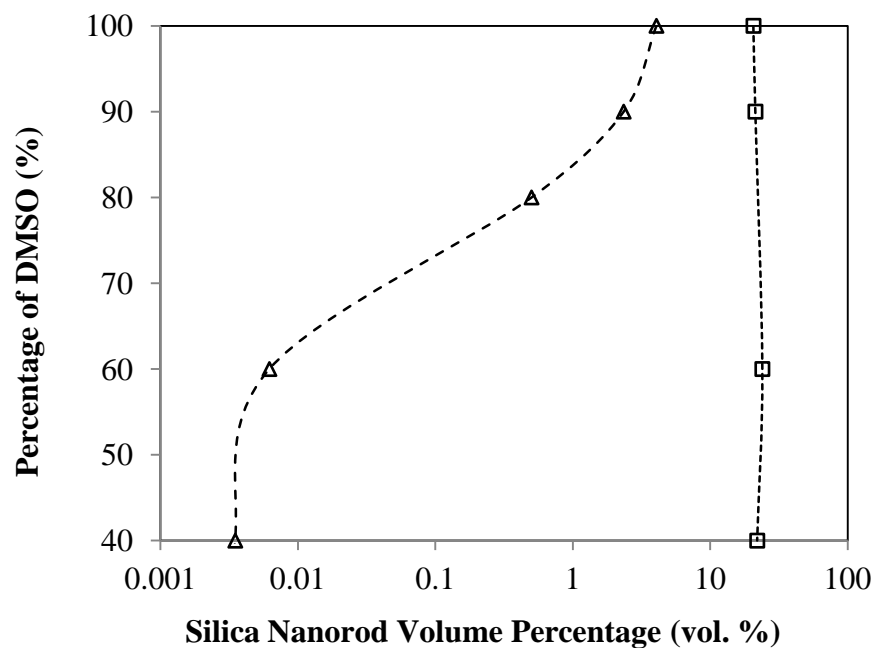


Figure 5.8. Phase diagram of silica nanorods dispersed in DMSO/H₂O, where more DMSO in solvent, better solvent quality resulting in a narrower biphasic region. Isotropic-biphasic transition ϕ_I (triangles); biphasic-LC transition ϕ_{LC} (squares).

When the DMSO concentration in the solvent was less than 40%, increasing the silica concentration did not result in liquid crystalline phase formation. In these poor solvents, liquid crystalline domains initially appeared at low concentration. However, as the concentration was further increased a crystal solvate phase (CS) formed and there appeared to be isotropic (I), liquid crystalline (LC), and crystal solvate (CS) coexistence (Figure 5.9). These CS phases are typically around 50 μm length and width, and the thickness are around 10–40 μm . CS phases have been found in both rigid-rod polymers in acids and SWNT in superacid after exposure to a water (moisture).^{146,147} For smectic A liquid crystals, nanorods can both move within each layer as in a liquid, and also penetrate from one layer to the next layer. In contrast, crystal solvents are aligned structures with a fixed lattice containing a fixed amount of solvent; unlike liquid crystals they cannot flow. The silica CS was distinct from the liquid crystalline domains in terms of its roughly tactoid shape, the more tightly packed structure and the fact that when a normal force was applied to samples in sealed microscope slides the CS moved as cohesive entities instead of spreading and then reassembling.

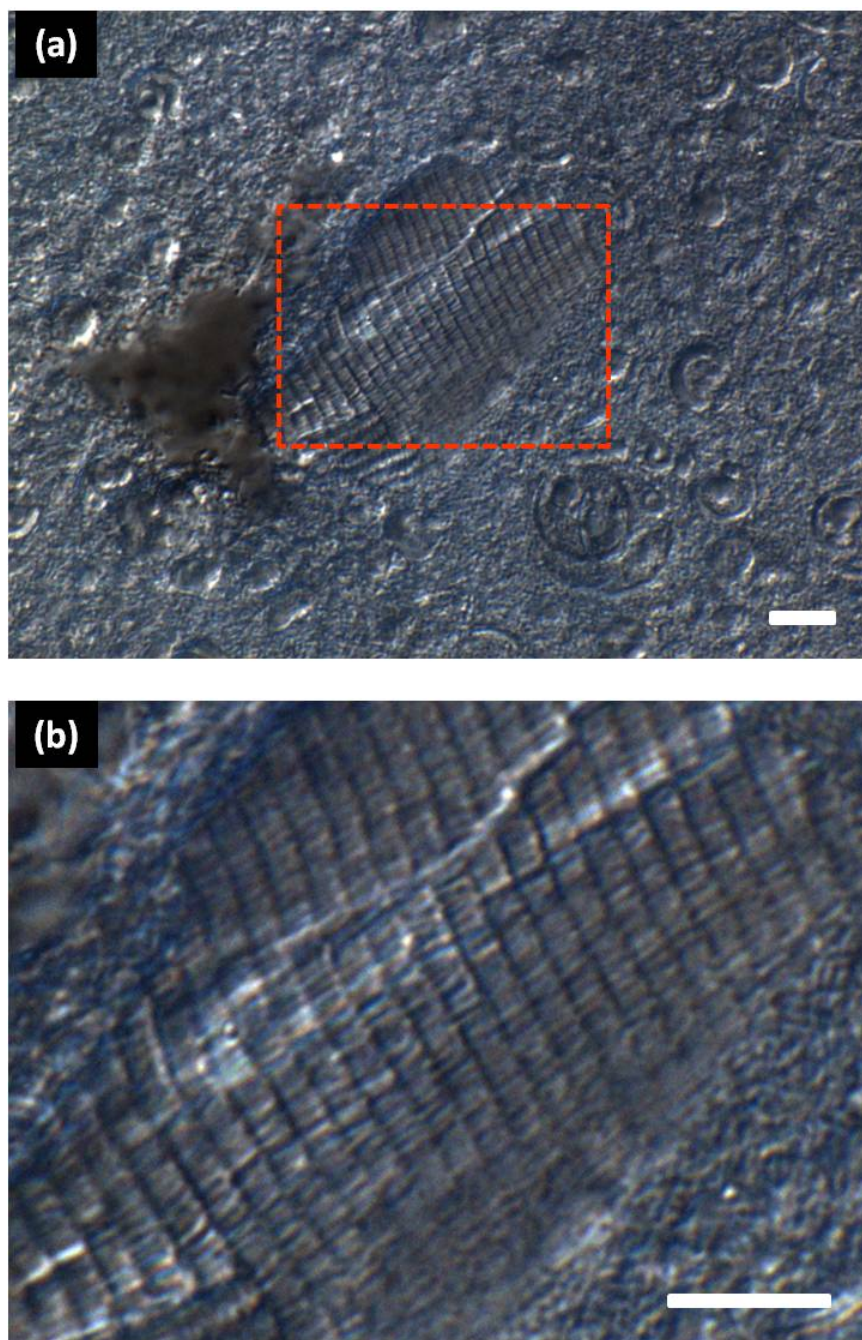


Figure 5.9 (a) Optical images of 31.3 vol. % silica nanorods dispersed in 20% DMSO 80% H₂O. Images were taken under cross-polarized light on a Nikon Eclipse 80i with LU Plan Fluor oil 60x/1.4 objective with 2× magnification in front of the camera. (b) Enlarged highlighted area. The scale bar is 10 μm.

5.6 Dispersion Processing Methodology Effect

Different processing methods to prepare silica nanorods dispersion have been explored. The silica-80/20 DMSO/H₂O biphasic dispersion after sedimentation over 100 hours will separate into three layers. The sedimentation process leaves the small rods in top layer, this further fractionate the size distribution in middle layer and bottom layer.

Similar to the goethite system investigated by Vroege et al.,²¹ the silica dispersions were only kinetically stable; over time the system sedimentated into different fractions with remarkably different microstructures. For example, sedimentating silica-80/20 DMSO/H₂O dispersion for over 100 hours resulted in three layers with distinct length distributions. As shown in Figure 5.10a, the sedimentation process left the shortest rods in a top layer, longer rods fractionated to the middle layer and the longest rods fractionated into the bottom layer. Samples taken from the top layer were isotropic and appeared completely black under cross polarized optical microscopy. Both the middle and bottom layers exhibited birefringence (Figure 5.10 b and c). The elongated structures appear similar to the oily streak textures which result from regular stacking of focal conic domains.^{148, 149} This “oil steak” structure formation has also been observed in thermotropic liquid crystal by decreasing the temperature,¹⁵⁰ and observed in lyotropic liquid crystal by applying shear.¹⁵¹ Oil streaks are thermodynamically favorable since they reduce the strain and surface energy between neighboring focal conic domains. This smectic structure is also observed in SEM images on dried coating obtained by drying the dispersion taking from middle and bottom layer at 80 °C and -30 mmHg for over 10 hours shown in Figure 5.10 (d,e).

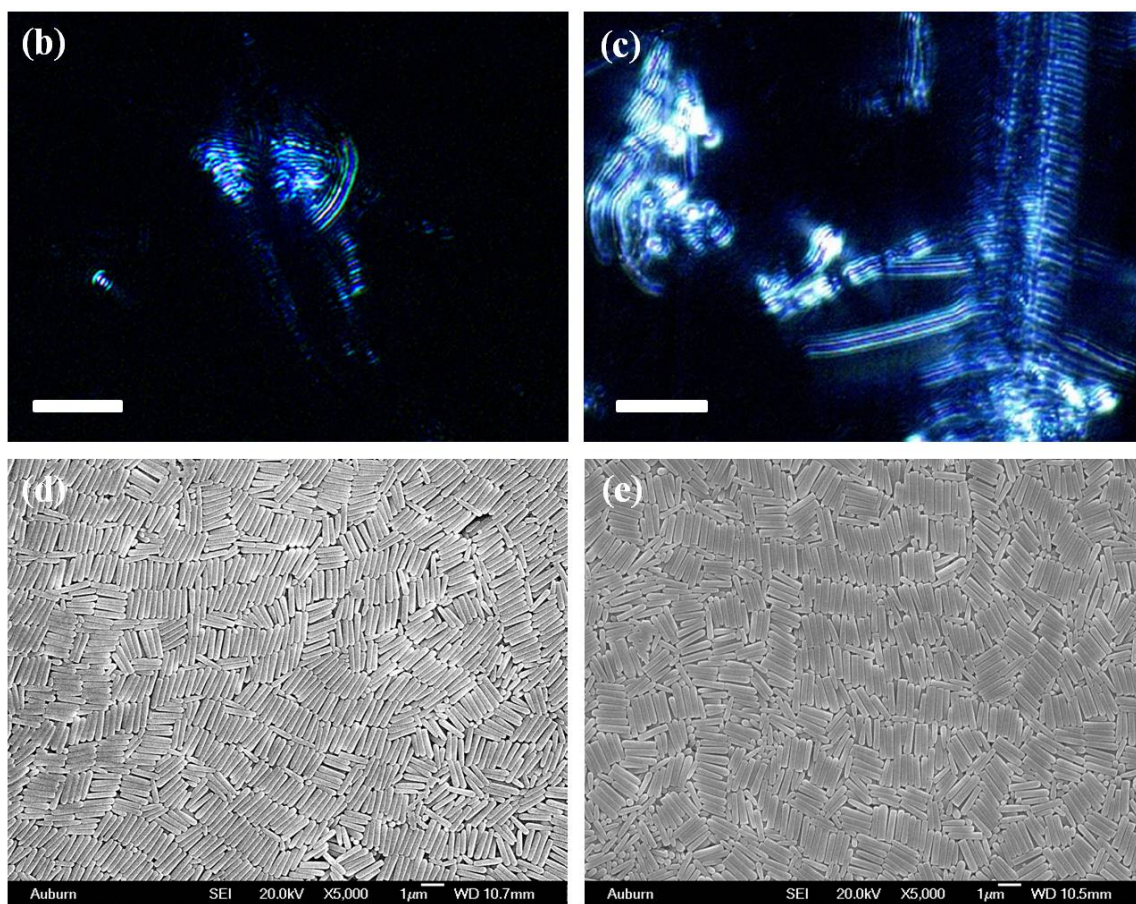
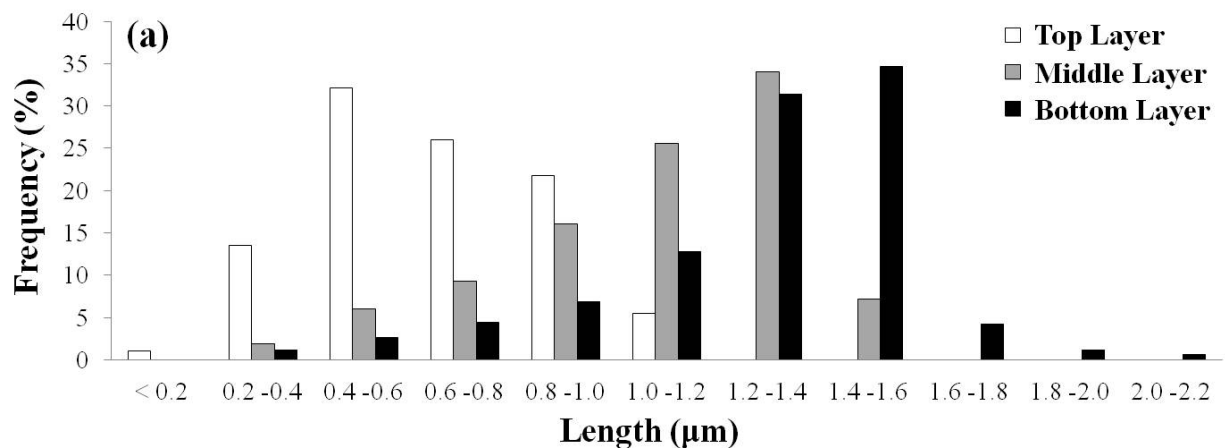


Figure 5.10 (a) Length distributions of silica nanorods dispersed in 80/20 DMSO/H₂O after sedimentation and taken from top, middle and bottom layers. Cross polarized light optical images of silica nanorods dispersed in 80/20 DMSO/H₂O after sedimentation and taken from (b) middle layer with 6.0 vol. % silica nanorods and (c) bottom layer with 34.1 vol. % silica nanorods of the dispersion. SEM images of dried coating made from (d) middle layer and (e) bottom layer. Scale bars are 10 μm for (b) (c).

5.7 Rheology

Rheology has proven a useful tool to augment microscopy investigations of liquid crystalline behavior of both rod-like polymers^{71, 85, 152, 153} and nanocylinders.^{30, 31, 34, 35, 147, 154, 155} However, the majority of the studies have focused on nematics. For lyotropic nematic liquid crystals, frequently observed rheological characteristics include that the viscosity versus concentration curve shows a maximum; start up shearing tests show the shear stress and first normal force difference oscillate over 100 shear units before reaching steady state; the Cox-Merz rule is not obeyed; and the viscosity versus shear rate curve often shows three distinct regions. There are not widely accepted rheological characteristics for smectic liquid crystals.^{71, 91, 92} Since nematics possess orientational order and smectics possess both positional order and orientational order some similarities can be expected. Theoretically, the shear response of monodomain smectic A phase should behave as an ordinary fluid when smectic layers are parallel to the shear direction, and as an elastic solid when under compression or dilation perpendicular to the layers.⁹² However, in practice, the appearance of both defects and dislocations in smectic liquid crystal systems result in very different rheological behavior than ordinary fluids or elastic solids. Similar to nematics, smectics typically show a critical yield stress beyond which the microstructure starts flowing and the rheological response is highly affected by the texture (i.e. defects and dislocations) of the system.^{95, 98, 99}

5.7.1 Viscosity versus Concentration Curve

Both Rheology and polarized light microscopy were used to characterize the phase transition of silica nanorods dispersed in DMSO/H₂O.

Figure 5.11 shows the evolution of microstructure and viscosity with increasing concentration of silica nanorods dispersed in 90% DMSO and 10% H₂O. As the concentration increases, viscosity initially increases, reaches to maximum and then decreases as the proportion of aligned domains increases. Once the system becomes fully liquid crystalline the viscosity starts to increase again. As expected, the maximum is less pronounced at higher shear rates and more pronounced at lower shear rates. The non-monotonic change of viscosity as a function of silica nanorods concentration is one of the characteristics of lyotropic liquid crystalline polymers (LCP). This upper minimum of viscosity versus volume fraction curve provides an estimate for the biphasic to liquid crystalline transition ϕ_{LC} .¹⁵⁶ For silica nanorods in 90/10 DMSO/H₂O $\phi_{LC} \approx 21.3$ vol. % based on both this rheological characteristic and the lowest concentration at which no isotropic domains were by optical microscopy. This concentration is much lower than the prediction of 89.8 vol. % by Onsager theory monodisperse rods interacting only hard through hard rod repulsion.⁶³ Furthermore, the dispersions in biphasic region showed a significant shear thinning behavior by comparing the viscosities at different shear rates 0.01, 0.1, 1, 10 s⁻¹. This shear thinning behavior is due to silica nanorods aligned parallel to the shearing direction after the shear rate reach to critical point.

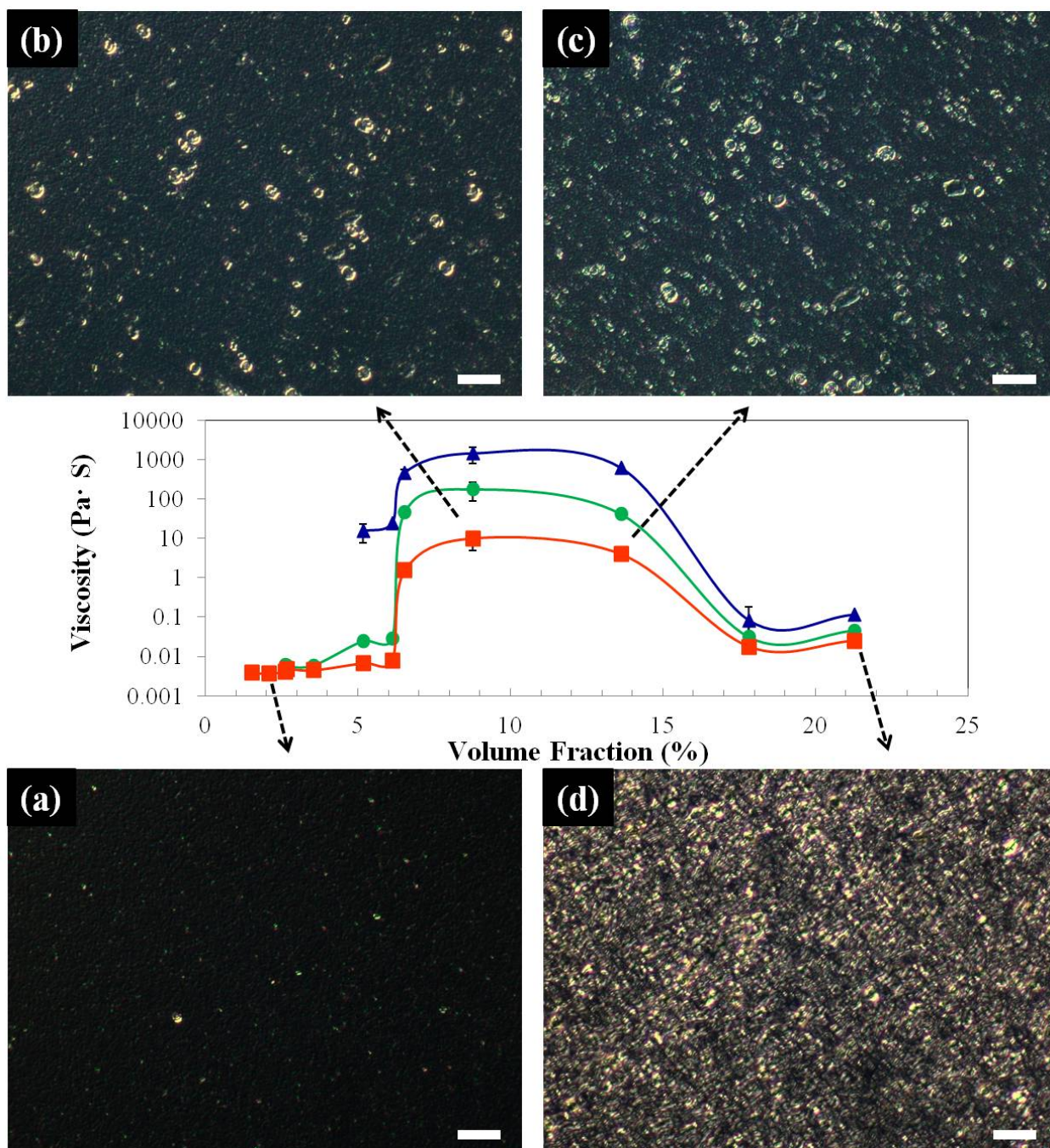


Figure 5.11 Relationship between viscosity and volume fraction of silica nanorods dispersed in 90/10 DMSO/H₂O with steady shear rate 0.1 s⁻¹ (blue triangles), 1 s⁻¹ (red circles), 10 s⁻¹ (orange squares). Accurate viscosities at shear rate lower than 0.1 s⁻¹ for low concentration of silica nanorods dispersion (below 5.2 vol. %) were not obtained due to insufficient torque. Images were taken under cross polarized light on a Nikon Eclipse 80i with 20× DIC 0.45NA objective and 2× additional magnifications in front of the camera. The increasing silica concentrations are (a) 2.7 vol. %, (b) 8.8 vol. %, (c) 13.6 vol. %, (d) 21.3 vol. %. The scale bars are 20 μm.

5.7.2 Transient of Start-up Flow

The dispersions also showed the long oscillatory transients typical of liquid crystalline dispersions. For all dispersions with silica nanorod volume fractions higher than 1.5 vol. %, the response to start-up of shear showed an overshoot followed by uniform oscillatory transients which persisted for over 1000 shear units. For example, Figure 5.12 shows the start-up of flow for 17.8 vol. % silica nanorods dispersed in 90/10 DMSO/H₂O at constant shear rates of 1 and 5 s⁻¹. This behavior is quite similar with that of liquid crystalline polymers,^{80, 81, 82} SWNT-superacid liquid crystals¹⁴⁴ and silver nanowire liquid crystals³⁵. This behavior is very different from that of isotropic dispersion,¹⁰⁵ where oscillatory transients last a few shear units at most. The silica dispersion data also exhibited the scaling behavior previously reported for liquid crystalline polymers.^{79, 81, 82, 83} Plotting the transient shear stress versus the shear unit (time multiplied by shear rate), results in curves with same period and intensity as shown in Figure 6b. This scaling behavior implies that the period of the oscillatory transient is inversely proportional to the shear rate. The long oscillatory transients together with the scaling behavior suggests that biphasic dispersions of silica nanorod are tumbling rather than shear-aligning in the low shear rate range.⁷¹ This is one of the features associated with lyotropic liquid crystals, and also shows the dispersion is sufficiently kinetically stable under gravity for rheological characterizations and fluid phase processing.

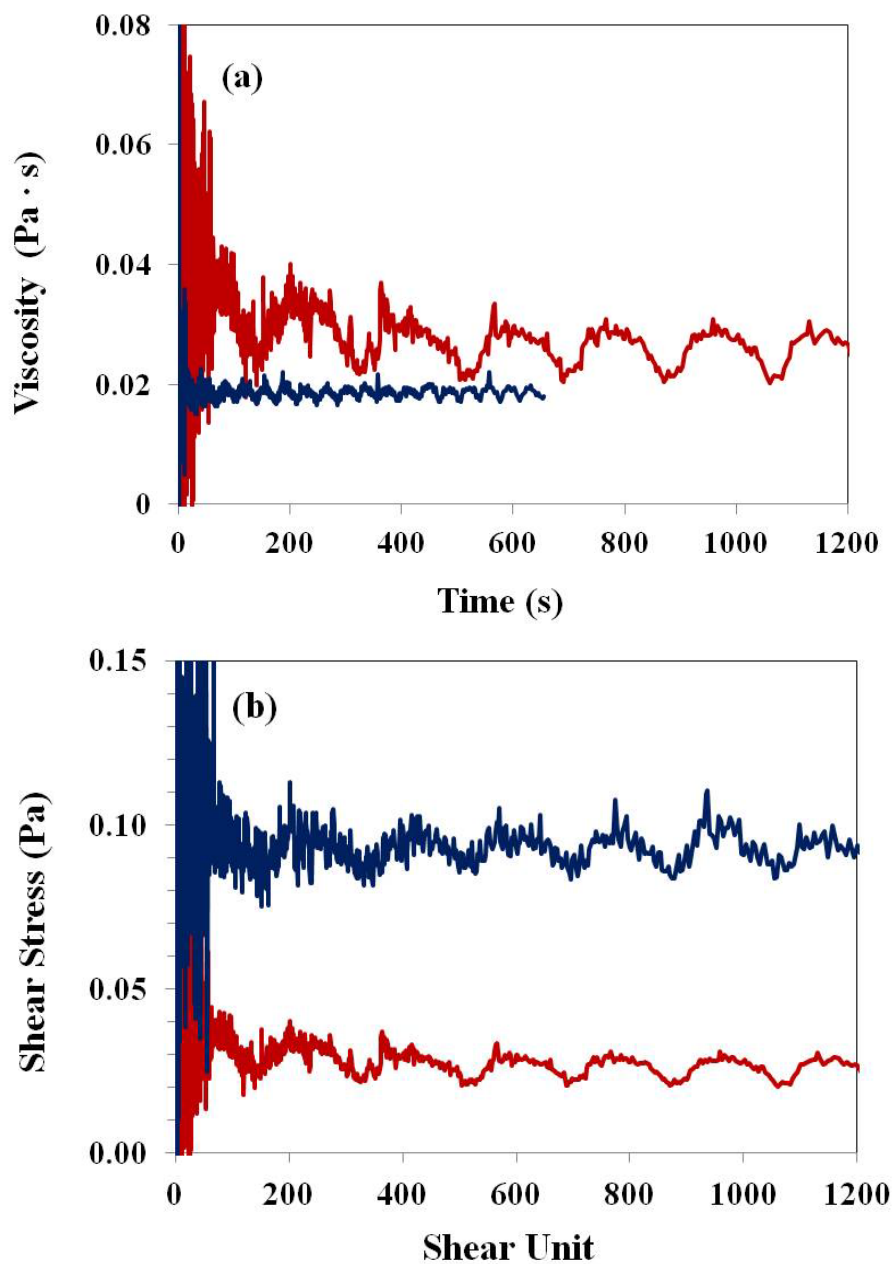


Figure 5.12 Start-up of flow of 17.8 vol. % silica nanorods dispersed in 90/10 DMSO/H₂O at constant shear rates of 1 s⁻¹ (black curve) and 5 s⁻¹ (grey curve). (a) Viscosity versus time curve and (b) shear stress versus shear unit curve.

5.7.3 Steady Shear Rheology

Steady shear tests were performed for both silica-90/10 DMSO/H₂O and silica-pure DMSO dispersions at different concentrations. A preshear with 1 s^{-1} for about 1000 s were applied to each experiment to ensure a well defined defect density. The steady shear viscosity versus shear rate curves of dispersions at different concentrations are shown in Figure 5.13 (silica-90/10 DMSO/H₂O) and Figure 5.14 (silica-pure DMSO). These dispersions with different solvents showed similar trends on the viscosity versus shear rate curve at different phase regions. For example, silica-90/10 DMSO/H₂O dispersions at the isotropic region with silica nanorod concentration lower than 2.7 vol% behaved as the Newtonian fluid at the measured shear rate range (Figure 5.13 a). When silica concentration increased to 2.7 vol. %, the dispersions began to show a shear thinning behavior. Furthermore, the viscosity kept increasing monotonically with silica concentration from 2.7 to 8.8 vol. %, where the viscosity showed a maximum in the biphasic regime (Figure 5.13 b). Further increasing the silica concentration to 13.6 vol. %, the viscosity started to decrease due to the formation of more ordered state (Figure 5.13 c). When the dispersion transitioned into an entirely liquid crystalline phase, the viscosity reached the minimum viscosity. This nonmonotonic relationship of viscosity as a function of concentration is a typical rheological signature of lyotropic LCPs.

It is interesting to note that the response of steady shear of dispersion at biphasic region and entirely liquid crystalline region are dramatically different. The steady shear rheology in biphasic region is still a debating area. The steady shear behavior of silica nanorod dispersion in entirely liquid crystalline region and near the biphasic to entirely liquid crystalline transition point showed similar response as the 8CB thermotropic smectic liquid crystal near its transition temperature.¹⁵⁷ As shown in Figure 5.15, the steady shear response of both silica-90/10 DMSO/H₂O and

silica-pure DMSO dispersions at silica concentration of 21.3 and 30.8 vol. % respectively divided into three regimes:¹⁵⁷ Regime 0 fitted by the Herschel-Bukely (HB) model; Regime I fitted by the power law behavior; Regime II corresponds to the Newtonian behavior. For the Regime 0, the dispersion behaved like a pseudo viscoplastic fluid fitted the HB model:

$$\sigma = \sigma_y + A\dot{\gamma}^n$$

where σ is the shear stress, σ_y is the yield stress, $\dot{\gamma}$ is the shear rate, A and n are adjustable parameters.¹⁵⁸ For Regime I, the dispersion can be fitted to a power law behavior:

$$\sigma = C\dot{\gamma}^{1/m}$$

where C is a prefactor, m is the shear rate index. When $m = 1$, the fluid behaves like a Newtonian fluid, when $m > 1$, the fluid behaves like a shear thinning fluid, and when $m < 1$, the fluid behaves like a shear thickening fluid. The model parameters at different regimes are summarized in Table 5-1. It showed that in Regime 0, the yield stress of silica dispersed in pure DMSO is lower than that of silica dispersed in 90/10 DMSO/H₂O. According to Horn and Kleman, the yield stress was related to the focal conic domain size:

$$\sigma_y \approx \frac{K}{L^2}$$

where K a constant with a typical value $K = 5.2 \times 10^{-12} \text{ N}$. Based on this equation, for 21.3 vol. % SiO₂ – 90/10 DMSO/H₂O dispersion, the focal conic domain size is $\sim 35 \text{ }\mu\text{m}$, while for 30.8 vol. % SiO₂ – pure DMSO dispersion, the focal conic domain size is $\sim 20 \text{ }\mu\text{m}$. In Regime I shear thinning region, the $m \approx 1.64$ for both dispersions, which is very close to both the experimental results of $1.67^{98, 99}$, 1.7^{157} , 1.85^{93} and theoretical model prediction of $5/3^{99}$ for smectic phase with focal conic defect. These shear thinning behaviors followed with a power law with similar shear rate index values are governed by the screw dislocation in focal conic domains.⁹⁹ In Regime II, both dispersions behaved close to a Newtonian fluid, with the shear rate

index equal to 1.11 and 1.24 respectively. This behavior suggested that there is a critical shear rate beyond which the defects became unstable and the lamellar phase began to orientate perpendicular to shearing direction with the molecular aligned parallel to the shearing direction.^{159, 160}

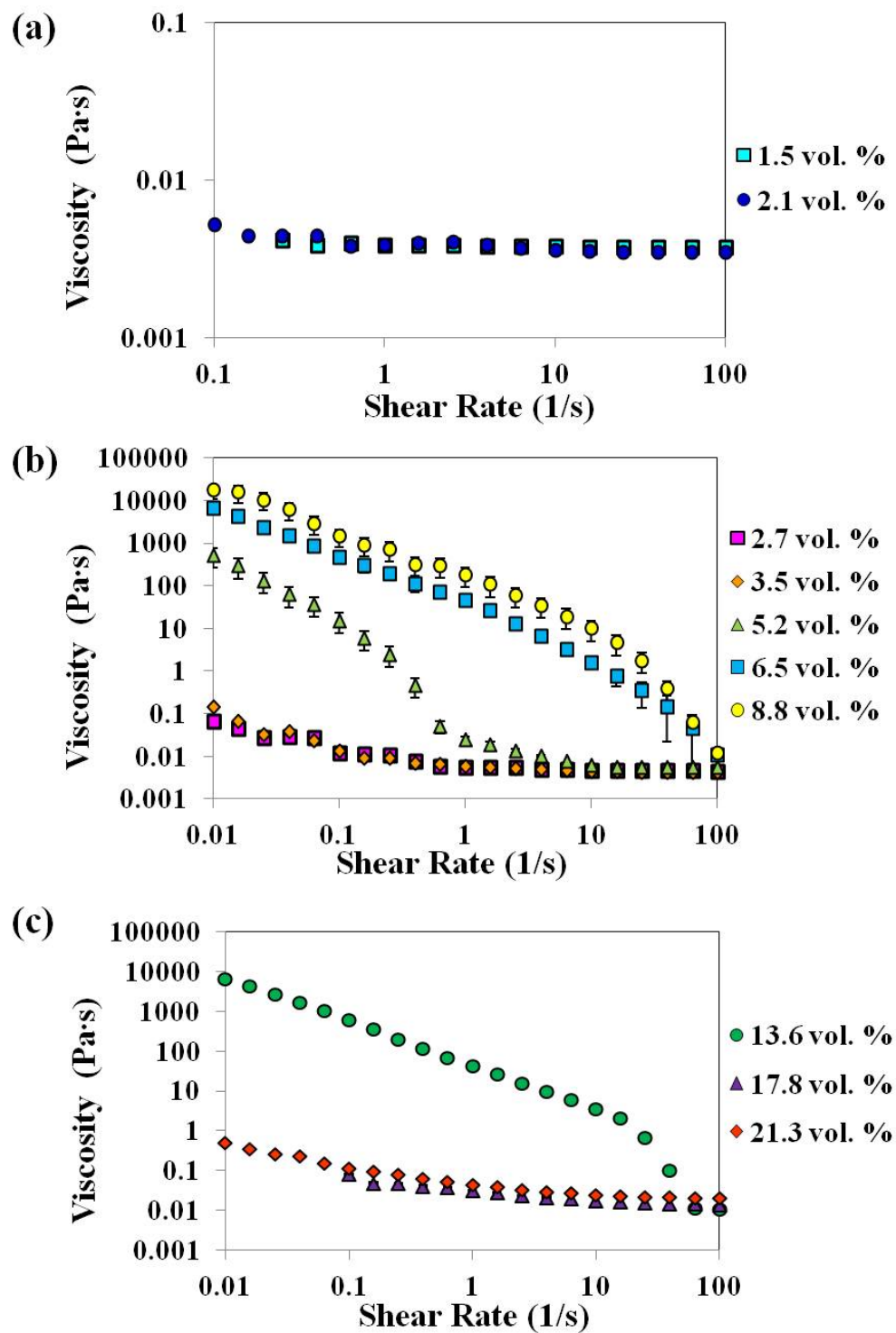


Figure 5.13 The steady shear viscosity of SiO₂-90/10 DMSO/H₂O dispersions at (a) isotropic region; (b) Increasing region of viscosity versus concentration curve; (c) Decreasing region of viscosity versus concentration curve.

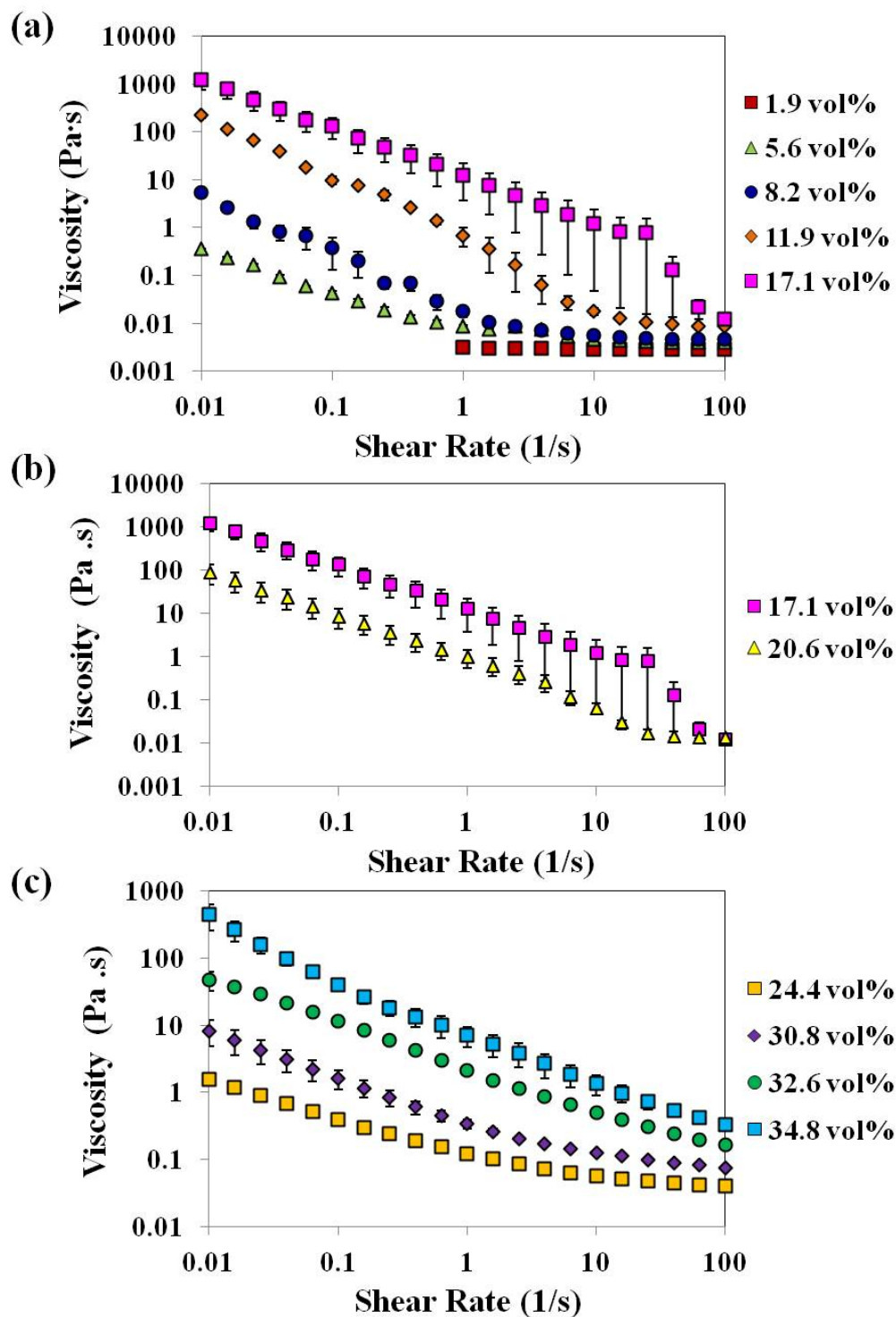


Figure 5.14 The steady shear viscosity of SiO₂-pure DMSO dispersions at (a) Increasing region of viscosity versus concentration curve; (b) Decreasing region of viscosity versus concentration curve; (c) Entirely liquid crystalline region.

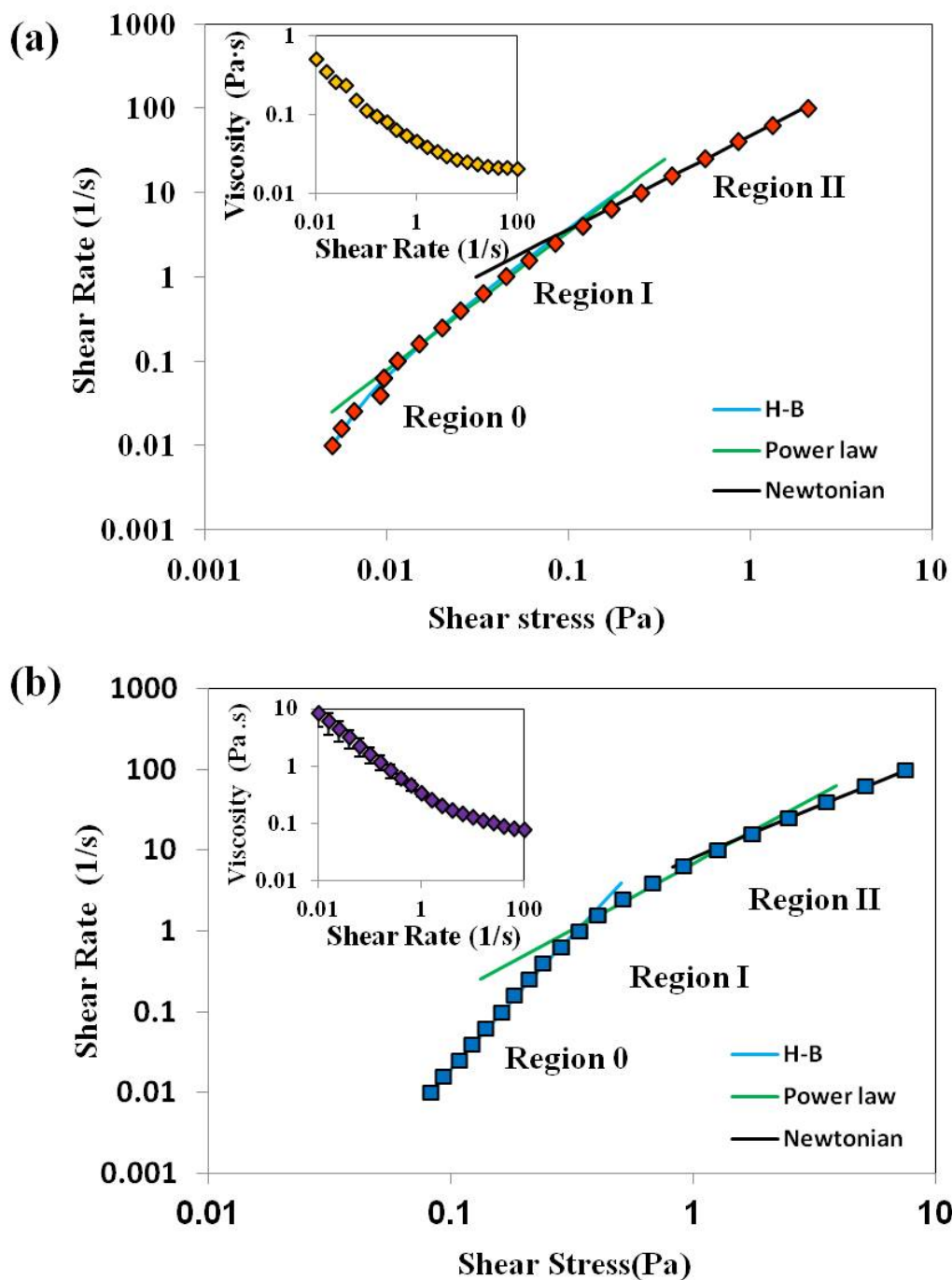


Figure 5.15 Steady state shear rate as a function of the shear stress just above the biphasic to entirely liquid crystalline phase transition of (a) 21.3 vol. % SiO_2 -90/10 DMSO/ H_2O ; (b) SiO_2 -pure DMSO 30.8 vol. %. Insets are viscosity versus shear rate curves.

Table 5-1 Yield stress, prefactor and shear rate index of steady shear response of 21.3 vol. % SiO₂-90/10 DMSO/H₂O and SiO₂-pure DMSO 30.8 vol. % at different regimes.

Dispersion	Regime 0			
	σ_y / Pa	A	n	R ²
21.3 vol. %SiO ₂ -90/10 DMSO/H ₂ O	0.003	0.041	0.65	0.985
30.8 vol. SiO ₂ -pure DMSO	0.01	0.32	0.32	0.999

Dispersion	Regime I		
	C	m	R ²
21.3 vol. %SiO ₂ -90/10 DMSO/H ₂ O	0.047	1.64	0.996
30.8 vol. SiO ₂ -pure DMSO	0.31	1.64	0.992

Dispersion	Regime II		
	C	m	R ²
21.3 vol. %SiO ₂ -90/10 DMSO/H ₂ O	0.031	1.11	0.999
30.8 vol. SiO ₂ -pure DMSO	0.186	1.24	0.999

5.7.4 Oscillatory Shear Rheology

The oscillatory measurements were performed on both silica-90/10 DMSO/H₂O and silica-pure DMSO dispersions with high concentrations silica nanorods. The strain amplitude dependence of both the storage modulus G' and loss modulus G'' of entirely liquid crystalline dispersions at different nanorod concentrations at a frequency ω of 10 rad/s is shown in Figure 5.16. At low strain amplitudes, the both modulus G' and G'' are independent of strain amplitude, but the amplitude dependence is observed at quite small values of strain amplitude (less than 1% strain). This reveals that the smectic liquid crystalline silica nanorod dispersions is “weak solid”⁹³ with very narrow linear viscoelastic region. This feature was also found in other smectic systems formed by both polymers (HTH-10 and PMADe) and small molecules (8CB).⁹³

Ordinary fluids follow the empirical Cox-Merz rule that the steady viscosity versus shear rate curve and dynamic viscosity versus frequency curve overlap very well. However, this rule is not obeyed for lyotropic liquid crystals.^{57, 71} This feature was also observed for both silica-90/10 DMSO/H₂O and silica-pure DMSO dispersions at nanorod concentrations from 5.2 vol. % to 13.6 vol. % for silica-90/10 DMSO/H₂O, and nanorod concentrations from 32.6 vol. % to 34.8 vol. % for silica-pure DMSO as shown in Figure 5.17.

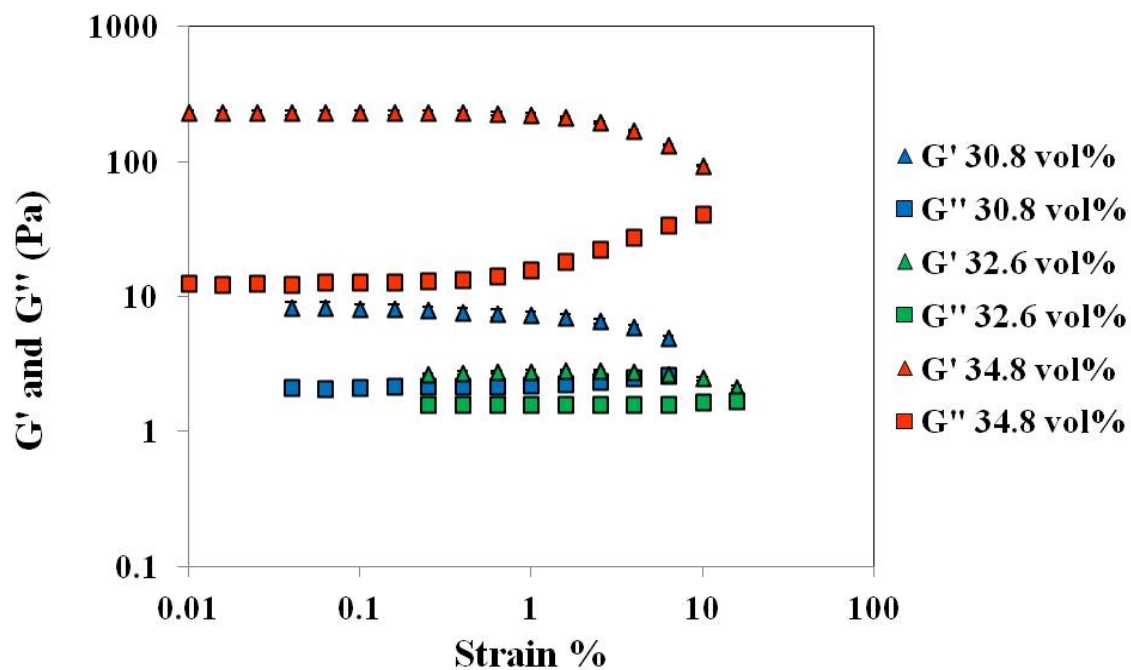


Figure 5.16 Strain amplitude sweep test of silica nanorod-DMSO entirely liquid crystalline dispersions at different nanorod concentrations at a frequency of $\omega = 10$ rad/s.

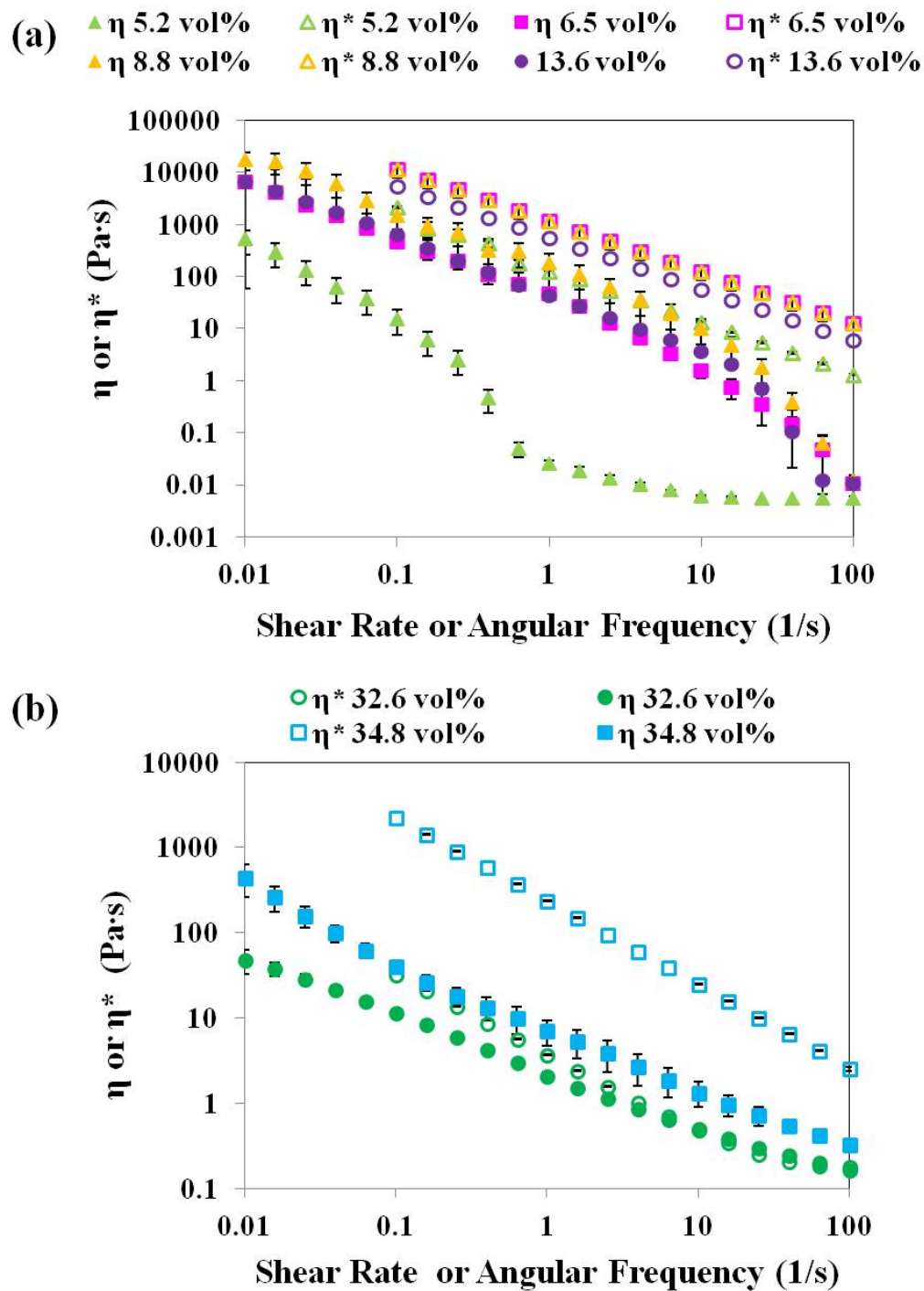


Figure 5.17 Viscosity/complex viscosity versus shear rate/angular frequency curve of (a) SiO₂-90/10 DMSO/H₂O in biphasic region and (b) SiO₂-pure DMSO in entirely liquid crystalline region.

5.8 Shear Induced Morphology Changes

Processing of liquid crystalline dispersions to form coatings, films, or fibers typically involves the application of shear; therefore, it is important to understand the shear response of the systems. Entirely liquid crystalline dispersions of 29.6 vol. % silica nanorods in pure DMSO showed lamellar structures with fewer focal conic defects (Figure 5.18 a). However, as shown by the inset there were still misaligned domains. In addition, this sample showed that centrifugation process is not perfect and a few very large bullet shaped rods were present. Using a coverslip to manually shear the sample resulted in more uniform alignment (Figure 5.18 b); the lamellar structure was more packed after shear due to the elastic compression between each layer.

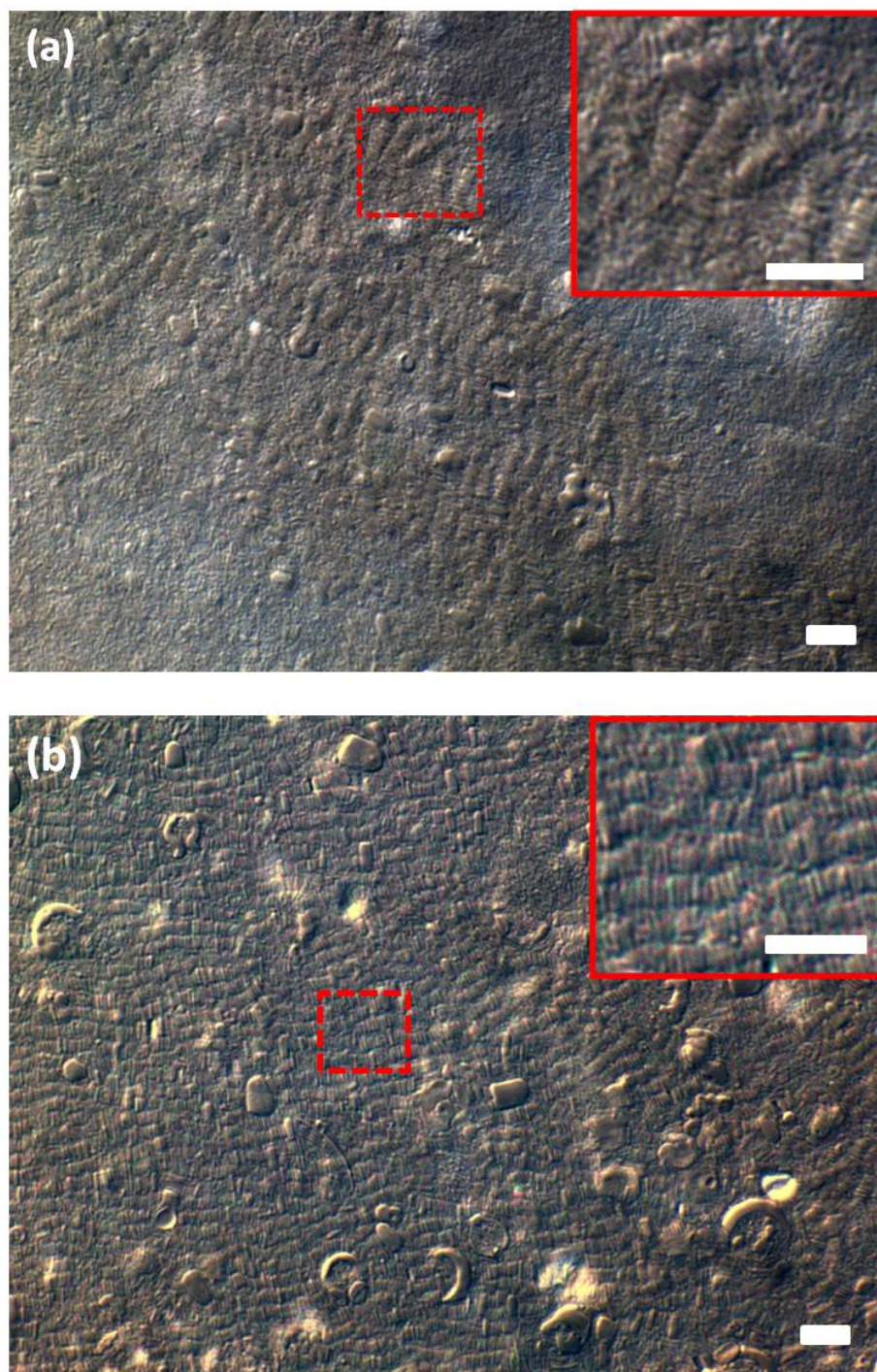


Figure 5.18. Optical images of 29.6 vol. % silica nanorods dispersed in pure DMSO (a) without and (b) with vertical shear. Images were taken under cross-polarized light on a Nikon Eclipse 80i with LU Plan Fluor oil 60 x/1.4 objectives with 2 \times magnification in front of the camera. The scale bar is 10 μ m. Detailed disorientation or monodomain lamellar phase are shown in the enlarged images.

5.8.1 Shear Induced Morphology Change Studied by Shear Cell

More detailed studies on shear induced morphology change were performed using a Rheo-optical set-up consisting of a Linkam shear cell on a Nikon i80 cross-polarized optical microscope. A liquid crystalline dispersion of 29.2 vol. % silica nanorods dispersed in 90% DMSO-10% H₂O is used in this experiment. Figure 5.19 shows the original nanorods before shear self-assemble to a lamellar structure. However, the structure is not homeotropic with curvature of the layers and disorientation of the rods within the layers. After slowly lowering the gap to 60 μm , the dispersion is allowed to rest for 1 hour before the shearing test. The optical image of the dispersion at the original state showed a lamellar structure roughly perpendicular to the shear cell shearing direction. Three different shear rates at 8.75, 12.5 and 37.5 s^{-1} were applied on this dispersion with 1 hour relaxation time in between. The dispersion microstructure change after cessation of shear were recorded by the optical microscopy with 50 x high WD objective and 2 x magnification in front of the camera. The result showed that there is a critical shear rate between 8.75 and 12.5 s^{-1} , which induce the rods generally aligning parallel to the shearing direction and layers perpendicular to the shearing direction. Increase the shear rate to 37.5 s^{-1} , more refined texture was observed after shear. Layer structure with high elastic energy resemble after hours. The higher shear rate, longer time is need for layer structure relaxation.

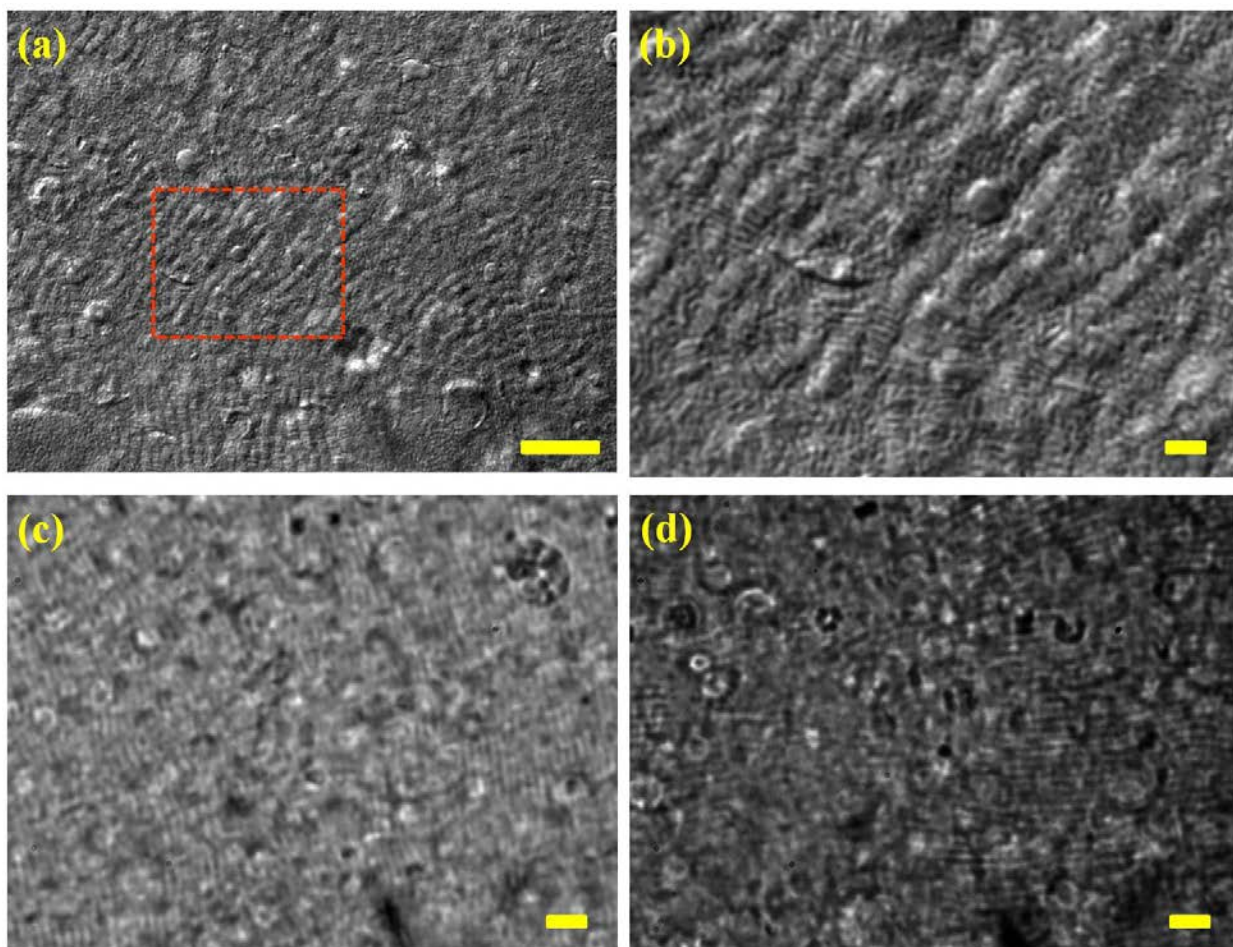


Figure 5.19 (a) Optical images of 29.2 vol. % silica nanorods dispersed in 90% DMSO 10% H₂O without shear. Images were taken under cross-polarized light on a Nikon Eclipse 80i with LU Plan Fluor oil 60 \times /0.45 objective with 2 \times in front of camera and (b) enlarged image. Same sample observed in shear cell using a long WD 50 \times objective with 2 \times in front of camera (c) before shearing test and (d) after shear at 37.5 s⁻¹ shear rate. The scale bar is 10 μ m in (a, c, d), and 2 μ m in (b).

5.8.2 Shear Induced Morphology Change Studied by SALS

Small Angle Light Scattering (SALS) is used to study the shear effect on a defective lamellar phase. Since liquid crystals must be both aligned and able to flow, Rheo-SALS was used to confirm that the onion structures observed by polarized optical microscope were deformable under shear. Figure 5.20 (a) showed SALS of low concentration biphasic dispersion of silica nanorods in 90% DMSO and 10% H₂O during a ramp up of shear rate from 0.1 to 100 s⁻¹. Both the SALS images (Figure 5.20 a) and the corresponding intensity curve (Figure 5.20 c) showed the intensity increases with shear rate. This scattering intensity increase with shear rate is consistent with shear effect study on lyotropic smectics A dispersion of a quaternary mixture of sodium dodecyl-sulphate (SDS), pentanol, water and dodecane by Diat and coworkers.^{161, 162, 163} This SALS intensity increase are corresponding to defect reducing by smaller the focal conic domains in the dispersion. Figure 5.20 (b) shows SALS images of higher concentration biphasic dispersion of silica nanorods in 90% DMSO and 10% H₂O during a ramp up of shear rate from 0.1 to 100s⁻¹. For higher silica nanorods concentration, the overall intensity of SALS at the entire shear rate range is higher than the intensity of lower silica nanorods 90% DMSO and 10% H₂O dispersion. However, it shows similar trend that the intensity increase with shear rate, which are associate with the focal conic domain size decrease. Beside, for both dispersions, the scattering showed little dependent on the angle at low shear rate, while the angle dependent of scattering appeared ~10-100 s⁻¹. This suggests that there is a critical shear rate associated with the focal conic defect deformation, which is at the magnification of 10 s⁻¹.

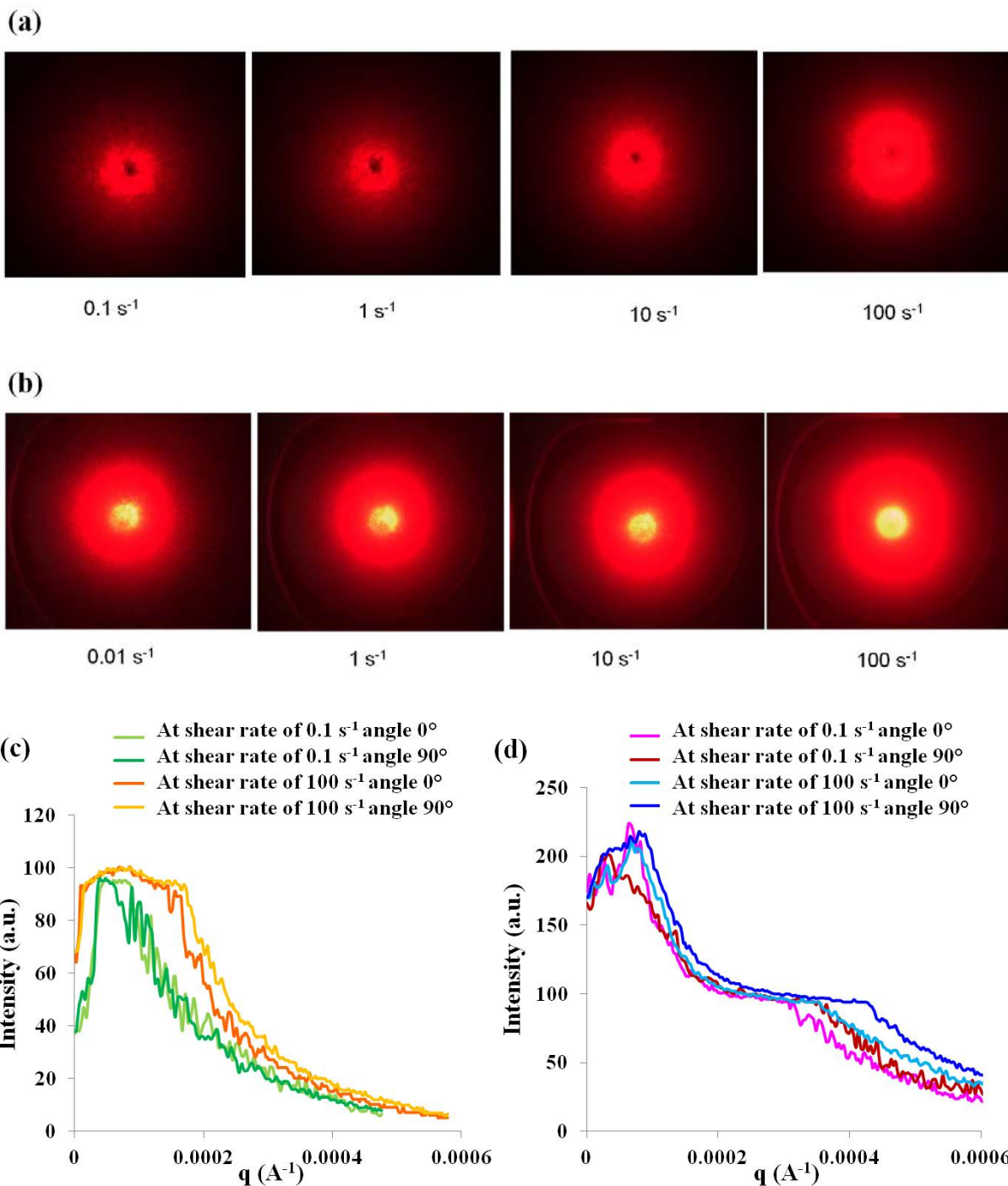


Figure 5.20 (a) SALS of 2.1 vol. % SiO₂-90/10 DMSO/H₂O and (b) 8.5 vol. % SiO₂-90/10 DMSO/H₂O during flow curve test at 0.1, 1, 10, and 100 s⁻¹; Corresponding scattering intensity at shear rate of 0.1 and 100 s⁻¹ and angle of 0° and 90° of (c) 2.1 vol. % SiO₂-90/10 DMSO/H₂O and (d) 8.5 vol. % SiO₂-90/10 DMSO/H₂O.

5.9 Film/Coating Fabrication

5.9.1 Drop Casting

Much of the interest in the phase behavior of nanorods in solvents relates to efforts to process the dispersions into films and coatings with controlled alignment. Drop casting method is an important small scale fabrication method for inkjet printing, washing and coating processes. Drop casting biphasic 6.7 vol. % silica in 90/10 DMSO/H₂O and removing the solvent at 80 °C under -30 mmHg vacuum resulted in “coffee ring” structures. The “coffee ring” structure formed mechanism after liquid drop evaporation has been explained by Deegan et al.^{164, 165} Contact line pinning resulted in radial flow of the rods toward the droplet edge and circumferential alignment along the edge of the dried drop. As a result, the center of the dried drop had a lower density of rods and isotropic microstructure. Figure 5.21 a shows that this coffee ring formation was even visible to the naked eye, while Figure 5.21 c and Figure 5.21 d show SEM images of the isotropic center and aligned edge. Cross polarized light optical microscopy image in Figure 5.21 b is consistent with the SEM, which shows the sample is birefringent at the edge and completely dark in the center. The recent study on polystyrene colloidal particle¹²⁵ showed that the aspect ratio affected the “coffee ring” structure formation. High aspect ratio ellipsoids with strong long-range interparticle attraction lead to a loosely packed structure rather than “coffee ring” structure. However, the diameter of nanorods in our system is significantly smaller than the polystyrene colloidal particles. Besides, the evaporation rate may also critical for the balance the strong long-range interparticle attraction of anisotropic particles. Coffee ring formation has been studied for other anisotropic nanomaterials including single-walled and multi-walled carbon nanotubes.^{122, 123}

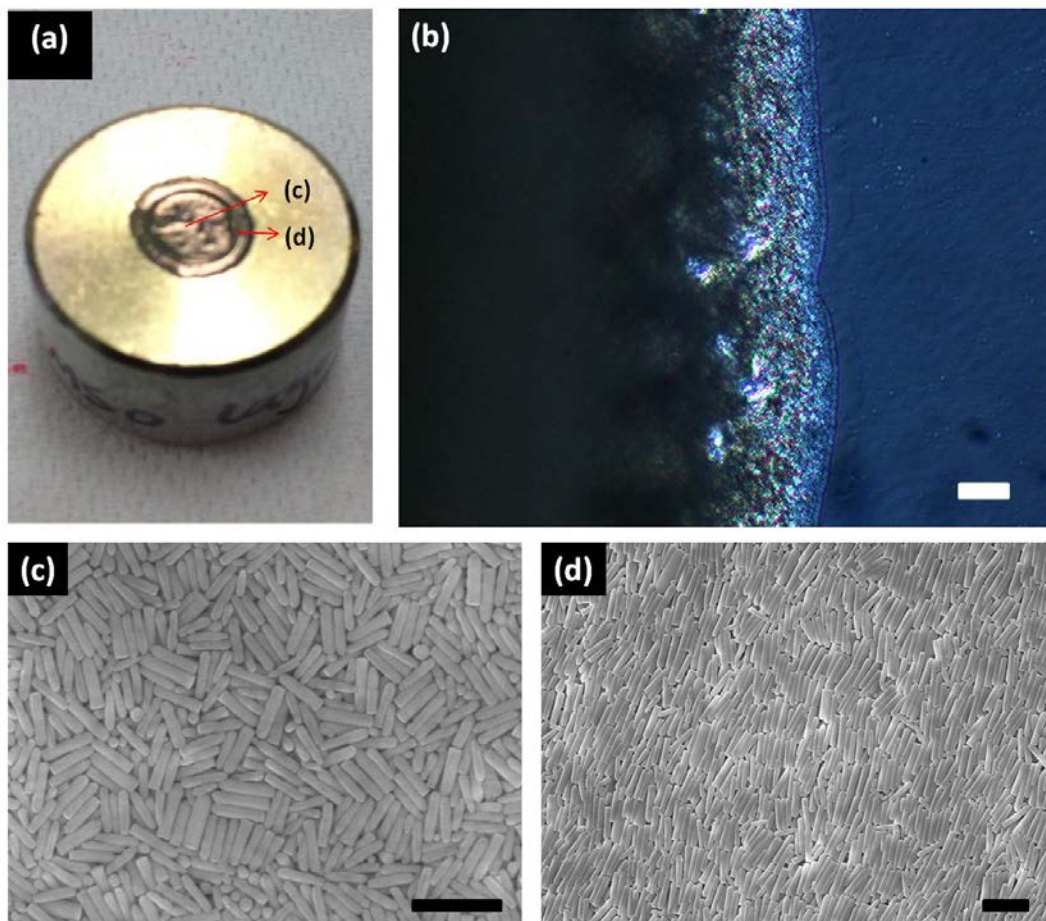


Figure 5.21 Images of drop casting coating obtained from silica-90/10 DMSO/H₂O biphasic dispersion at 6.7 vol. % without shear. (a) Coffee rings structure; (b) Cross polarized light optical image; (c) SEM image in the center; (d) SEM image close to the edge. Scale bar in (c, d) are 2 μm , in (b) is 20 μm .

5.9.2 Shear Alignment

Many coating processes involve shear which is known to align rods. Biphasic dispersions of 6.9 vol. % and 9.3 vol. % in 90/10 DMSO/H₂O were manually sheared at $\sim 100 \text{ s}^{-1}$ and then dried in a vacuum oven for over 10 hours at 80 °C under -30 mmHg vacuum. The SEM images (Figure 5.22) of the dried coatings showed silica nanorods generally aligned in the shearing direction. However, coatings made from 9.3 vol. % silica nanorods show greater alignment and closer packing structure than the coating made from 6.9 vol. % silica nanorods. For the coating made from 6.9 vol. % silica nanorod, $\sim 79 \%$ nanorods aligned within the 45° angle of deviation, and $\sim 25 \%$ nanorods aligned within 10° angle of deviation. However, for coating made from 9.3 vol. % silica nanorods, $\sim 99 \%$ nanorods aligned within 45° angle of deviation, and $\sim 50\%$ nanorods aligned within 10° angle of deviation. These results are consistent with other studies that higher alignment in more predominantly liquid crystalline dispersions can result in greater alignment in bulk materials.¹⁴⁷ In addition the higher viscosity of the 9.3 vol. % silica nanorods dispersion ($\sim 1000 \text{ Pa}\cdot\text{s}$ for 9.3 vol. % and $\sim 10 \text{ Pa}\cdot\text{s}$ for 6.9 vol. % at shear rate of 0.1 s^{-1}) may have retarded relaxation after the cessation of shear further contributing to the more aligned film.

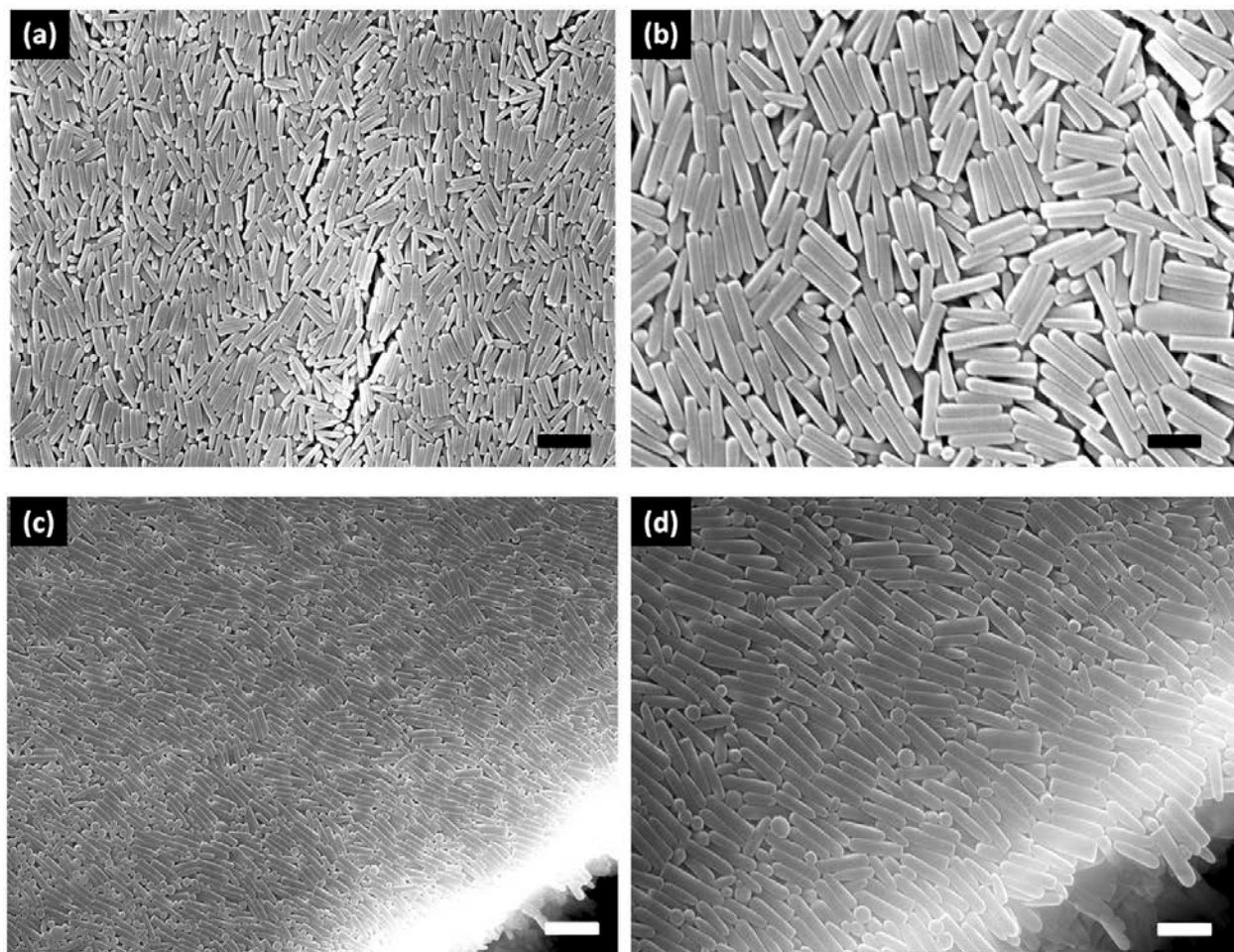


Figure 5.22 Scanning electron microscope images of shear alignment film obtained from shearing silica nanorods 90/10 DMSO/H₂O dispersion (a) with 6.9 vol. % nanorods and (b) enlarged image, and (c) with 9.3 vol. % nanorods and (d) enlarged image. The scale bar is 2 μm for (a) (c), and 1 μm for (b) (d).

5.10 Conclusion

The experimental phase diagram for dispersions of silica nanorods in DMSO/H₂O shows the phase behavior was highly affected by the DMSO percentage in the binary solvent. Below a critical DMSO concentration, the system is initially biphasic, but a completely liquid crystalline phase cannot be formed. Instead, the system forms crystal solvates. Dispersion rheology was consistent with the key rheological characterizations for rod-like polymer lyotropic liquid crystals include: the viscosity versus concentration curve shows a maximum; start up shearing tests shows the shear stress and oscillate over 100 shear units before reaching steady state; and the Cox-Merz rule is not obeyed. Different dispersion microstructures were observed, depending on whether or not after long time sedimentation and consequently different silica nanorod polydispersities. The microstructures of coatings produced from the dispersions were dependent on the initial microstructure and the applied shear.

Chapter 6 CONCLUSION

Lyotropic nanocylinder liquid crystals are a recent extension of the well-established field of liquid crystalline science. The majority of research to date has focused on nematic liquid crystals of nanorods/nanotubes with intermediate aspect ratios. This research highlighted that a broad range of nanocylinder dispersions can form liquid crystalline phases and that demixed nematic and smectic phases are possible. Dispersions containing silver nanowires with an average length of approximately 6 μm , and silver nanoparticle aggregates formed demixed nematic phases in ethylene glycol. This result was surprising due to the combination of long length, high density of Ag relative to that of the solvent, and the significant shape and size polydispersity. In contrast, dispersions of silica nanorods with an aspect ratio of 5, which is near the lower Onsager limit of 4.49 for non interacting rods, formed smectic liquid crystal phases in mixtures of DMSO and water. The isotropic-biphasic boundary was highly dependent on the relative concentrations of DMSO and water in the solvent, but the biphasic liquid crystalline boundary ϕ_{LC} was nearly constant when the DMSO concentration in the solvent was above 40%. Below a critical concentration of 40% DMSO, the system could form liquid crystal domains, but increasing concentration resulted in the formation of a crystal solvate phase and not a single phase liquid crystal.

The morphology and rheology of the systems investigated in this research was reminiscent of previous studies but contained some unique features. In the biphasic region, the silver system showed the spaghetti structure which was first reported for SWNT-superacid dispersions; this

structure is a significant contrast to the more globular domains typically formed by liquid crystalline polymers. Like both polymer and carbon nanotube liquid crystals, the nematic region was characterized by Schlieren structures. Under shear, the silver system could form shear band and worm textures. These textures have been reported in the liquid crystalline polymer literature, however, in the silver system they were retained for remarkably long time after shear cessation. This distinction is attributed to the nanowires' large size and high persistence length. In spite of polydispersity, the silica system formed smectic phases characterized by a large number of focal conic defects. The tapered shape of the shorter rods may have contributed to this texture. In fact, after fractionating the sample by sedimentation, the bottom layer which contained the longest, less tapered rods, formed oily streak textures. Rheologically, both systems showed the expected long maximum in the viscosity versus concentration curve. They also exhibited other characteristics of liquid crystalline polymer systems such as a yield stress and failure of the Cox-Merz rule. The similarities of the rheology of these systems to each other, and to other nanocylinder dispersions such as SWNT-superacids, show that what has long been thought of as characteristics of lyotropic polymer liquid crystals are more broadly applicable. The distinctions between these systems highlight the potential differences between smectics and nematics and systems with markedly different mesogen building blocks.

Drop casting studies showed that the silica nanorods formed coffee rings; this is consistent with expectations for drying drops of colloidal dispersions with contact line pinning. In contrast, the larger, more complex, silver nanowire system did not form coffee rings. This was attributed to the capillary force being insufficient to move and orient the high aspect ratio rods and the presence of the aggregates. Shearing the dispersions in an effort to produce aligned coatings, confirmed that dispersions with greater intrinsic alignment (due to more liquid crystalline ordering) resulted

in coatings with greater alignment. In addition, these studies showed that in the demixed nematic silver system, shearing resulted in the nanowires aligning at the top of the coating and the nanosphere aggregates packing together in the bottom layer of the coating. Shearing the smectic phases resulted in the rods aligning into layers with some defects existing between domains, particularly in the vicinity of unusually large diameter rods.

Inorganic nanocylinders are an intriguing and relatively new class of mesogens in the over one hundred year old field of liquid crystalline science. The results of this research highlight that liquid crystalline science provides a solid foundation for understanding the phase behavior, rheology, and processing of nanocylinder dispersions. Many of the characteristics that have historically been attributed to lyotropic liquid crystalline polymers are being established as being more broadly application to macromolecular lyotropic liquid crystals - including nanocylinder liquid crystals. However, the range of geometries, densities, and nanocylinder interactions can result in morphologies and behaviors that would not be anticipated based on the lyotropic liquid crystalline polymer literature. Nanocylinders promise to make exciting contributions to understanding the phase behavior and rheology of dispersions containing anisotropic entities. Furthermore, this evolving, fundamental understanding holds promise for the production of new aligned materials just as developing a fundamental understanding of rod-like polymer solutions resulted in revolutionary materials such as DuPont Kevlar.

REFERENCE

- (1) Iijima, S. Helical microtubules of graphitic carbon. *Nature* **1991**, *354*, 56-58.
- (2) Chaney, S. B.; Shanmukh, S.; Dluhy, R. A.; Zhao, Y. P. Aligned silver nanorod arrays produce high sensitivity surface-enhanced Raman spectroscopy substrates. *Applied Physics Letters* **2005**, *87*.
- (3) Yang, Y.; Xiong, L. M.; Shi, J. L.; Nogami, M. Aligned silver nanorod arrays for surface-enhanced Raman scattering. *Nanotechnology* **2006**, *17*, 2670-2674.
- (4) Hu, Z. A.; Wang, Y. X.; Xie, Y. L.; Yang, Y. Y.; Zhang, Z. Y.; Wu, H. Y. Ag nanowires and its application as electrode materials in electrochemical capacitor. *Journal of Applied Electrochemistry* **2010**, *40*, 341-344.
- (5) De, S.; Higgins, T. M.; Lyons, P. E.; Doherty, E. M.; Nirmalraj, P. N.; Blau, W. J.; Boland, J. J.; Coleman, J. N. Silver Nanowire Networks as Flexible, Transparent, Conducting Films: Extremely High DC to Optical Conductivity Ratios. *ACS Nano* **2009**, *3*, 1767-1774.
- (6) Chen, J. F.; Ding, H. M.; Wang, J. X.; Shao, L. Preparation and characterization of porous hollow silica nanoparticles for drug delivery application. *Biomaterials* **2004**, *25*, 723-727.
- (7) Chen, C. C.; Liu, Y. C.; Wu, C. H.; Yeh, C. C.; Su, M. T.; Wu, Y. C. Preparation of fluorescent silica nanotubes and their application in gene delivery. *Advanced Materials* **2005**, *17*, 404-407.
- (8) Buyukserin, F.; Martin, C. R. The use of Reactive Ion Etching for obtaining "free" silica nano test tubes. *Applied Surface Science* **2010**, *256*, 7700-7705.
- (9) Xi, J. Q.; Kim, J. K.; Schubert, E. F. Silica nanorod-array films with very low refractive indices. *Nano Letters* **2005**, *5*, 1385-1387.
- (10) Yu, Y. Y.; Chen, C. Y.; Chen, W. C. Synthesis and characterization of organic - inorganic hybrid thin films from poly(acrylic) and monodispersed colloidal silica. *Polymer* **2003**, *44*, 593-601.
- (11) Malzbender, J.; den Toonder, J. M. J.; Balkenende, A. R.; de With, G. Measuring mechanical properties of coatings: a methodology applied to nano-particle-filled sol-gel coatings on glass. *Materials Science & Engineering R-Reports* **2002**, *36*, 47-103.
- (12) Longmire, M.; Choyke, P. L.; Kobayashi, H. Clearance properties of nano-sized particles and molecules as imaging agents: considerations and caveats. *Nanomedicine* **2008**, *3*, 703-717.
- (13) Huang, M. H.; Mao, S.; Feick, H.; Yan, H. Q.; Wu, Y. Y.; Kind, H.; Weber, E.; Russo, R.; Yang,

- P. D. Room-temperature ultraviolet nanowire nanolasers. *Science* **2001**, 292, 1897-1899.
- (14) Duan, X. F.; Niu, C. M.; Sahi, V.; Chen, J.; Parce, J. W.; Empedocles, S.; Goldman, J. L. High-performance thin-film transistors using semiconductor nanowires and nanoribbons. *Nature* **2003**, 425, 274-278.
- (15) Huynh, W. U.; Dittmer, J. J.; Alivisatos, A. P. Hybrid nanorod-polymer solar cells. *Science* **2002**, 295, 2425-2427.
- (16) Ko, H.; Tsukruk, V. V. Liquid-crystalline processing of highly oriented carbon nanotube arrays for thin-film transistors. *Nano Letters* **2006**, 6, 1443-1448.
- (17) Duan, X. F. Assembled semiconductor nanowire thin films for high-performance flexible macroelectronics. *MRS Bulletin* **2007**, 32, 134-141.
- (18) Lee, S. W.; Lee, S. K.; Belcher, A. M. Virus-based alignment of inorganic, organic, and biological nanosized materials. *Advanced Materials* **2003**, 15, 689-692.
- (19) Davidson, P.; Batail, P.; Gabriel, J. C. P.; Livage, J.; Sanchez, C.; Bourgaux, C. Mineral liquid crystalline polymers. *Progress in Polymer Science* **1997**, 22, 913-936.
- (20) vanBruggen, M. P. B.; vanderKooij, F. M.; Lekkerkerker, H. N. W. Liquid crystal phase transitions in dispersions of rod-like colloidal particles. *Journal of Physics-Condensed Matter* **1996**, 8, 9451-9456.
- (21) Vroege, G. J.; Thies-Weesie, D. M. E.; Petukhov, A. V.; Lemaire, B. J.; Davidson, P. Smectic Liquid-Crystalline Order in Suspensions of Highly Polydisperse Goethite Nanorods. *Advanced Materials*. **2006**, 18, 2565-2568.
- (22) Dessombz, A.; Chiche, D.; Davidson, P.; Panine, P.; Chaneac, C.; Jolivet, J. P. Design of liquid-crystalline aqueous suspensions of rutile nanorods: Evidence of anisotropic photocatalytic properties. *Journal of the American Chemical Society* **2007**, 129, 5904-5909.
- (23) Li, L. S.; Marjanska, M.; Park, G. H. J.; Pines, A.; Alivisatos, A. P. Isotropic-liquid crystalline phase diagram of a CdSe nanorod solution. *The Journal of Chemical Physics*. **2004**, 120, 1149-1152.
- (24) Zhang, S. J.; Pelligra, C. I.; Keskar, G.; Majewski, P. W.; Ren, F.; Pfefferle, L. D.; Osuji, C. O. Liquid Crystalline Order and Magnetocrystalline Anisotropy in Magnetically Doped Semiconducting ZnO Nanowires. *ACS Nano* **2011**, 5, 8357-8364.
- (25) Zhang, S. J.; Majewski, P. W.; Keskar, G.; Pfefferle, L. D.; Osuji, C. O. Lyotropic Self-Assembly of High-Aspect-Ratio Semiconductor Nanowires of Single-Crystal ZnO. *Langmuir* **2011**, 27, 11616-11621.
- (26) Sharma, V.; Park, K.; Srinivasarao, M. Colloidal dispersion of gold nanorods: Historical background, optical properties, seed-mediated synthesis, shape separation and self-assembly. *Materials Science & Engineering R-Reports* **2009**, 65, 1-38.

- (27) Murphy, C. J.; San, T. K.; Gole, A. M.; Orendorff, C. J.; Gao, J. X.; Gou, L.; Hunyadi, S. E.; Li, T. Anisotropic metal nanoparticles: Synthesis, assembly, and optical applications. *Journal of Physical Chemistry B* **2005**, *109*, 13857-13870.
- (28) Murphy, C. J.; Jana, N. R. Controlling the aspect ratio of inorganic nanorods and nanowires. *Advanced Materials* **2002**, *14*, 80-82.
- (29) Meuer, S.; Oberle, P.; Theato, P.; Tremel, W.; Zentel, R. Liquid crystalline phases from polymer-functionalized TiO₂ nanorods. *Advanced Materials* **2007**, *19*, 2073-2078.
- (30) Davis, V. A.; Ericson, L. M.; Parra-Vasquez, A. N.; Fan, H.; Wang, Y.; Prieto, V.; Longoria, J. A.; Ramesh, S.; Saini, R.; Kittrell, C.; Billups, W. E.; Adams, W. W.; Hauge, R. H.; Smalley, R. E.; Pasquali, M. Phase Behavior and Rheology of SWNTs in Superacids. *Macromolecules* **2004**, *37*, 154-160.
- (31) Davis, V. A.; Parra-Vasquez, A. N. G.; Green, M. J.; Rai, P. K.; Behabtu, N.; Prieto, V.; Booker, R. D.; Schmidt, J.; Kesselman, E.; Zhou, W.; Fan, H.; Adams, W. W.; Hauge, R. H.; Fischer, J. E.; Cohen, Y.; Talmon, Y.; Smalley, R. E.; Pasquali, M. True solutions of single-walled carbon nanotubes for assembly into macroscopic materials. *Nature Nanotechnology* **2009**, *4*, 830-834.
- (32) Green, M. J. Isotropic-nematic phase separation and demixing in mixtures of spherical nanoparticles with length-polydisperse nanorods. *Journal of Polymer Science Part B-Polymer Physics* **2012**, *50*, 1321-1327.
- (33) Ao, G. Liquid Crystalline Phase Behavior and Fiber Spinning of Double-Stranded DNA Stabilized Single-Walled Carbon Nanotube Dispersions. PhD., Auburn University, May, 2012 2012.
- (34) Ao, G.; Nepal, D.; Aono, M.; Davis, V. A. Cholesteric and Nematic Liquid Crystalline Phase Behavior of Double-Stranded DNA Stabilized Single-Walled Carbon Nanotube Dispersions. *ACS Nano* **2011**, *5*, 1450-1458.
- (35) Murali, S.; Xu, T.; Marshall, B. D.; Kayatin, M. J.; Pizarro, K.; Radhakrishnan, V. K.; Nepal, D.; Davis, V. A. Lyotropic Liquid Crystalline Self-Assembly in Dispersions of Silver Nanowires and Nanoparticles. *Langmuir*, 2010; Vol. 26, pp 11176-11183.
- (36) Wu, Y.; Xiang, J.; Yang, C.; Lu, W.; Lieber, C. M. Single-crystal metallic nanowires and metal/semiconductor nanowire heterostructures. *Nature* **2004**, *430*, 61-65.
- (37) Oldenburg, A. L.; Hansen, M. N.; Zweifel, D. A.; Wei, A.; Boppart, S. A. Plasmon-resonant gold nanorods as low backscattering albedo contrast agents for optical coherence tomography. *Optics Express* **2006**, *14*, 6724-6738.
- (38) Wang, H. F.; Huff, T. B.; Zweifel, D. A.; He, W.; Low, P. S.; Wei, A.; Cheng, J. X. In vitro and in vivo two-photon luminescence imaging of single gold nanorods. *Proceedings of the National Academy of Sciences of the United States of America* **2005**, *102*, 15752-15756.
- (39) Aslan, K.; Leonenko, Z.; Lakowicz, J. R.; Geddes, C. D. Annealed silver-island films for

applications in metal-enhanced fluorescence: Interpretation in terms of radiating plasmons. *Journal of Fluorescence* **2005**, *15*, 643-654.

(40) Haynes, C. L.; McFarland, A. D.; Van Duyne, R. P. Surface-enhanced Raman spectroscopy. *Analytical Chemistry* **2005**, *77*, 338A-346A.

(41) Chen, J. Y.; Wiley, B. J.; Xia, Y. N. One-dimensional nanostructures of metals: Large-scale synthesis and some potential applications. *Langmuir* **2007**, *23*, 4120-4129.

(42) Pang, Y. T.; Meng, G. W.; Fang, Q.; Zhang, L. D. Silver nanowire array infrared polarizers. *Nanotechnology* **2003**, *14*, 20-24.

(43) Hu, X. H.; Chan, C. T. Photonic crystals with silver nanowires as a near-infrared superlens. *Applied Physics Letters* **2004**, *85*, 1520-1522.

(44) Munoz, J. E.; Cervantes, J.; Esparza, R.; Rosas, G. Iron nanoparticles produced by high-energy ball milling. *Journal of Nanoparticle Research* **2007**, *9*, 945-950.

(45) Okada, T.; Kawashima, K.; Nakata, Y. Nano-wire pig-tailed ZnO nano-rods synthesized by laser ablation. *Thin Solid Films* **2006**, *506*, 274-277.

(46) Vasquez, Y.; Henkes, A. E.; Bauer, J. C.; Schaak, R. E. Nanocrystal conversion chemistry: A unified and materials-general strategy for the template-based synthesis of nanocrystalline solids. *Journal of Solid State Chemistry* **2008**, *181*, 1509-1523.

(47) Rao, C. N. R.; Deepak, F. L.; Gundiah, G.; Govindaraj, A. Inorganic nanowires. *Progress in Solid State Chemistry* **2003**, *31*, 5-147.

(48) Cao, G. Z.; Liu, D. W. Template-based synthesis of nanorod, nanowire, and nanotube arrays. *Advances in Colloid and Interface Science* **2008**, *136*, 45-64.

(49) Tsuji, M.; Hashimoto, M.; Nishizawa, Y.; Tsuji, T. Synthesis of gold nanorods and nanowires by a microwave-polyol method. *Materials Letters* **2004**, *58*, 2326-2330.

(50) Liu, X.; Tian, B.; Yu, C.; Tu, B.; Zhao, D. Nanoporous arrays of metal sulfides templated by mesoporous silica. *Studies in Surface Science and Catalysis* **2004**, *154*, 939-945.

(51) Han, Y. J.; Kim, J. M.; Stucky, G. D. Preparation of noble metal nanowires using hexagonal mesoporous silica SBA-15. *Chemistry of Materials* **2000**, *12*, 2068-2069.

(52) El-Sayed, M. A. Some interesting properties of metals confined in time and nanometer space of different shapes. *Accounts of Chemical Research* **2001**, *34*, 257-264.

(53) Sun, Y. G.; Xia, Y. N. Shape-controlled synthesis of gold and silver nanoparticles. *Science* **2002**, *298*, 2176-2179.

(54) Lin, S. W.; Yue, J.; Gedanken, A. Synthesis of long silver nanowires from AgBr nanocrystals. *Advanced Materials* **2001**, *13*, 656-658.

(55) Kuijk, A.; van Blaaderen, A.; Imhof, A. Synthesis of Monodisperse, Rodlike Silica Colloids

with Tunable Aspect Ratio. *Journal of the American Chemical Society* **2011**, *133*, 2346-2349.

(56) Jehnichen, D.; Tobisch, J.; Friedel, P.; Pospiech, D. Structure investigations of regular main chain copolyesters. *Polymer* **1996**, *37*, 1463-1475.

(57) Donald, A.; Windle, A.; Hanna, S. *Liquid Crystalline Polymers*; 2nd ed.; Cambridge: Cambridge, 2006.

(58) Friedel, G. The Mesomorphic States of Matter. *Annales de Physique* **1922**, *18*, 273-274.

(59) Bouligan, Y. Fibillar orientations in skeleton of arthropoda 1 crabs, twist-joint arrangement of laminae. *Journal of Microscopy-Oxford* **1971**, *11*, 441.

(60) Lavrentovich, O. D. Hyperbolic monopole in a smectic C liquid-crystal. *JETP Letters* **1986**, *43*, 382-385.

(61) Fournier, J. B.; Dozov, I.; Durand, G. Surface frustration and texture instability in smectic-A liquid crystals. *Physical Review A* **1990**, *41*, 2252-2255.

(62) Boltenhagen, P.; Lavrentovich, O. D.; Kleman, M. Focal conic domains with positive Gaussian curvature and saddle-splay rigidity of smectic L-alpha phases. *Physical Review A* **1992**, *46*, R1743-R1746.

(63) Onsager, L. The effect of shape on the interaction of colloidal particles. *Annals of the New York Academy of Sciences* **1949**, *51*, 627-659.

(64) Flory, P. J. Theory of crystallization in copolymers. *Transactions of the Faraday Society* **1955**, *51*, 848-857.

(65) Lekkerkerker, H. N. W.; Coulon, P.; Vanderhaegen, R.; Deblieck, R. On the isotropic-liquid crystal phase-separation in a solution of rodlike particles of different lengths. *Journal of Chemical Physics* **1984**, *80*, 3427-3433.

(66) Speranza, A.; Sollich, P. Simplified Onsager theory for isotropic-nematic phase equilibria of length polydisperse hard rods. *Journal of Chemical Physics* **2002**, *117*, 5421-5436.

(67) Vroege, G. J.; Lekkerkerker, H. N. W. Phase-transition in lyotropic colloidal and polymer liquid-crystals. *Reports on Progress in Physics* **1992**, *55*, 1241-1309.

(68) Khokhlov, A. R.; Semenov, A. N. On the theory of liquid-crystalline ordering of polymer-chain with limited flexibility. *Journal of Statistical Physics* **1985**, *38*, 161-182.

(69) Green, M. J.; Parra-Vasquez, A. N. G.; Behabtu, N.; Pasquali, M. Modeling the phase behavior of polydisperse rigid rods with attractive interactions with applications to single-walled carbon nanotubes in superacids. *The Journal of Chemical Physics* **2009**, *131*, 10.

(70) Rai, P. K.; Pinnick, R. A.; Parra-Vasquez, A. N. G.; Davis, V. A.; Schmidt, H. K.; Hauge, R. H.; Smalley, R. E.; Pasquali, M. Isotropic-nematic phase transition of single-walled carbon nanotubes in strong acids. *Journal of the American Chemical Society* **2006**, *128*, 591-595.

- (71) Larson, R. *The Structure and Rheology of Complex Fluids*; Oxford University Press: New York, 1999.
- (72) Larson, R. G.; Mead, D. W. The Ericksen number and Deborah number cascades in sheared polymer nematics. *Liquid Crystals* **1993**, *15*, 151-169.
- (73) Wissbrun, K. F. Rheology of rod-like polymers in the liquid-crystalline state. *Journal of Rheology* **1981**, *25*, 619-662.
- (74) Kiss, G.; Porter, R. S. Flow Induced phenomena of lyotropic polymer liquid crystals: the negative normal force effect and bands perpendicular to shear. In *Mechanical and Thermophysical Properties of Polymer Liquid Crystals*; W. Brostow. London, Chapman & Hall, 1998, pp 342-406.
- (75) Asada, T.; Muramatsu, H.; Watanabe, R.; Onogi, S. Rheooptical studies of racemic poly(γ -benzyl glutamate) liquid-crystals. *Macromolecules* **1980**, *13*, 867-871.
- (76) Larson, R. G. Roll-cell instabilities in shearing flows of nematic polymers. *Journal of Rheology* **1993**, *37*, 175-197.
- (77) Walker, L. M.; Wagner, N. J.; Larson, R. G.; Mirau, P. A.; Moldenaers, P. The rheology of highly concentrated PBLG solutions. *Journal of Rheology* **1995**, *39*, 925-952.
- (78) Walker, L. M.; Kernick, W. A.; Wagner, N. J. In situ analysis of the defect texture in liquid crystal polymer solutions under shear. *Macromolecules* **1997**, *30*, 508-514.
- (79) Moldenaers, P.; Mewis, J. Transient-behavior of liquid-crystalline solution of poly(benzylglutamate). *Journal of Rheology* **1986**, *30*, 567-584.
- (80) Vermant, J.; Moldenaers, P.; Picken, S. J.; Mewis, J. A comparison between texture and rheological behavior of lyotropic liquid-crystalline polymers during flow. *Journal of Non-Newtonian Fluid Mechanics* **1994**, *53*, 1-23.
- (81) Picken, S. J.; Aerts, J.; Doppert, H. L.; Reuvers, A. J.; Northolt, M. G. Structure and rheology of aramid solutions-transient rheological and rheooptical measurements. *Macromolecules* **1991**, *24*, 1366-1375.
- (82) Moldenaers, P.; Mewis, J. Relaxational phenomena and anisotropy in lyotropic polymeric liquid-crystals. *Journal of Non-Newtonian Fluid Mechanics* **1990**, *34*, 359-374.
- (83) Mortier, M.; Moldenaers, P.; Mewis, J. Transient rheological behaviour of poly-para-phenyleneterephthalamide (PpPTA) in sulphuric acid. *Rheologica Acta* **1996**, *35*, 57-68.
- (84) Larson, R. G.; Mead, D. W. Time and shear-rate scaling laws for liquid-crystal polymers. *Journal of Rheology* **1989**, *33*, 1254-1281.
- (85) Kiss, G.; Porter, R. S. Rheology of concentrated-solutions of poly(Gamma-Benzyl-Glutamate). *Journal of Polymer Science Part C-Polymer Symposium* **1978**, 193-211.

- (86) Kiss, G.; Porter, R. S. Rheology of concentrated-solutions of helical polypeptides. *Journal of Polymer Science Part B-Polymer Physics* **1980**, *18*, 361-388.
- (87) Marrucci, G.; Maffettone, P. L. Description of the liquid-crystalline phase of rodlike polymers at high shear rates. *Macromolecules* **1989**, *22*, 4076-4082.
- (88) Larson, R. G. Arrested tumbling in shearing flows of liquid-crystal polymers. *Macromolecules* **1990**, *23*, 3983-3992.
- (89) Kiss, G.; Porter, R. S. Rheo-optical studies of liquid-crystalline solutions of helical polypeptides. *Molecular Crystals and Liquid Crystals* **1980**, *60*, 267-&.
- (90) Grizzuti, N.; Cavella, S.; Cicarelli, P. Transient and steady-state rheology of a liquid-crystalline hydroxypropylcellulose solution. *Journal of Rheology* **1990**, *34*, 1293-1310.
- (91) Larson, R. G.; Winey, K. I.; Patel, S. S.; Watanabe, H.; Bruinsma, R. The rheology of layered liquids - lamellar block-copolymers and smectic liquid-crystals. *Rheologica Acta* **1993**, *32*, 245-253.
- (92) Oswald, P.; Pieranski, P. *Smectic and Columnar Liquid Crystals*; Taylor & Francis, Boca Raton 2006.
- (93) Colby, R. H.; Ober, C. K.; Gillmor, J. R.; Connelly, R. W.; Duong, T.; Galli, G.; Laus, M. Smectic rheology. *Rheologica Acta* **1997**, *36*, 498-504.
- (94) Helfrich, W. Capillary flow of cholesteric and smectic liquid crystals. *Physical Review Letters* **1969**, *23*, 372-374.
- (95) Horn, R. G.; Kleman, M. Observations on shear-induced textures and rheology of a smectic-A phase. *Annales De Physique* **1978**, *3*, 229-234.
- (96) Colby, R. H.; Nentwich, L. M.; Clingman, S. R.; Ober, C. K. Defect-mediated creep of structured materials. *Europhysics Letters* **2001**, *54*, 269-274.
- (97) Bouligan, Y. Study of mesomorphic textures confocal domains in smectics-review and theoretical considerations. *Journal De Physique* **1972**, *33*, 525-&.
- (98) Meyer, C.; Asnacios, S.; Bourgaux, C.; Kleman, M. Rheology of lyotropic and thermotropic lamellar phases. *Rheologica Acta* **2000**, *39*, 223-233.
- (99) Meyer, C.; Asnacios, S.; Kleman, M. Universal properties of lamellar systems under weak shear. *European Physical Journal E* **2001**, *6*, 245-253.
- (100) Gou, L. F.; Chipara, M.; Zaleski, J. M. Convenient, rapid synthesis of Ag nanowires. *Chemistry of Materials* **2007**, *19*, 4378-4378.
- (101) Song, W. H.; Kinloch, I. A.; Windle, A. H. Nematic liquid crystallinity of multiwall carbon nanotubes. *Science* **2003**, *302*, 1363-1363.
- (102) Adams, M.; Dogic, Z.; Keller, S. L.; Fraden, S. Entropically driven microphase transitions in

mixtures of colloidal rods and spheres. *Nature* **1998**, 393, 349-352.

(103) Zhou, W.; Fischer, J. E.; Heiney, P. A.; Fan, H.; Davis, V. A.; Pasquali, M.; Smalley, R. E. Single-walled carbon nanotubes in superacid: X-ray and calorimetric evidence for partly ordered H₂SO₄. *Physical Review B* **2005**, 72, 5.

(104) Marrucci, G. Rheology of liquid-crystalline polymers. *Physica Scripta* **1991**, T35, 44-46.

(105) Marrucci, G. Tumbling regime of liquid-crystalline polymers. *Macromolecules* **1991**, 24, 4176-4182.

(106) Kulicke, W. M.; Jeberien, H. E.; Kiss, H.; Porter, R. S. Visual observation of flow irregularities in polymer-solutions at theta-conditions. *Rheologica Acta* **1979**, 18, 711-716.

(107) Alderman, N. J.; Mackley, M. R. Optical textures observed during the shearing of thermotropic liquid-crystal polymers. *Faraday Discussions* **1985**, 79, 149-160.

(108) Graziano, D. J.; Mackley, M. R. Disclinations observed during the shear of MBBA. *Molecular Crystals and Liquid Crystals* **1984**, 106, 103-119.

(109) Graziano, D. J.; Mackley, M. R. Shear induced optical textures and their relaxation behavior in thermotropic liquid-crystalline polymers. *Molecular Crystals and Liquid Crystals* **1984**, 106, 73-93.

(110) Deneve, T.; Navard, P.; Kleman, M. Shear rheology and shear-induced textures of a thermotropic copolyesteramide. *Journal of Rheology* **1993**, 37, 515-529.

(111) Mather, P. T.; Pearson, D. S.; Larson, R. G. Flow patterns and disclination-density measurements in sheared nematic liquid crystals .2. Tumbling 8CB. *Liquid Crystals* **1996**, 20, 539-546.

(112) Dobb, M. G.; Johnson, D. J.; Saville, B. P. Supramolecular structure of a high-modulus polyaromatic fiber (Kevlar 49). *Journal of Polymer Science Part B-Polymer Physics* **1977**, 15, 2201-2211.

(113) Donald, A. M.; Viney, C.; Windle, A. H. Banded structures in oriented thermotropic polymers. *Polymer* **1983**, 24, 155-159.

(114) Simmens, S. C.; Hearle, J. W. S. Observation of bands in high-modulus aramid fibers by optical microscopy. *Journal of Polymer Science Part B-Polymer Physics* **1980**, 18, 871-876.

(115) Thapar, H.; Bevis, M. The micromorphology of an injection molded thermotropic liquid-crystal polymer. *Journal of Materials Science Letters* **1983**, 2, 733-736.

(116) Ernst, B.; Navard, P. Band textures in mesomorphic (hydroxypropyl) cellulose solutions. *Macromolecules* **1989**, 22, 1419-1422.

(117) Navard, P. Formation of band textures in hydroxypropylcellulose liquid-crystals. *Journal of Polymer Science Part B-Polymer Physics* **1986**, 24, 435-442.

- (118) Wang, J.; Labes, M. M. Control of the anisotropic mechanical-properties of liquid-crystal polymer-films by variations in their banded texture. *Macromolecules* **1992**, *25*, 5790-5793.
- (119) Viney, C.; Putnam, W. S. The banded microstructure of sheared liquid-crystalline polymers. *Polymer* **1995**, *36*, 1731-1741.
- (120) Marrucci, G.; Grizzuti, N.; Buonauro, A. Band formation in sheared HPC solutions-effects of sample thickness. *Molecular Crystals and Liquid Crystals* **1987**, *153*, 263-269.
- (121) Marsano, E.; Carpaneto, L.; Ciferri, A. Formation of a banded texture in solutions of liquid-crystalline polymers: hydroxypropylcellulose in H₂O. *Molecular Crystals and Liquid Crystals* **1988**, *158*, 267-278.
- (122) Li, Q. W.; Zhu, Y. T.; Kinloch, I. A.; Windle, A. H. Self-organization of carbon nanotubes in evaporating droplets. *J. Phys. Chem. B* **2006**, *110*, 13926-13930.
- (123) Zhang, S. J.; Li, Q. W.; Kinloch, I. A.; Windle, A. H. Ordering in a Droplet of an Aqueous Suspension of Single-Wall Carbon Nanotubes on a Solid Substrate. *Langmuir* **2010**, *26*, 2107-2112.
- (124) Jana, N. R.; Gearheart, L. A.; Obare, S. O.; Johnson, C. J.; Edler, K. J.; Mann, S.; Murphy, C. J. Liquid crystalline assemblies of ordered gold nanorods. *Journal of Materials Chemistry* **2002**, *12*, 2909-2912.
- (125) Yunker, P. J.; Still, T.; Lohr, M. A.; Yodh, A. G. Suppression of the coffee-ring effect by shape-dependent capillary interactions. *Nature* **2011**, *476*, 308-311.
- (126) Borodko, Y.; Habas, S. E.; Koebel, M.; Yang, P.; Frei, H.; Somorjai, G. A. Probing the interaction of poly(vinylpyrrolidone) with platinum nanocrystals by UV-Raman and FTIR. *Journal of Physical Chemistry B* **2006**, *110*, 23052-23059.
- (127) Miller, M. S.; O'Kane, J. C.; Niec, A.; Carmichael, R. S.; Carmichael, T. B. Silver Nanowire/Optical Adhesive Coatings as Transparent Electrodes for Flexible Electronics. *Acs Applied Materials & Interfaces* **2013**, *5*, 10165-10172.
- (128) Kuijk, A.; Byelov, D. V.; Petukhov, A. V.; van Blaaderen, A.; Imhof, A. Phase behavior of colloidal silica rods. *Faraday Discussions* **2012**, *159*, 181-199.
- (129) Bolhuis, P.; Frenkel, D. Tracing the phase boundaries of hard spherocylinders. *Journal of Chemical Physics* **1997**, *106*, 666-687.
- (130) Kitamura, R.; Pilon, L.; Jonasz, M. Optical constants of silica glass from extreme ultraviolet to far infrared at near room temperature. *Applied Optics* **2007**, *46*, 8118-8133.
- (131) Amirthalingam, T.; Kalirajan, J.; Chockalingam, A. Use of silica-gold core shell structured nanoparticles for targeted drug delivery system. *Journal of Nanomedicine Nanotechnology* **2011**, *2*.
- (132) Taylor, L. S.; Langkilde, F. W.; Zograf, G. Fourier transform Raman spectroscopic study of

the interaction of water vapor with amorphous polymers. *Journal of Pharmaceutical Sciences* **2001**, *90*, 888-901.

(133) Duverger, C.; Nedelec, J. M.; Benatsou, M.; Bouazaoui, M.; Capoen, B.; Ferrari, M.; Turrell, S. Waveguide Raman spectroscopy: a non-destructive tool for the characterization of amorphous thin films. *Journal of Molecular Structure* **1999**, *481*, 169-178.

(134) Chen, D.; Shen, Y. Q.; Zhu, C. H.; Hough, L. E.; Gimeno, N.; Glaser, M. A.; MacLennan, J. E.; Ros, M. B.; Clark, N. A. Interface structure of the dark conglomerate liquid crystal phase. *Soft Matter* **2011**, *7*, 1879-1883.

(135) Gopinath, D.; Ravi, D.; Rao, B. R.; Apte, S. S.; Renuka, D.; Rambhau, D. Ascorbyl palmitate vesicles (Aspasomes): formation, characterization and applications. *International Journal of Pharmaceutics* **2004**, *271*, 95-113.

(136) Kato, T.; Mizoshita, N.; Kishimoto, K. Functional liquid-crystalline assemblies: Self-organized soft materials. *Angewandte Chemie-International Edition* **2006**, *45*, 38-68.

(137) Percec, V.; Cho, W. D.; Ungar, G. Increasing the diameter of cylindrical and spherical supramolecular dendrimers by decreasing the solid angle of their monodendrons via periphery functionalization. *Journal of the American Chemical Society* **2000**, *122*, 10273-10281.

(138) Donnio, B.; Guillon, D. Liquid crystalline dendrimers and polypedes. In *Supramolecular Polymers Polymeric Betains Oligomers*; Springer-Verlag Berlin: Berlin, 2006; Vol. 201, pp 45-155.

(139) Meyer, C.; Nastishin, Y.; Kleman, M. Kinked focal conic domains in a SmA. *Molecular Crystals and Liquid Crystals* **2007**, *477*, 537-547.

(140) Nastishin, Y. A.; Meyer, C.; Kleman, M. Imperfect focal conic domains in A smectics: a textural analysis. *Liquid Crystals* **2008**, *35*, 609-624.

(141) Papkov, S. P.; Kulichik, V. G.; Kalmykov, V. D.; Malkin, A. Y. Rheological properties of anisotropic poly(para-benzamide) solutions. *Journal of Polymer Science Part B-Polymer Physics* **1974**, *12*, 1753-1770.

(142) Speranza, A.; Sollich, P. Isotropic-nematic phase equilibria in the Onsager theory of hard rods with length polydispersity. *Physical Review E* **2003**, *67*, 19.

(143) Wensink, H. H.; Vroege, G. J. Isotropic-nematic phase behavior of length-polydisperse hard rods. *The Journal of Chemical Physics* **2003**, *119*, 6868-6882.

(144) Davis, V. A.; Ericson, L. M.; Parra-Vasquez, A. N. G.; Fan, H.; Wang, Y. H.; Prieto, V.; Longoria, J. A.; Ramesh, S.; Saini, R. K.; Kittrell, C.; Billups, W. E.; Adams, W. W.; Hauge, R. H.; Smalley, R. E.; Pasquali, M. Phase Behavior and rheology of SWNTs in superacids. *Macromolecules* **2004**, *37*, 154-160.

(145) Green, M. J.; Parra-Vasquez, A. N. G.; Behabtu, N.; Pasquali, M. Modeling the phase

behavior of polydisperse rigid rods with attractive interactions with applications to single-walled carbon nanotubes in superacids. *Journal of Chemical Physics* **2009**, *131*, 10.

(146) Cohen, Y.; Buchner, S.; Zachmann, H. G.; Davidov, D. Phase-transitions in solutions of rigid polymers studied by synchrotron radiation. *Polymer* **1992**, *33*, 3811-3817.

(147) Davis, V. A. Liquid crystalline assembly of nanocylinders. *Journal of Materials Research* **2011**, *26*, 140-153.

(148) Boltenhagen, P.; Lavrentovich, O.; Kleman, M. Oil streaks and focal conic domains in L-Alpha lyotropic liquid-crystals. *Journal De Physique I* **1991**, *1*, 1233-1252.

(149) Kleman, M.; Lavrentovich, O. D. Liquids with conics. *Liquid Crystals* **2009**, *36*, 1085-1099.

(150) Chaveriat, L.; Meyer, C.; Beaupere, D.; Demailly, G.; Stasik, I. 6-S-alkyl-6-thiohexonolactones and 6-S-alkyl-6-thiohexitols: Efficient synthesis and new smectic liquid crystal phases. *Journal of Molecular Liquids* **2008**, *142*, 17-21.

(151) Chatterjee, S.; Anna, S. L. Interaction of toroidal focal conic defects with shear flow. *Soft Matter* **2012**, *8*, 6698-6705.

(152) Kiss, G.; Porter, R. S. Rheology of concentrated solutions of poly(gamma-benzyl-glutamate). *Journal of Polymer Science Part B-Polymer Physics* **1996**, *34*, 2271-2289.

(153) Ciferri, A. *Rheology of Nematic Polymers*. VCH Publishers: New York, 1991; p 438.

(154) Ureña-Benavides, E. E.; Ao, G.; Davis, V. A.; Kitchens, C. L. Rheology and Phase Behavior of Lyotropic Cellulose Nanocrystal Suspensions. *Macromolecules* **2011**, *44*, 8990-8998.

(155) Solomon, M. J.; Spicer, P. T. Microstructural regimes of colloidal rod suspensions, gels, and glasses. *Soft Matter*, *6*, 1391-1400.

(156) Kiss, G. D. Rheology and Rheo-Optics of Concentrated Solutions of Helical Polypeptides. Ph.D., University of Massachusetts 1979.

(157) Fujii, S.; Ishii, Y.; Komura, S.; Lu, C. Y. D. Smectic rheology close to the smectic-nematic transition. *Europhysics letters* **2010**, *90*.

(158) Moller, P. C. F.; Mewis, J.; Bonn, D. Yield stress and thixotropy: on the difficulty of measuring yield stresses in practice. *Soft Matter* **2006**, *2*, 274-283.

(159) Oswald, P.; Allain, M. Rheology and structural defects in a lyotropic lamellar phase. *Journal of Colloid and Interface Science* **1988**, *126*, 45-53.

(160) Fujii, S.; Komura, S.; Ishii, Y.; Lu, C. Y. D. Elasticity of smectic liquid crystals with focal conic domains. *Journal of Physics-Condensed Matter* **2011**, *23*.

(161) Diat, O.; Roux, D.; Nallet, F. Effect of shear on a lyotropic lamellar phase. *Journal De Physique II* **1993**, *3*, 1427-1452.

(162) Diat, O.; Roux, D. Preparation of monodisperse multilayer vesicles of controlled size and

high encapsulation ratio. *Journal De Physique I* **1993**, 3, 9-14.

(163) Diat, O.; Roux, D. Effect of shear on dilute sponge phase. *Langmuir* **1995**, 11, 1392-1395.

(164) Deegan, R. D.; Bakajin, O.; Dupont, T. F.; Huber, G.; Nagel, S. R.; Witten, T. A. Capillary flow as the cause of ring stains from dried liquid drops. *Nature* **1997**, 389, 827-829.

(165) Deegan, R. D.; Bakajin, O.; Dupont, T. F.; Huber, G.; Nagel, S. R.; Witten, T. A. Contact line deposits in an evaporating drop. *Physical Review E* **2000**, 62, 756-765.